DOKUZ EYLUL UNIVERSITY

GRADUATE SCHOOL OF NATURAL AND APPLIED SCIENCES

SYNTHESIS OF GARNET BASED FILMS BY SOL-GEL TECHNIQUE AND INVESTIGATION OF THEIR MAGNETO-OPTIC PROPERTIES

by

Mustafa EROL

July, 2009

İZMİR

SYNTHESIS OF GARNET BASED FILMS BY SOL-GEL TECHNIQUE AND INVESTIGATION OF THEIR MAGNETO-OPTIC PROPERTIES

A Thesis Submitted to the
Graduate School of Natural and Applied Sciences of Dokuz Eylul University
In Partial Fulfillment of the Requirements for the Degree of Master of Science
in Metallurgical and Materials Engineering, Metallurgical and Materials Program

by
Mustafa EROL

July, 2009
İZMİR

M. Sc. THESIS EXAMINATION RESULT FORM

We have read the thesis entitled **"SYNTHESIS OF GARNET BASED FILMS BY SOL-GEL TECHNIQUE AND INVESTIGATION OF THEIR MAGNETO-OPTIC PROPERTIES"** completed by **MUSTAFA EROL** under revision of **ASSOC. PROF. DR. ERDAL ÇELİK** and we certitfy that in our opinion it is fully adequate, in scope and in quality, as a thesis for the degree of Master of Science.

.....

Assoc. Prof. Dr. Erdal ÇELİK

Supervisor

.....

(Jury Member)

.....

(Jury Member)

.....

Prof.Dr. Cahit HELVACI

Director

Graduate School of Natural and Applied Science

ACKNOWLEDGEMENTS

I sincerely thank for the people who mentally support and encourage me, aid me in my pursuing of the M. Sc. degree, and help in my academic accomplishment.

Firstly, I would like to thank Assoc. Prof. Dr. Erdal ÇELİK for his supervision, guidance, patience, and support in this work.

I also would like to thank my all colleagues especially Yavuz Öztürk, M. Faruk Ebeoğlugil and Orkut Sancakoğlu for their cooperation, friendship and patience

Finally, I would like to thank my all family for their support and persistence.

The present research was also supported by (TUBITAK) with project code 106T651 named as; Production of garnet based nano films and investigation of their magneto-optical properties.

Mustafa EROL

SYNTHESIS OF GARNET BASED FILMS BY SOL-GEL TECHNIQUE AND INVESTIGATION OF THEIR MAGNETO-OPTIC PROPERTIES

ABSTRACT

The objective of this study is to fabricate YIG thin films produced via sol-gel technique on several substrates and characterize them structurally, magnetically and magneto-optically. In order to evaluate solution characteristics which affect thin film structure; turbidity, pH values, and rheological properties of the prepared solutions were measured by turbidimeter, pH meter and rheometer machines before coating process. In order to use suitable process regime and to define chemical structure and reaction type of intermediate temperature products, Differential Thermal Analysis-Thermogravimetry (DTA-TG) and Fourier Transform Infrarared (FTIR) devices were used in the film production. Phase identification of the films was performed using X-Ray Diffraction (XRD) and surface morphology was investigated using Scanning Electron Microscopy with an Energy Dispersive X-ray spectroscopy (IXRF System EDS) system attachment. Thickness measurements of the films were investigated through refractometer and spectrophotometer devices. Magnetic and magneto-optical properties were characterized using vibrating sample magnetometer (VSM) and self design Magneto-optical experiment setup respectively. It was concluded that high purity YIG based thin films were successfully deposited on several substrates for magneto-optical applications.

Keywords: YIG, garnet, sol-gel, magnetism, magneto-optical properties

SOL-GEL TEKNİĞİ KULLANILARAK GARNET ESASLI FİLMLERİN ÜRETİLMESİ VE MANYETO-OPTİK OZELLİKLERİNİN İNCELENMESİ

ÖZ

Bu çalışmanın amacı, sol-jel tekniği kullanılarak YIG ince filmlerin çeşitli altlıklar üzerine üretilmesi ve yapısal, manyetik olarak ve manyeto-optik olarak karakterize edilmesidir. İnce film yapısına etki eden çözeltilerinin karakterizasyonu değerlendirmek için kaplama öncesi hazırlanan çözeltilerin bulanıklık, pH değerleri ve reolojik özellikleri turbidimetre, pH metre, ve reometre cihazları kullanılarak ölçülmüştür. Uygun ısıl işlem rejimini belirlemek ve film üretiminde, ara sıcaklıklardaki ürünlerin kimyasal yapısı ve reaksiyon tiplerini belirlemek için DTA-TG ve FTIR cihazları kullanılmıştır. Üretilen filmlerin faz analizleri X-ışını difraktometresi (XRD) kullanılarak, yüzey morfolojisi incelemeleri ise Enerji Saçılım spektroskopu ilaveli Taramalı Elektron mikroskobu SEM/EDS cihazı kullanılarak yapılmıştır. Filmlerin kalınlıkları refraktometre ve spektrofotometre cihazları ile ölçülmüştür. Manyetik ve manyeto-optik özellikler sırasıyla titreşimli numune manyetometresi (VSM) ve kendi tasarımımız olan manyeto-optik deney düzeneği ile karakterize edilmiştir. YIG bazlı ince filmler çeşitli altlıklar üzerine manyeto-optik uygulamaları için başarı ile kaplandığı bulunmuştur.

Anahtar kelimeler*:* YIG, garnet, sol-jel, manyetizma, manyeto-optik özellikler

CONTENTS

Page

CHAPTER ONE
INTRODUCTION

The silicate mineral garnet, which occurs fairly commonly in nature, has been known as a source of abrasive grit and has served as a semiprecious stone. Now that the synthesis of crystalline silicates is generally difficult, it was only quit recently that garnets of this type have been made and even more recently that nonsilicate garnet-structure materials have been produced.

The crystal structure of garnet is rather complex even though the crystal symmetry is cubic. There are, moreover, eight formula units $A_3B_2C_3O_{12}$ in a unit cell for a total of 160 atoms, as shown by a valuable X-ray diffraction study of natural garnet by powder techniques.

There is extensive body of knowledge concerning garnets and their structure as well as of the nature and origin of ferrimagnetism, ferrimagnetic garnets, exemplified by yttrium-iron garnet (YIG) were discovered. Since that time, a tremendous body of research results has been published. Furthermore, at least two new technological areas have grown enormously with the aid of YIG-based devices:

(i) tunable filters, circulators, and gyrators for us in the microwave region and
(ii) magnetic-bubble-domain-type digital memories: As the bulk of the material used in these applications consists of thin films c discs which are produced by epitaxial growth, the material properties depend on the growth process which is tailored to the specific application (Buschow, 1997).

In general, YIG is treated as the prototype material with the effects of the substitution of other rare earths for yttrium considered first. There have been a number of works in which various aspects of the ferrimagnetic garnets have been reviewed and summarized in excellent fashion. YIG has a complex cubic structure, non-magnetic Y^{3+} ions occupy dodecahedra) sites and magnetic Fe^{3+} ions occupy

octahedral and tetrahedral sites as in lattice. To improve magneto-optic properties of pure YIG, yttrium may be substituted by one of the lanthanides e.g., lanthanum, cerium, neodymium, gadolinium and so on. Its unit cell includes different magnetic ions, iron and one of the rare earth groups. Its magnetic property arises from the antiparallel ordering between Fe^{3+} ions in the octahedral and tetrahedral sites as a result of exchange couplings between the ions but the Y^{3+} ions couple weekly leading to cant-parallel to the tetrahedral site ion (Sekijima et al., 1999). The net magnetic moment of YIG per unit cell is 40 Bohr magnetrons (Moulson et al., 2003). Its saturation magnetization is 136 kA/m at room temperature. With Ce addition, paramagnetic trivalent Ce^{3+} ions are replaced with non-magnetic Y^{3+} ions in c-sites (Wickersheim et al., 1967).

Magneto-optic effect arises after the change of the state of the polarization of light due to interaction with a magnetic material discovered by M. Faraday who found that a polarized light was rotated after passing through a glass under an external magnetic field along the direction of propagation of incoming light. For a magnetic field perpendicular to incoming light similar rotation was also observed now known as Voigt effect. Magneto-optical effects for the YIG type and its variants can be explained macroscopically via difference in the refraction indices for right and left circularly polarized light hence it is quite often called circular birefringence. There is also similar effect of the circular dichroism arises from the absorbance differences for left and right circularly polarized light. Yet both effect can be attributed usually to the Zeeman effect, i.e., two degenerate electronic state split into two circular components which worked well for Bi-YIG. Transitions involving with these states produces usual absorption and dispersion line shapes (Shinagawa, 1999). YIG has very large figure of merit (rotation angle over the absorption) near infrared, however in the visible band the absorption becomes very large compare to the increase in the Faraday rotation angle making the material hard to use in a desired application. Hence there are many efforts to increase the magneto-optic properties of YIG, e.g, for Bi-YIG material this increase was observed as a function of the Bi concentration. The most suitable ions expected to increase the magneto-optical properties are those of having a right radii, e.g., Bi, Pb, Ce, Pr, Nd, Ru, Rh, Ir and Co (Das et al., 2002).

Furthermore some of the studies have focused on to enhance the magneto-optical properties and the magnetic properties revealed that the most promising candidate to enhance magneto-optical activity strongly in iron garnets in the visible and near infrared regions are cerium and bismuth substituted materials.

For other applications, there are also several works on the behavior of yttrium iron garnet mainly on the valence-uncompensated doping or the substitution of iron in tetrahedral or octahedral sites, or the substitution of yttrium in dodecahedral sites by different other metallic cations whereas, some others focused on possible application of YIG and substituted YIG as (Higuchi et al., 2002) who obtained Ce-YIG thin films for magnetic sensor applications. Their materials displayed greater Faraday rotation in Ce substitution than that of in Bi substitution. The magnetic-field sensitivity of $Ce_{0.24}Y_{2.76}Fe_5O_{12}$ was about 0.0048 % m/A larger than that of $(BiGdLaY)_3(FeGa)_5O_{12}$. Gomi et al. (1988) has made a single crystal thin film Ce-YIG for optical memory devices, and Mino et al. (1998) have grown Ce-YIG films for optical waveguides . They both employed the usual R.F. diode sputtering or the pulse laser deposition to prepare the cerium substituted YIG films. Ce-YIG single crystals have already been widely studied because the addition of cerium oxide can significantly enhance the Faraday rotation and reduce the optical propagation loss produced fibrous single crystals Ce-YIG by floating zone (FZ) method changing atmosphere to nitrogen atmosphere as they increased the solubility limit of Ce. Another application of Ce-YIG based on Faraday rotation is fabrication of non-reciprocal planar light-wave circuits of the thin films on an amorphous substrate having good magneto-optical properties made by Uno & Noge (2001)

As mentioned, several techniques can be employed to make YIG based materials such as RF magnetron sputtering, sol-gel and pulse laser deposition technique. Of these, the sol-gel processing has a number of advantages. To illustrate this, it is possible to synthesize quite good polycrystalline ferrites with the sol-gel method. The sol–gel process offers considerable advantages such as better mixing of the starting materials and excellent chemical homogeneity in the final product. Moreover, the molecular level mixing aids the structure evolution lowering the

crystallization temperature and the sol-gel layer can be deposited desired thickness in one step because this thickness depends only on precursor's concentration. The available Ce-YIG material research has mainly on single thin film crystals. Here a polycrystalline Ce-YIG, studied infrequently, have been produced using the sol-gel method and eventually its magneto-optical properties will be studied (Öztürk et al., 2008).

This thesis devoted to the research on YIG, Ce-YIG and Bi-YIG films prepared on pyrex glass and Si (100) substrates from solutions of Ce, Bi, Y and Fe alkoxide precursors, 2,4-pentanedionate, propionic acid, glacial acetic acid and hydrochloric acid using the sol-gel technique for magneto-optical technologies. Along this aim, turbidity, pH measurement and rheological properties of the prepared solutions were resolved. To define chemical structure and reaction type of intermediate temperature products and to use suitable process regime, differential thermal analysis-thermogravimetry (DTA-TG) and Fourier transform infrarared (FTIR) devices were used in the film production. The structural and microstructural properties of the coatings were extensively characterized using X-ray diffractometry (XRD), profilometer and scanning electron microscopy (SEM) plus energy dispersive spectroscopy (EDS). The magnetic and magneto-optic properties of thin films measured trough vibrating sample magnetometer (VSM) and magneto-optic system.

CHAPTER TWO
MAGNETO-OPTICAL PHONEMENON

2.1 Magnetic Sensors

Magnetic sensors have been in use for well over 2,000 years. Early applications were for direction finding, or navigation. Today, magnetic sensors are still a primary means of navigation but many more uses have evolved. The technology for sensing magnetic fields has also evolved driven by the need for improved sensitivity, smaller size, and compatibility with electronic systems.

A unique aspect of using magnetic sensors is that measuring magnetic fields is usually not the primary intent. Another parameter is usually desired such as wheel speed, presence of a magnetic ink, vehicle detection, or heading determination. These parameters can not be measured directly, but can be extracted from changes, or disturbances, in magnetic fields. Figure 2.1 shows other sensors, such as temperature, pressure, strain, or light that can be detected using an appropriate sensor. The output of these sensors will directly report the desired parameter. On the other hand, using magnetic sensors to detect direction, presence, rotation, angle, or electrical currents only indirectly detect these parameters. First, the enacting input has to create, or modify a magnetic field (DiBiccari, 2002).

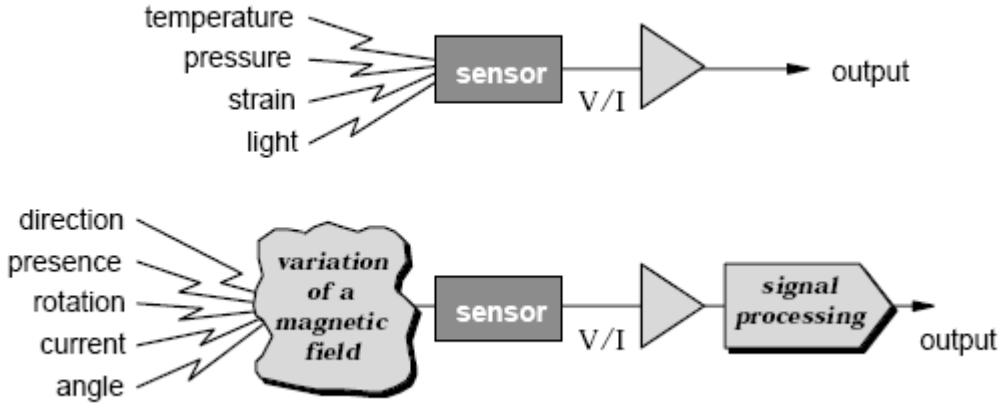

Figure 2.1 Comparison of conventional and magnetic sensors (DiBiccari, 2002)

A current in a wire, a permanent magnet, or sensing the Earth's magnetic field can create this field. Once the sensor detects that field, or change to a field, the output signal requires some signal processing to translate the sensor output into the desired parameter value. This makes magnetic sensing a little more difficult to apply in most applications, but it also allows for reliable and accurate sensing of parameters that are difficult to sense otherwise.

One way to classify the various magnetic sensors is by the field sensing range. These sensors can be arbitrarily divided into three categories—low field, medium field, and high field sensing. Sensors that detect magnetic fields less than 1 micro gauss will be classed low field sensors. Sensors with a range of 1 micro gauss to 10 gauss will be considered Earth's field sensors and sensors that detect fields above 10 gauss will be considered bias magnet field sensors for this research. Figure 2.2 indicates the various sensor technologies and illustrates the magnetic field sensing ranges (DiBiccari, 2002)

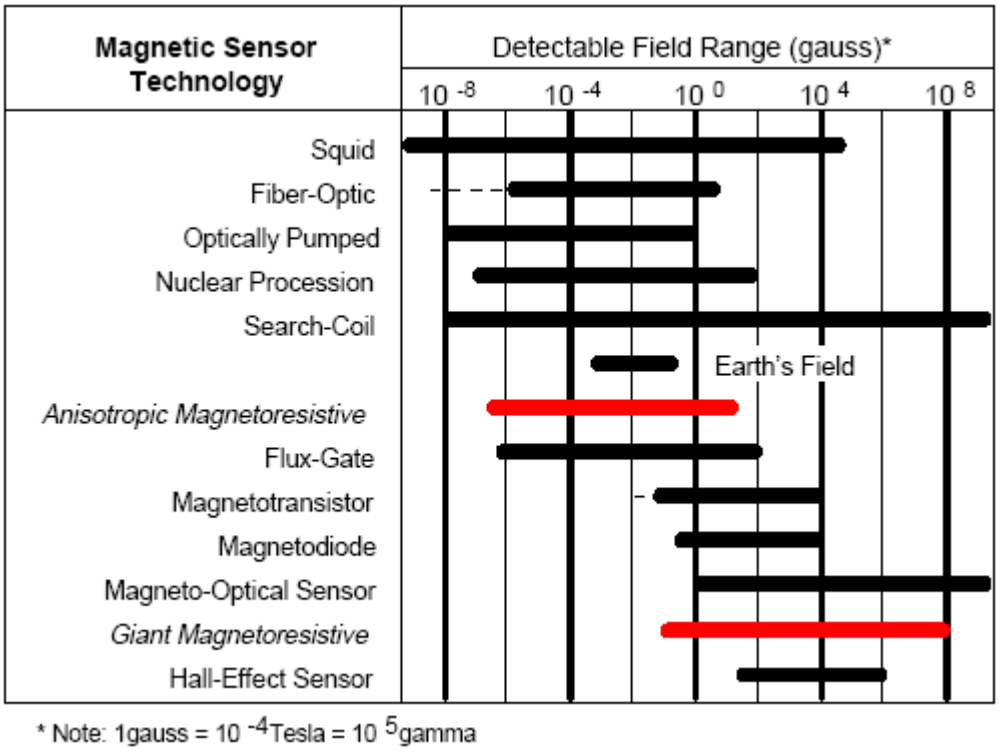

Figure 2.2 Magnetic sensor technologies according to field ranges (DiBiccari, 2002)

The material we will study, garnets are magneto-optical materials as can be seen in Figure 2.2. Magneto-Optical Sensors (MOS) are in the range of $10^0$and 10^8 Gauss. Light is a electromagnetic wave and it is affected from the electric field and magnetic field that present at the medium of interaction. To appreciate properly how magneto-optic ceramics function, it is first necessary to consider the nature of light and its interaction with materials.

2.2 Electromagnetic Wave Theory

James Clerk Maxwell (1831–1879), against a background of experimental and theoretical work by Andre´ Ampe`re (1775–1836). Karl Gauss (1777–1855) and Michael Faraday (1791–1867), developed the electromagnetic wave theory of light. Maxwell's equations describe how an electromagnetic wave originates from an accelerating charge and propagates in free space with a speed of $2.998x10^8$ m/s. An electromagnetic wave in free space comprises an electric field E and a magnetic induction field B which vibrate in mutually perpendicular directions in a plane normal to the wave propagation direction (Wikipedia Foundation, 2008). According to Maxwell's equations, a time-varying electric field generates a magnetic field and vice versa. Therefore, as an oscillating electric field generates an oscillating magnetic field, the magnetic field in turn generates an oscillating electric field, and so on. These oscillating fields together form an electromagnetic wave. Figure 2.3 indicates the propagation of light with the affects of both electrical field and magnetic field components.

Electromagnetic (EM) radiation is a self-propagating wave in space or through matter. EM radiation has an electric and magnetic field component which oscillate in phase perpendicular to each other and to the direction of energy propagation. Electromagnetic radiation is classified into types according to the frequency of the wave, these types include (in order of increasing frequency): radio waves, microwaves, terahertz radiation, infrared radiation, visible light, ultraviolet radiation, X-rays and gamma rays. Of these, radio waves have the longest wavelengths and Gamma rays have the shortest. A small window of frequencies, called visible

spectrum or light, is sensed by the eye of various organisms, with variations of the limits of this narrow spectrum. This spectrum is indicated in Figure 2.4.

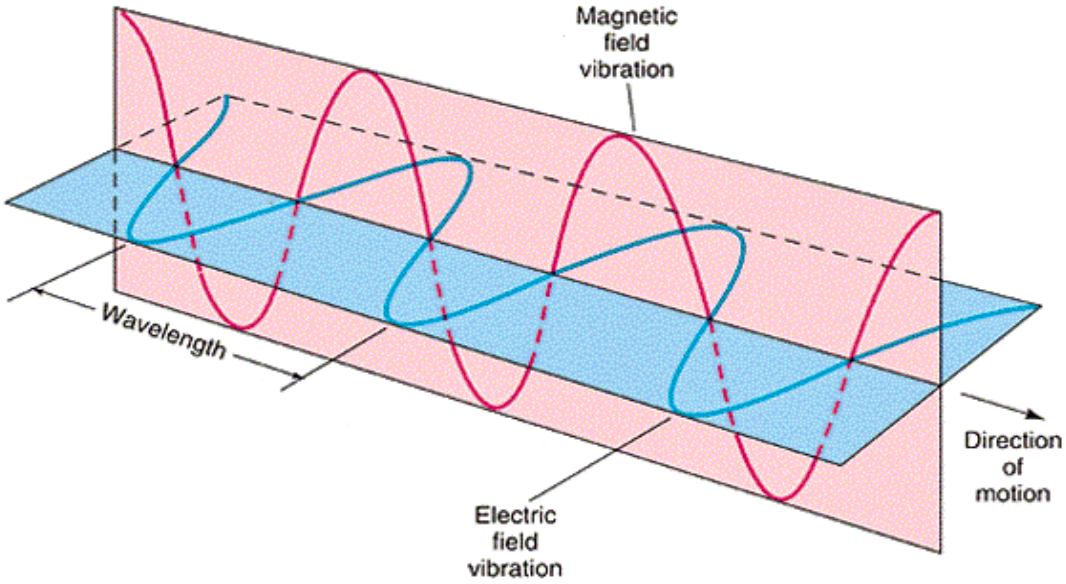

Figure 2.3 Electromagnetic wave propagating between electric and magnetic fields (Callister, 2009)

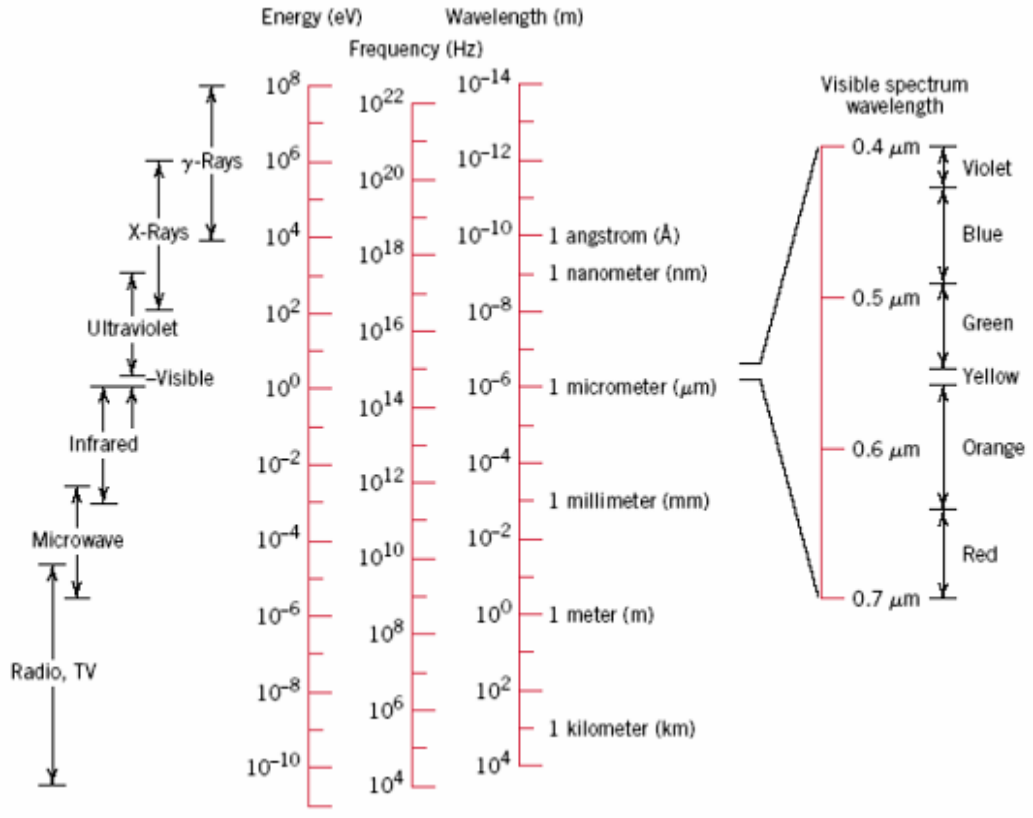

Figure 2.4 The electromagnetic spectrum (Callister, 2009)

In the classical sense, electromagnetic radiation is considered to be wave-like, consisting of electric and magnetic field components that are perpendicular to eachother and also to the direction of propagation (Figure 2.3). Light, heat (or radiant energy), radar, radio waves, and x-rays are all forms of electromagnetic radiation. Each is characterized primarily by a specific range of wavelengths, and also according to the technique by which it is generated. The **electromagnetic spectrum** of radiation spans the wide range from -rays (emitted by radioactive materials) having wavelengths on the order of m (nm), through x-rays, ultraviolet, visible, infrared, and finally radio waves with wavelengths as long as m. This spectrum is shown in Figure 2.4. Visible light lies within a very narrow region of the spectrum, with wavelengths ranging between about 0.4 (m) and 0.7 (m). The perceived color is determined by wavelength; for example, radiation having a wavelength of approximately 0.4 appears violet, whereas green and red occur at about 0.5 and 0.65 respectively. The spectral ranges for the several colors are included in Figure 2.4. White light is simply a mixture of all colors. The ensuing discussion is concerned primarily with this visible radiation, by definition the only radiation to which the eye is sensitive.

All electromagnetic radiation traverses a vacuum at the same velocity, that of light—namely, m/s (186,000 miles/s). This velocity, *c*, is related to the electric permittivity of a vacuum and the magnetic permeability of a vacuum through

$$c = \frac{1}{\sqrt{\in_0 \mu_0}} \tag{2.1}$$

Thus, there is an association between the electromagnetic constant *c* and these electrical and magnetic constants. Furthermore, the frequency and the wavelength of the electromagnetic radiation are a function of velocity according to

$$c = \lambda \nu \tag{2.2}$$

Frequency is expressed in terms of hertz (Hz), and 1 Hz cycle per second. Ranges of frequency for the various forms of electromagnetic radiation are also included in the spectrum (Figure 2.4).

Sometimes it is more convenient to view electromagnetic radiation from a quantum-mechanical perspective, in which the radiation, rather than consisting of waves, is composed of groups or packets of energy, which are called **photons.** The energy *E* of a photon is said to be quantized, or can only have specific values, defined by the relationship

$$E = h\nu = \frac{hc}{\lambda} \qquad (2.3)$$

where *h* is a universal constant called **Planck's constant,** which has a value of J-s. Thus, photon energy is proportional to the frequency of the radiation, or inversely proportional to the wavelength. Photon energies are also included in the electromagnetic spectrum (Figure 2.4).

When describing optical phenomena involving the interactions between radiation and matter, an explanation is often facilitated if light is treated in terms of photons. On other occasions, a wave treatment is more appropriate; at one time or another, both approaches are used in this discussion.

2.3 Polarization

The electric and magnetic vibrations of an electromagnetic wave occur in numerous planes. A light wave which is vibrating in more than one plane is referred to as **unpolarized light**. Light emitted by the sun, by a lamp in the classroom, or by a candle flame is unpolarized light. Such light waves are created by electric charges which vibrate in a variety of directions, thus creating an electromagnetic wave which vibrates in a variety of directions. This concept of unpolarized light is rather difficult to visualize. In general, it is helpful to picture unpolarized light as a wave which has

an average of half its vibrations in a horizontal plane and half of its vibrations in a vertical plane (Henderson, 1997).

Light can be represented as a transverse electromagnetic wave made up of mutually perpendicular, fluctuating electric and magnetic fields. Figure 2.5a shows the electric field in the xy plane, the magnetic field in the xz plane and the propagation of the wave in the x direction. Figur 2.5b shows a line tracing out the electric field vector as it propagates (Case Western University, 2009) . Polarization (also polarisation) is a property of waves that describes the orientation of their oscillations. According to the Maxwell equations, the direction of the magnetic field is uniquely determined for a specific electric field distribution and polarization (Wikipedia Foundation, 2008). Traditionally, only the electric field vector is dealt with because the magnetic field component is essentially the same (Case Western University, 2009).

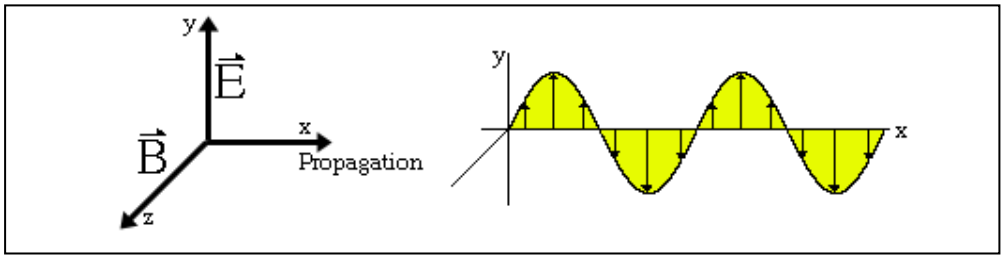

Figure 2.5 (a) Electrical field, magnetic field vectors and light propagation direction, and (b) electrical field vectors propagation. (Case Western University, 2009).

The simplest manifestation of polarization to visualize is that of a plane wave, which is a good approximation of most light waves (a plane wave is a wave with infinitely long and wide wavefronts). For plane waves the transverse condition requires that the electric and magnetic field be perpendicular to the direction of propagation and to each other. Conventionally, when considering polarization, the electric field vector is described and the magnetic field is ignored since it is perpendicular to the electric field and proportional to it. The electric field vector of a plane wave may be arbitrarily divided into two perpendicular components labeled *x* and *y* (with **z** indicating the direction of travel). For a simple harmonic wave, where the amplitude of the electric vector varies in a sinusoidal manner in time, the two components have exactly the same frequency. However, these components have two

other defining characteristics that can differ. First, the two components may not have the same amplitude. Second, the two components may not have the same phase, that is they may not reach their maxima and minima at the same time. Mathematically, the electric field of a plane wave can be written as,

$$\vec{E}(\vec{r},t) = \left(A_x \cdot \cos(kz - \omega t), A_y \cdot \cos(kz - \omega t + \phi), 0\right) \qquad (2.4)$$

where A_x and A_y are the amplitudes of the x and y directions and φ is the relative phase between the two components. The shape traced out in a fixed plane by the electric vector as such a plane wave passes over it (a Lissajous figure) is a description of the polarization state.

In the leftmost figure above, the two orthogonal (perpendicular) components are in phase. In this case the ratio of the strengths of the two components is constant, so the direction of the electric vector (the vector sum of these two components) is constant. Since the tip of the vector traces out a single line in the plane, this special case is called linear polarization. The direction of this line depends on the relative amplitudes of the two components (Wikipedia Foundation, 2008).

In the middle figure, the two orthogonal components have exactly the same amplitude and are exactly ninety degrees out of phase. In this case one component is zero when the other component is at maximum or minimum amplitude. There are two possible phase relationships that satisfy this requirement: the *x* component can be ninety degrees ahead of the *y* component or it can be ninety degrees behind the *y* component. In this special case the electric vector traces out a circle in the plane, so this special case is called circular polarization. The direction the field rotates in, depends on which of the two phase relationships exists. These cases are **called right-hand circular polarization** and **left-hand circular polarization**, depending on which way the electric vector rotates.

In all other cases, where the two components are not in phase and either do not have the same amplitude and/or are not ninety degrees out of phase, the polarization

is called elliptical polarization because the electric vector traces out an ellipse in the plane (**the polarization ellipse**). This is shown in the above figure on the right (Wikipedia Foundation, 2008).

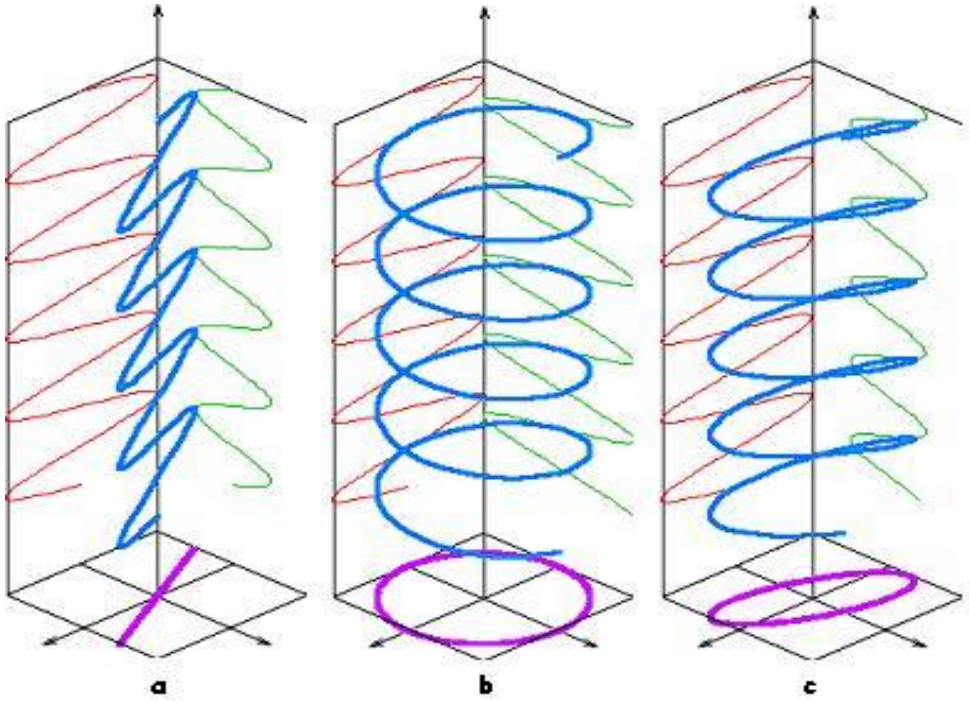

Figure 2.6 **(a)** Linear polarization, **(b)** Circularly polarization and **(c)** Elliptical polarization (Wikipedia Foundation, 2008).

2.3.1 Polarizers

It is possible to transform unpolarized light into polarized light. Polarized light waves are light waves in which the vibrations occur in a single plane. The process of transforming unpolarized light into polarized light is known as polarization. There are a variety of methods of polarizing light (Henderson, 1997).

Ordinary white light is made up of waves that fluctuate at all possible angles. Light is considered to be "linearly polarized" when it contains waves that only fluctuate in one specific plane. A polarizer is a material that allows only light with a specific angle of vibration to pass through. The direction of fluctuation passed by the polarizer is called the "easy" axis (Case Western University, 2009).

The most common method of polarization involves the use of a Polaroid filter. Polaroid filters are made of a special material which is capable of blocking one of the two planes of vibration of an electromagnetic wave. (Remember, the notion of two planes or directions of vibration is merely a simplification which helps us to visualize the wavelike nature of the electromagnetic wave.) In this sense, a Polaroid serves as a device which filters out one-half of the vibrations upon transmission of the light through the filter. When unpolarized light is transmitted through a Polaroid filter, it emerges with one-half the intensity and with vibrations in a single plane; it emerges as polarized light (Henderson, 1997).

If two polarizers are set up in series so that their optical axes are parallel, light passes through both. However, if the axes are set up 90 degrees apart (crossed), the polarized light from the first is extinguished by the second. As the angle rotates from 0 to 90 degrees, the amount of light that is transmitted decreases. This effect is demonstrated in the Figure 2.7. The polarizers are parallel at the top and crossed at the bottom (Case Western University, 2009).

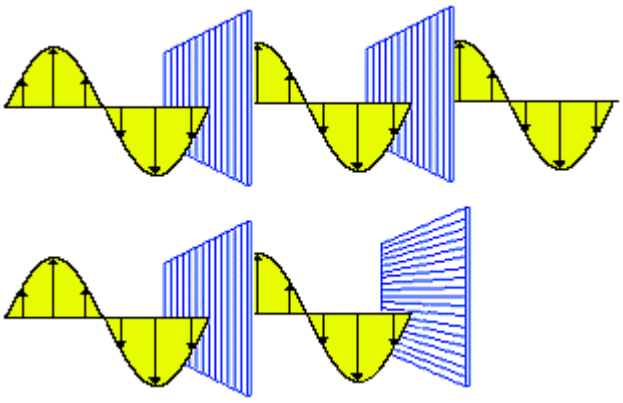

Figure 2.7 Interactions between polarizer and unpolarized light (Case Western University, 2009).

2.4 Classification of Magnetic Materials

Magnetic materials are those materials that can be attracted or repelled by a magnet and be magnetized themselves. The magnetic properties of materials are of microscopic origin, especially atomic. Actually, magnetism in materials comes from

the orbital motion and spin angular momentum of electrons in the atoms. According to Maxwell's theory of magnetism, electric charges in motion form small magnetic dipole moments that react to an applied magnetic or electric field strength. Even if nuclear magnetism exists, its contribution to the overall atomic magnetism is seldom too low owing to the several orders of magnitude existing between the Bohr and nuclear magnetons ($\mu B/\mu N = 1847$).

There exist five classes of magnetic materials:
(i) diamagnetic materials or diamagnets,
(ii) paramagnetic materials or paramagnets,
(iii) ferromagnetic materials or ferromagnets,
(iv) antiferromagnetic materials or antiferromagnets and
(v) ferrimagnetic materials or ferrimagnets (Cardarelli, 2008).

2.4.1 Diamagnetic Materials

When an external magnetic field ***H*** is applied to a diamagnetic material (or diamagnet), the atomic electronic orbitals are strongly modified owing to the deviation of electron trajectory by the magnetic field according to Laplace's law. Therefore, a spontaneous induced magnetic field appears and it opposes the variations of the external magnetic field as predicted by Lenz's law. Actually, despite the weakness of the magnetic dipole moment of the atoms, they orientate along the field lines in order to compensate the external magnetic field. This behavior is totally reversible, and the random magnetic moment orientation is restored when the application of the external field has ceased. In conclusion, diamagnetism originates from an induced current opposing the external applied magnetic field. For this reason, diamagnetic materials exhibit small and negative magnetic susceptibilities ($\chi_m \approx -10^{-5}$), that is, their relative magnetic permeabilities are slightly below unity ($\mu_r < 1$). As a general rule, because diamagnetism originates from orbital deformation under an applied external magnetic field, all materials obviously have a basic diamagnetic component. In diamagnetic materials, the magnetic susceptibility can be accurately predicted by Langevin's classical theory of electromagnetism as follows:

$$\chi_m = -\mu_0 n Z e^2 \langle r_2 \rangle / 6m_0, \quad (2.5)$$

where, μ_0 the magnetic permeability of a vacuum in $H.m^{-1}$, Z the atomic number of the atom, n the atomic density in m^{-3}, e the elementary charge in C, $\langle r_2 \rangle$ the root mean square of the square of the atomic radius in m^2. Examples of diamagnetic materials are given in Table 2.1, which explains magnetic susceptibilities and magnetic permeabilities of diamagnets.

Table 2.1 Magnetic susceptibilities and magnetic permeabilities of diamagnets (Cardarelli, 2008)

Diamagnets	**Magnetic susceptibilities ($10^6\chi$)**	**Relative magnetic permeabilities (μ_r)**
Silicon (Si)	-0,2965	0,999999704
Germanium (Ge)	-0,6354	0,999999365
Bismuth (Bi)	-1,3186	0,999998681
Gallium (Ga)	-1,4102	0,999998590
Graphite (C)	-1,1150	0,999998885

2.4.2 Paramagnetic Materials

For paramagnetic materials (or ***paramagnets***), the magnetism's origin is due to the partial alignment of existing magnetic dipole moments, which are randomly oriented by thermal agitation in the absence of an applied external magnetic field. When an external field is applied to the material, all the magnetic dipole moments orientate along the field lines and increase locally the magnetic field value. Paramagnetic materials have a positive value of magnetic susceptibility, commonly ranging from $+10^{-6}$ to $+10^{-2}$. Hence, their relative magnetic permeability is slightly above unity ($\mu_r > 1$). For instance, paramagnetic materials include gases such as oxygen and all the chemical elements not listed in the previous paragraph dealing with diamagnets such as Li, Na, Mg, Al, Ti, Zr, Sn, Mn, Cr, Mo, and W and all the platinum-group metals: Ru, Rh, Pd, Os, Ir, Pt. On the other hand, the magnetic susceptibility of paramagnetic materials decreases with an increase in temperature. The temperature dependence of the magnetic susceptibility of paramagnetic materials is given by the Curie–Weiss law described by the following equation:

$$\chi_m = \mu_0 n m^2 / \left[3k\left(T - T_c\right)\right] = C / \left(T - T_c\right) \quad (2.6)$$

where μ_0 is the magnetic permeability of a vacuum in $H.m^{-1}$, n the atom density in m^{-3}, m the microscopic dipolar magnetic moment of an atom in $A.m^2$, k the Boltzmann constant in $J.K^{-1}$, T the absolute thermodynamic temperature in K, TC the paramagnetic Curie temperature in K, at which the susceptibility reaches its maximum value, and C the paramagnetic Curie constant in K^{-1} (Cardarelli, 2008).

2.4.3 Ferromagnetic Materials

Ferromagnetic materials have magnetic dipolar moments aligned parallel to each other even without an external applied magnetic field. Particular zones in the material where all the magnetic dipole moments exhibit the same orientation are called **magnetic domains** or **Weiss domains**. Interfaces between the Weiss domains are called **Bloch boundaries** or **walls**. For instance in a polycrystalline material, crystal borders that separate different lattice orientations are Bloch walls. Nevertheless, either within a single crystal of a polycrystalline material or monocrystal, several magnetic domains can coexist. Therefore, the entire macroscopic material is divided into small magnetic domains, each domain having a net magnetization even without an external field. This magnetization is called spontaneous magnetization (MS). However, a bulk sample will generally not have a net magnetization since the sum of all spontaneous magnetization vectors in the various domains is zero due to their random orientations. But application of a small external magnetic field will cause growth of favorable domains resulting in materials having a high magnetization and a high magnetic susceptibility (roughly 10^6). Therefore, their relative magnetic permeabilities are largely above unity. The main elements that exhibit ferromagnetism are the three transition metals of group VIIIB such as Fe, Co, and Ni and some lanthanides such as Gd, Tb, Dy, Ho, and Tm, crystalline compounds such as MnAs, MnBi, MnSb, CrO_2, and Fe_3C, and alloys or intermetallic compounds containing Fe, Co, and Ni (e.g., steel, mumetal, AlNiCo, peralloy). However, above a certain critical temperature, called the **Curie temperature**, T_c, these materials lose their spontaneous magnetization and become paramagnetic. There are two main requirements for an atom of an element to be ferromagnetic. First, the atom must have a total angular momentum different from zero ($J \neq 0$). This atomic condition is completed when neither electronic nonspherical

subshell 3-d nor 4-f is completely filled and the sum of the spin angular momenta of all the electrons is not zero. The second condition is based on thermodynamics; it is dependent on the sign of the difference between the electronic repulsion energy between Fermi gases of two adjacent atoms and the energy from the repulsion of electrons having the same spin. The total energy variation is positive for ferromagnetic materials, while it is negative for nonferromagnetic materials (e.g., Pt, Mn, and Cr). The physicist Slater has established a practical criterion to determine the ferromagnetic character of a material. This criterion is the ratio between the equilibrium radius between two adjacent atoms in the solid and the average orbital radius of electrons in 3-d or 4-f subshells. When this ratio is above 3, the material is ferromagnetic, while for those whose ratio is below 3, the material does not exhibit ferromagnetic properties. Table 2.2 shows properties of some of the ferromagnetic materials (Cardarelli, 2008).

Table 2.2 Properties of some ferromagnetic elements (Cardarelli, 2008)

Kimyasal Element	**Fe**	**Co**	**Ni**	**Gd**	**Tb**	**Dy**	**Er**
Curie Temperature (T_c/K)	1043,15	1394,15	631,15	292,15	222	87	32
Saturation Magnetization (B_s/T) at 4 K	2,193	1,797	0,656	2,470	3,430	3,750	3,410
Relative Atomic Dipol Magnetic Moment (μ/μ_B)	2,22	1,7	0,62	7	9	10	9

2.4.4 Anti-ferromagnetic Materials

Antiferromagnetic materials have an antiparallel arrangement of equal spins resulting in a very low magnetic susceptibility similar to that of paramagnetic materials. The spin arrangement of antiferromagnetic materials is not stable above a critical temperature, called the Néel Temperature, T_N. For instance, antiferromagnetic materials are chromium and manganese, some rare-earth metals, transition metal oxides such as MnO, FeO, and NiO, and other solids such as MnS, CrSb, $FeCO_3$, and MnF_2 (Cardarelli, 2008).

2.4.5 Ferrimagnetic Materials

Ferrimagnetic materials have two kinds of magnetic ions with unequal spins, oriented in an antiparallel fashion. The spontaneous magnetization can be regarded as the two opposing and unequal magnetizations of the ions on the two sublattices. Ferrimagnetic materials become paramagnetic above a certain Curie temperature and properties of some of them were listed in Table 2.3 (Cardarelli, 2008).

Table 2.3 Properties of some ferrimagnetic garnets (Cardarelli, 2008)

Ferrit/Garnet Type	**Chemical Formula**	**Structure type Crystal structure**	**Magnetic Induction Saturation (B_s/T)**	**Curie Temperature (T_c/^{o}C)**
Eu-Fe Garnet	$Eu_3Fe_5O_{12}$	Garnet type Cubic	0,116	293
Gd-Fe Garnet	$Gd_3Fe_5O_{12}$	Garnet type Cubic	0,017	291
Manghemite	γ -Fe_2O_3	Spinel Type Cubic	0,52	575
Sm-Fe Garnet	$Sm_3Fe_5O_{12}$	Garnet type Cubic	0,170	305
Y-Fe Garnet	$Y_3Fe_5O_{12}$	Garnet type Cubic	0,178	292

2.5 Magneto-optical Effects

MOS properties can be summarized by magneto-optical effect relations. Thus, a magneto-optic effect is any one of a number of phenomena in which an electromagnetic wave propagates through a medium that has been altered by the presence of a quasistatic magnetic field.

In such a material, which is also called gyrotropic or gyromagnetic, left- and right-rotating elliptical polarizations can propagate at different speeds, leading to a number of important phenomena. When light is transmitted through a layer of magneto-optic material, the result is called the Faraday effect: the plane of polarization can be rotated, forming a Faraday rotator. The results of reflection from a magneto-optic material are known as the magneto-optic Kerr effect as schematized in Figure 2.8 (Wikipedia Foundation, 2008).

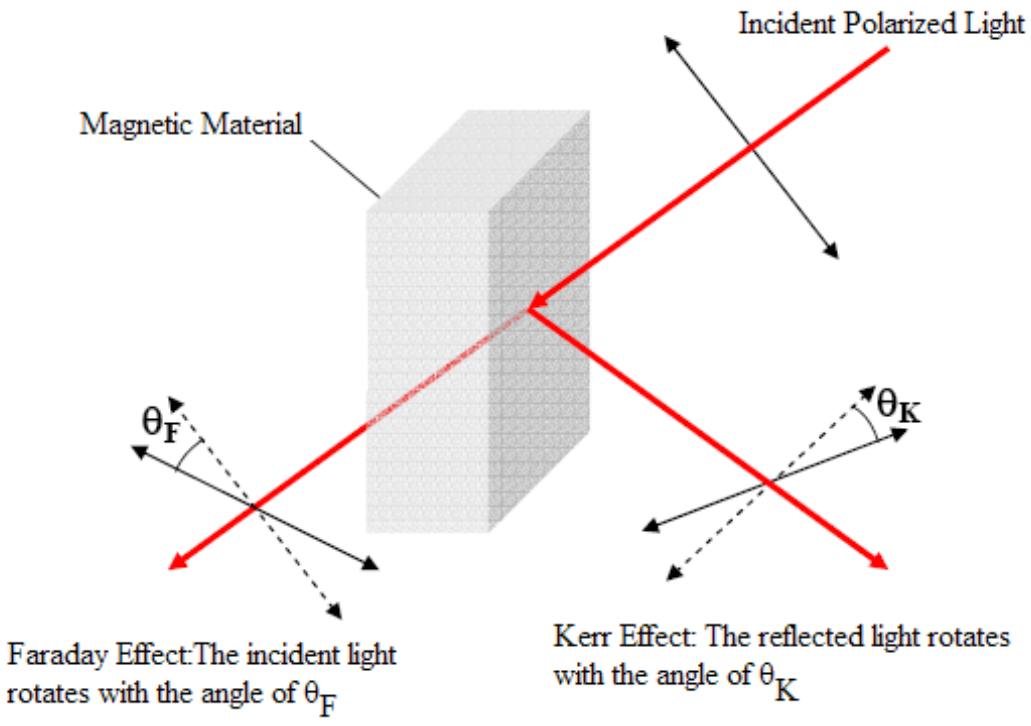

Figure 2.8 Kerr and Faraday effects (Wikipedia Foundation, 2008)

2.5.1 Faraday Effect

Faraday effect or Faraday rotation is a magneto-optical phenomenon, or an interaction between light and a magnetic field in a dielectric material. The rotation of the plane of polarization is proportional to the intensity of the component of the magnetic field in the direction of the beam of light.

The Faraday effect, discovered by Michael Faraday in 1845, was the first experimental evidence that light and electromagnetism are related. The theoretical basis for that relation, now called electromagnetic radiation, was further developed by James Clerk Maxwell in the 1860s and 1870s. This effect occurs in most optically transparent dielectric materials (including liquids) when they are subject to strong magnetic fields (Wikipedia Foundation, 2008).

The Faraday effect is a result of ferromagnetic resonance when the permittivity of a material is represented by a tensor. This resonance causes waves to be decomposed into two circularly polarized rays which propagate at different speeds, a property known as circular birefringence. The rays can be considered to re-combine upon emergence from the medium, however owing to the difference in propagation speed they do so with a net phase offset, resulting in a rotation of the angle of linear polarization. Figure 2.9 indicates polarization of rotation of light due to faraday effect (Wikipedia Foundation, 2008).

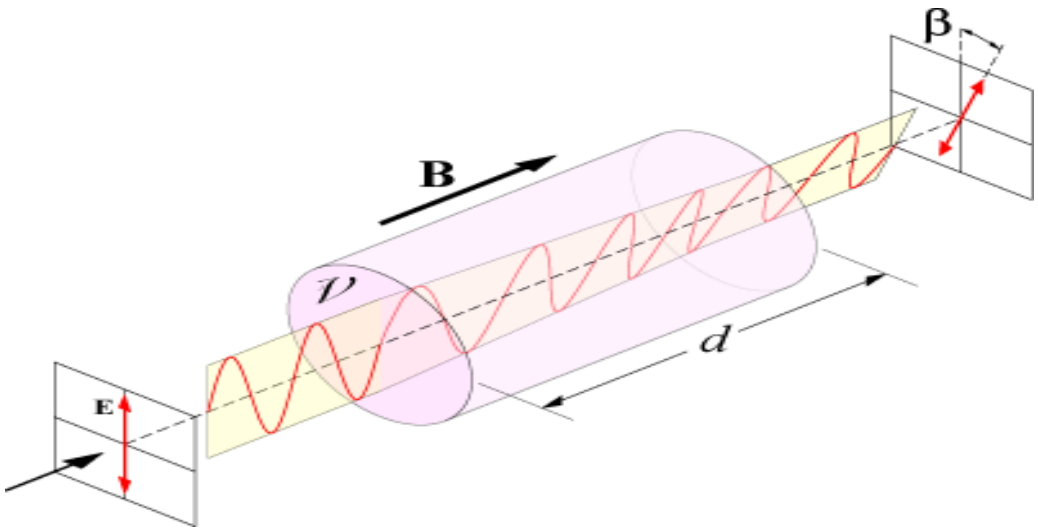

Figure 2.9 Polarization of rotation of light due to Faraday Effect (Wikipedia Foundation, 2009)

The relation between the angle of rotation of the polarization and the magnetic field in a diamagnetic material is:

$$\beta = \upsilon . B . d \qquad (2.1)$$

where, β is the angle of rotation (in radians); B is the magnetic flux density in the direction of propagation (in teslas); d is the length of the path (in meters) where the light and magnetic field interact; and υ is the Verdet constant for the material. This is empirical proportionality constant.

A positive Verdet constant corresponds to L-rotation (anticlockwise) when the direction of propagation is parallel to the magnetic field and to R-rotation

(clockwise) when the direction of propagation is anti-parallel. Thus, if a ray of light is passed through a material and reflected back through it, the rotation doubles.

Faraday rotation is an unique value of materials which posses magnetic properties. Materials for different applications could be chosen according to area of application. Table 2.4 lists several materials and their faraday rotations. Due to increase or decrease the value of rotation for a distinct material substitution is effective for a standard material. Researchers reported that the optimum rotation for an application is could be decided according to the substituent concentration of Bi for $Y_{(3-x)}Bi_{(x)}Fe_5O_{12}$ (Wikipedia Foundation, 2009).

Some materials, such as terbium gallium garnet (TGG) have extremely high Verdet constants. By placing a rod of this material in a strong magnetic field, Faraday rotation angles of over 0.78 rad (45°) can be achieved. This allows the construction of Faraday rotators, which are the principal component of Faraday isolators, devices which transmit light in only one direction. Similar isolators are constructed for microwave systems by using ferrite rods in a waveguide with a surrounding magnetic field.

Table 2.4 Faraday rotations of several magnetic materials (Wikipedia Foundation, 2009)

Material	Rotation (Deg)	Material	Rotation (Deg)
Fe	$3.825 \cdot 10^5$	$NdFeO_3$	$4.72 \cdot 10^4$
Co	$1.88 \cdot 10^5$	$CrBr_3$	$1.3 \cdot 10^5$
Ni	$1.3 \cdot 10^5$	EuO	$5 \cdot 10^5$
$Y_3Fe_5O_{12}$	250	MnBi	$5.0 \cdot 10^5$
$Gd_2BiFe_5O_{12}$	$1.01 \cdot 10^4$	$YFeO_3$	$4.9 \cdot 10^3$

2.5.2 Kerr Effect

Magneto-optic Kerr effect (MOKE) is one of the magneto-optic effects. It describes the changes of light reflected from magnetized media. The light that is reflected from a magnetized surface can change in both polarization and reflectivity. The effect is identical to the Faraday effect except that the magneto-optical Kerr effect is a measurement of the reflected light, while the Faraday effect is a measurement of the transmitted light. Both effects result from the off-diagonal components of the dielectric tensor ε (Wikipedia Foundation, 2009).

MOKE can be further categorized by the direction of the magnetization vector with respect to the reflecting surface and the plane of incidence. The different types of MOKE are illustrated in Figure 2.10. Also in Table 2.5 the Kerr rotations of some materials are listed.

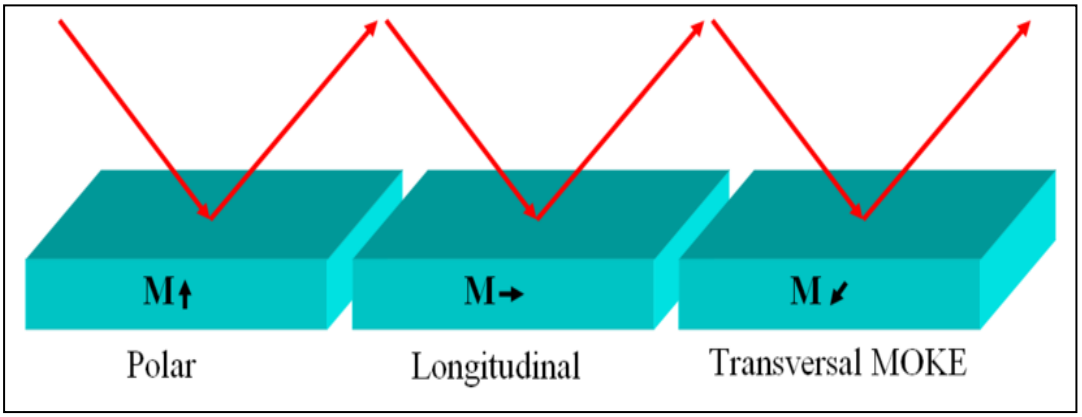

Figure 2.10 Different types of MOKE according to the magnetization (Wikipedia Foundation, 2009)

Table 2.5 Kerr rotations of several magnetic materials (Wikipedia Foundation, 2009)

Material	Rotation (Deg)	Material	Rotation (Deg)
Fe	0.87	MnBi	0.7
Co	0.85	PtMnSb	2.0
Ni	0.19	CoS_2	1.1
Gd	0.16	$CrBr_3$	3.5
Fe_3O_4	0.32	CeSb	90

2.5.2.1 Polar MOKE

When the magnetization vector is perpendicular to the reflection surface and parallel to the plane of incidence, the effect is called the polar Kerr effect. To simplify the analysis, near normal incidence is usually employed when doing experiments in the polar geometry (Akdoğan, 2004). The illustration of polar MOKE is represented in Figure 2.11.

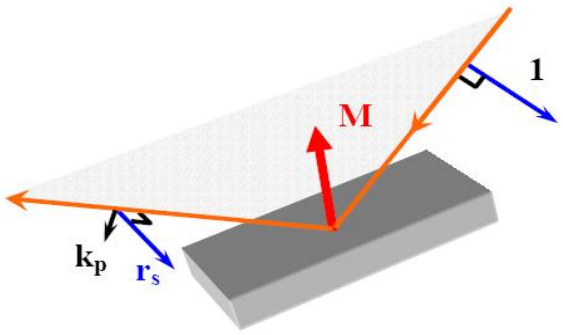

Figure 2.11 Polar MOKE (Akdoğan, 2004)

2.5.2.2 Longitudinal MOKE

In the effect, the magnetization vector is parallel to both the reflection surface and the plane of incidence. The longitudinal setup involves light reflected at an angle from the reflection surface and not normal to it, as above in the polar MOKE case. In the same manner, linearly polarized light incident on the surface becomes elliptically polarized, with the change in polarization directly proportional to the component of magnetization that is parallel to the reflection surface and parallel to the plane of incidence. This elliptically polarized light to first-order has two perpendicular E vectors, namely the standard Fresnel amplitude coefficient of reflection r and the Kerr coefficient k. The Kerr coefficient is typically much smaller than the coefficient of reflection. The illustration of Longitudinal MOKE is shown in Figure 2.12.

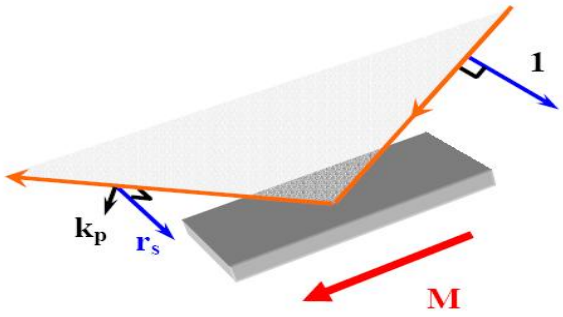

Figure 2.12 Longitudiual MOKE (Akdoğan, 2004)

2.5.2.3 Transversal MOKE

When the magnetization is perpendicular to the plane of incidence and parallel to the surface it is said to be in the *transverse* configuration. In this case, the incident light is also not normal to the reflection surface but instead of measuring the polarity of the light after reflection, the reflectivity *r* is measured. This change in reflectivity is proportional to the component of magnetization that is perpendicular to the plane of incidence and parallel to the surface, as above. If the magnetization component points to the right of the incident plane, as viewed from the source, then the Kerr vector adds to the Fresnel amplitude vector and the intensity of the reflected light is $| r + k |^2$. On the other hand, if the component of magnetization component points to the left of the incident plane as viewed from the source, the Kerr vector subtracts from the Fresnel amplitude and the reflected intensity is given by $| r - k |^2$ (Wikipedia Foundation, 2009).

2.6 Magneto-optical Materials

New technological applications such as magnetic sensor, optical wave-guides, magneto-optical modulator and integrated magneto-optic devices require improved sensitivity, smaller size and compatibility with electronic systems. For such applications, materials with a good magneto-optic property are of a significant issue. Number of magneto-optic materials is available e.g., flint glass (SF_6), BSO ($Bi_{12}SiO_2$), BGO ($Bi_{12}GeO_{20}$) and garnets. Garnets have more appeal due to their large magneto-optical response. Yttrium iron garnet ($Y_3Fe_5O_{12}$: YIG) having

promising magnetic and magneto-optic properties is the most suitable material for these applications (DiBiccari, 2002).

2.6.1 Flint Glass (SF6)

Flint glass is optical glass that has relatively high refractive index and low Abbe number. Flint glasses are arbitrarily defined as having an Abbe number of 50 to 55 or less. The currently known flint glasses have refractive indices ranging between 1.45 and 2.00. A concave lens of flint glass is commonly combined with a convex lens of crown glass to produce an achromatic doublet lens because of their compensating optical properties (Kurkjian et al., 1998).

2.6.2 BSO ($Bi_{12}SiO_2$) and BGO ($Bi_{12}GeO_{20}$)

$Bi_{12}SiO_{20}$ (BSO) and $Bi_{12}GeO_{20}$ (BGO) are cubic crystals, containing two molecular units per unit cell. Some of the properties making these materials of technological interest include low ultrasonic velocity, small acoustic damping up to 1 GHz, and large piezoelectric, photorefractive, photoelastic, magnetooptic and electrooptic (nonlinear index) effects. Although being cubic results in isotropic intensity transmission and reflection properties for linearly polarized light, both crystals are gyrotropic, showing optical activity, the rotation of the plane of polarization of linearly polarized light being proportional to the thickness of the crystal (Kurkjian et al., 1998).

2.6.3 Garnets

Magnetic garnets have proven useful as MO devices because of their large Faraday rotations relative to other materials. Numerous studies involving magnetic garnets used as waveguides have inspired further exploration using rare earth iron garnets as possible media for next generation MO recording media. Uses include electronic device sensors, magnetic bubbles used in logic operation, and memory elements for electronic computers (Öztürk et al., 2008).

The general formula for the ferrimagnetic garnets is written as $R_3Fe_5O_{12}$, where R stands for yttrium in the case of YIG; the yttrium can be totally or partially replaced by one of the lanthanides such as lanthanum, cerium, neodymium, gadolinium etc. Therefore the structure contains two types of magnetic ion, iron and one of the rare earth group. Whilst the contribution to the magnetization from the orbital motion of the electrons in elements of the first transition series is close to zero (quenching) because of the orbital–lattice coupling that of the electrons in the lanthanide ions has a significant effect. The unpaired electrons of the first series elements are in the outermost 3d group and therefore are not shielded from the crystal field which is responsible for quenching. In the lanthanide ions the unpaired electrons in the 4f group are shielded by the 5s5p electrons and there is therefore an orbital contribution in addition to that of the unpaired spins. As a consequence the contribution of the lanthanide ions to the magnetization is somewhat greater than would be estimated from the simple rules governing the elements of the first transition series. A further consequence of this shielding is that the coupling of lanthanide ions to other magnetic ions is weaker than that between the ions of the first transition series (Moulson, 2003).

The material chosen for the development of a MO film was substituted YIG. YIG has been used as an optical isolator in fiber optics and recently has been produced with rare earth and aluminum substitutions (R, Al: YIG), where R= Bi, Gd, Er, Ho, etc. Faraday rotations of 50°/μm have been achieved with Bi, Al: YIG as compared with 12°/μm for YIG (Öztürk et al., 2008).

YIG has a complex cubic structure, shown in Figure 2.13 and some physical properties illustrated in Table 2.6. Note that iron occupies two different sites in the structure. The MO effect derives from the interaction of the iron atoms when exposed to a magnetic field. Bismuth or another rare earth element strengthens the effect by their diamagnetic properties (DiBiccari, 2002).

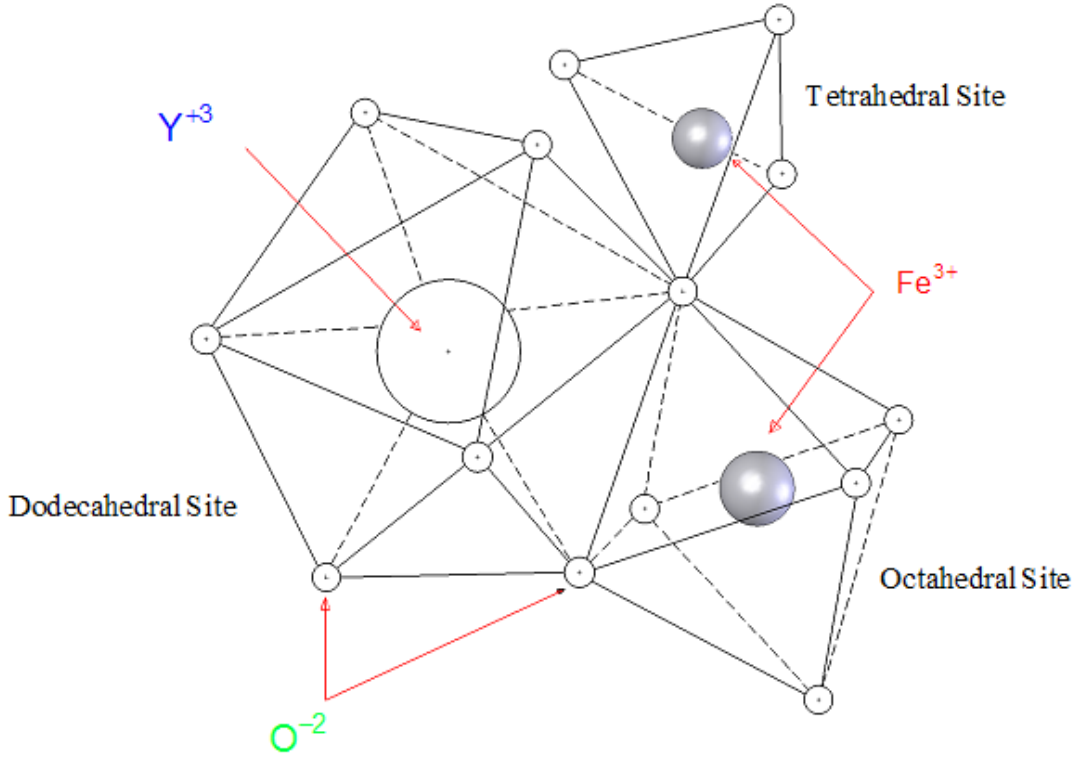

Figure 2.13 YIG crystal structure

A simplified depiction of the structure provides clarity into understanding the magnetization observed, shown in Figure 2.14. The ferrimagnetic garnets have the Formula;

$$(3M_2O_3)_c(2Fe_2O_3)_a(3Fe_2O_3)_d \qquad (2.2)$$

with

- $6Fe_d(30\mu_B)\uparrow$
- $4Fe_d(20\mu_B)\downarrow$
- $6M_c\downarrow$

M a trivalent rare-earth ion or yttrium ion. The subscripts show cation (a) is located in an octahedral site with 6 oxygen ions surrounding; (c) is a dodecahedral site surrounded with 8 oxygen ions; (d) surrounded with 4 oxygen ions forming a tetrahedral site. A single cubic cell of ferromagnetic garnet contains 160 atoms with a side being 8 molecules of $Fe_2Fe_3M_3O_{12}$, or approximately 12.4 A^o depending upon

M. The magnetic moment arises from the antiparallel coupling between (a) and (d) ions with the (c) ion oriented antiparallel to the (d) ion. The net moment, m_s, in Bohr magnetons per unit formula $3M_2O_3 \cdot 5Fe_2O_3$ is;

$$m_s = 6\, m_c - (6\, m_d - 4\, m_a) = 6\, m_c - 10\, \mu_B \qquad (2.3)$$

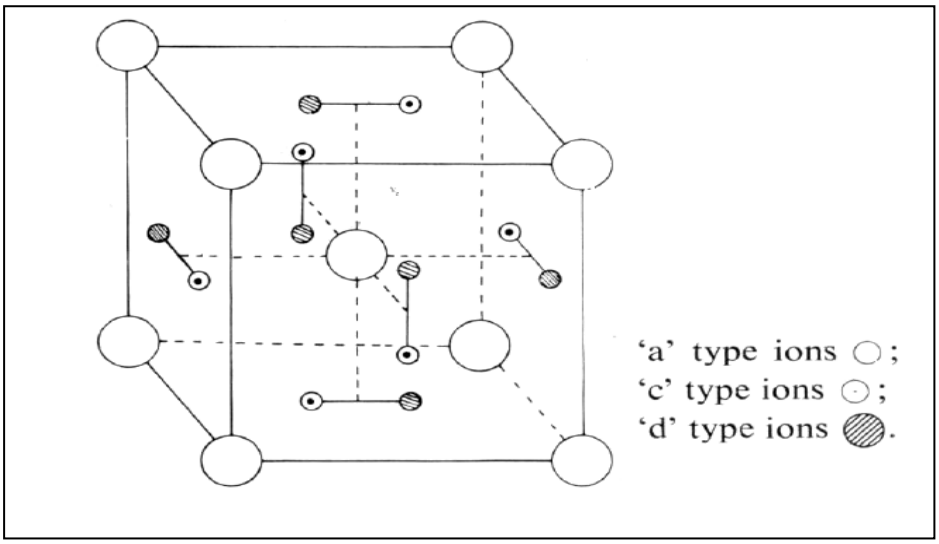

Figure 2.14 Simplified garnet structure of unit $(Fe_2)_a\ (Fe_3)_d\ (M_2)_cO_{12}$, (DiBiccari, 2002)

Table 2.6 Physical properties of YIG

Property at 25° C	Pure YIG
Empirical Formula	$Y_3Fe_5O_{12}$
Molecular Weight (grams)	737.95
Crystal Structure	Cubic
Density (g-cm^3)	5.17
Melting Point (°C)	1555
Hardness (moh)	6.5 to 7.0
Lattice Constant (Å)	12.376
Saturation Magnetization (Gauss)	1780

Property at 25^{o} C (Continue)	Pure YIG
Magnetic Anisotropy (erg/cm^{3})	-6.20 x 10^{-3}
Electrical Resistivity (Ù/cm)	1 x 10^{14}
Young's Modulus	2 x 10^{12}
Poisson's Ratio	0.29
Dielectric Constant	15.0
Curie Temperature (K)	553
Thermal Conductivity (W/cm^{-1}/^{o}C^{-1})	0.074
Thermal Expansion Coefficient (^{o}C^{-1})	1.04 x 10^{-5}
Refractive index, 1310 nm	2.20
Faraday Rotation, 1310 nm (^{o}mm^{-1})	21.4
Transmittance1 (%)	$\geq$95
Magneto-optical Sensitivity (^{o}A^{-1})	0.14

2.6.3.1 Effect of Dopping on Properties of Garnets

The general formula for the ferrimagnetic garnets is written $R_3Fe_5O_{12}$, where R stands for yttrium in the case of YIG; the yttrium can be totally or partially replaced by one of the lanthanides such as lanthanum, cerium, neodymium, gadolinium etc (Moulson, 2003).

The lattice site occupancy is conventionally represented by the Formula $\{R_3\}c[Fe_2]a(Fe_3)dO_{12}$, where [ ]a indicates ions on octahedral sites, ( )d indicates ions on tetrahedral sites and { }c indicates ions on 12-coordinated sites. R^{3+} ion cannot occupy the octahedral and tetrahedral sites because of its large ion radius, so R^{3+} ion can only occupy dodecahedral sites which have larger space. In the case of ferrimagnetic garnet $R_3Fe_5O_{12}$, the ion distribution structure can be represented by writing the garnet Formula as *{*R_3*}*$[Fe_2](Fe_3)O_{12}$, *{ }*, [ ], ( ) representing 24c (dodecahedral), 16a (octahedral) and 24d (tetrahedral), respectively. As we all know, YIG is the most representative and well-known compound among the rare-earth-iron

garnets, and various magnetization can be achieved by substitution in the YIG (Haitao et al., 2008).

The existence of crystallographic sites of different size makes it possible to substitute into YIG (a prototype of iron garnet) a wide variety of ions with different ionic radii and valence states. Normally, metal ions with larger ion diameters such as Ca, Bi, Pb, Y, Ho, Dy, Gd, Eu, Sm, Na, Pr and La occupy *c* site; smaller ones such as Al, Ga are prefer to occupy the *a* site. It is possible for them to be in *d* site too.

Bi substitutes Y ions in *c* site will increase the Curie temperature, Faraday rotation, etc. Al or Ga ions in d site instead of the Fe ions causes a decreasing of the total moment of per unit and a decreasing Curie temperature. When Ga ion at tetrahedral sites, it can cause a low temperature magnetization abnormaly, the magnetization start to decrease below 35K Dy in *c* site is usually used to increase the anisotropy because of the largest negative magnetostriction coefficient of DyIG. Cu is effective in increasing coercive field the H_c with pinning effect (Öztürk et al. 2008).

YIG is substituted to improve magneto-optic properties, yttrium may be substituted by one of the lanthanides e.g., lanthanum, cerium, neodymium, gadolinium and so on. Its unit cell includes different magnetic ions, iron and one of the rare earth groups. Its magnetic property arises from the antiparallel ordering between Fe^{3+} ions in the a-site and d-site as a result of exchange couplings between the ions but the c-site ions couple weekly leading to cant-parallel to the d-site ion. The net magnetic moment of YIG per unit cell is 40 Bohr magnetrons. Its saturation magnetization is 136 kA/m at room temperature. With Ce addition, paramagnetic trivalent Ce^{3+} ions are replaced with non-magnetic Y^{3+} ions in c-sites (Öztürk et al. 2008).

Magneto-optic effect arises after the change of the state of the polarization of light due to interaction with a magnetic material discovered by M. Faraday who found that a polarized light was rotated after passing through a glass under an external magnetic

field along the direction of propagation of incoming light. For a magnetic field perpendicular to incoming light similar rotation was also observed now known as Voigt effect. Magneto-optical effects for the YIG type and its variants can be explained macroscopically via difference in the refraction indices for right and left circularly polarized light hence it is quite often called circular birefringence. There is also similar effect of the circular dichroism arises from the absorbance differences for left and right circularly polarized light. Yet both effect can be attributed usually to the Zeeman effect, i.e., two degenerate electronic state split into two circular components which worked well for Bi-YIG. For different applications the choice of appropriate garnet choice is done according to saturation magnetization as shown in Figure 2.16. Also, for sensitive temperature usages of garnets the substituted ions are very important. According to this aim, the choice of appropriate substitution is decided via Figure 2.15.

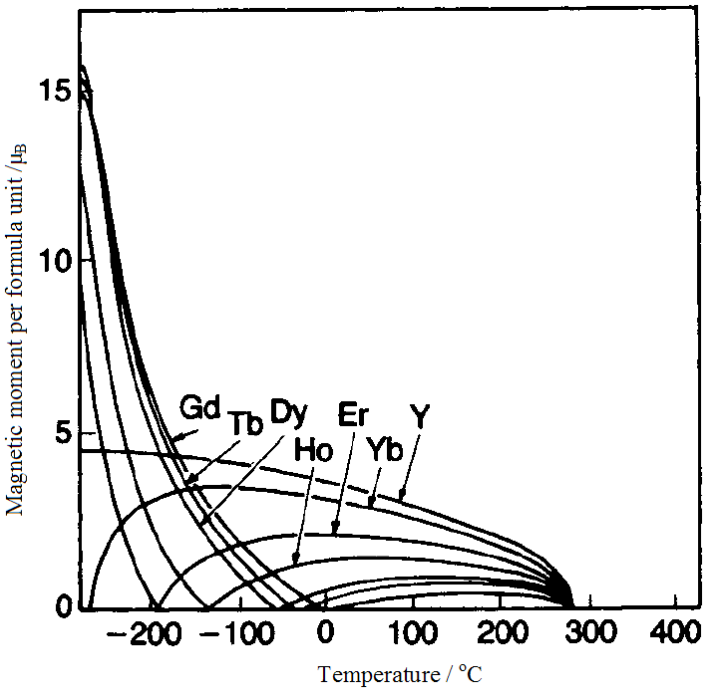

Figure 2.15 Saturation magnetization for different type garnet according to different temperatures (Moulson, 2003)

Transitions involving with these states produces usual absorption and dispersion line shapes. YIG has very large figure of merit (rotation angle over the absorption)

near infrared, however in the visible band the absorption becomes very large compare to the increase in the Faraday rotation angle making the material hard to use in a desired application. Hence there are many efforts to increase the magneto-optic properties of YIG, e.g, for Bi-YIG material this increase was observed as a function of the Bi concentration. The most suitable ions expected to increase the magneto-optical properties are those of having a right radii, e.g., Bi, Pb, Ce, Pr, Nd, Ru, Rh, Ir and Co (Moulson, 2003).

Saturation magnetization is a very important phonemia for a magnetic material. Since the saturation magnetization is the amount of magnetic field that a magnet can produce, optimum values for that material must be optimized for service usage.

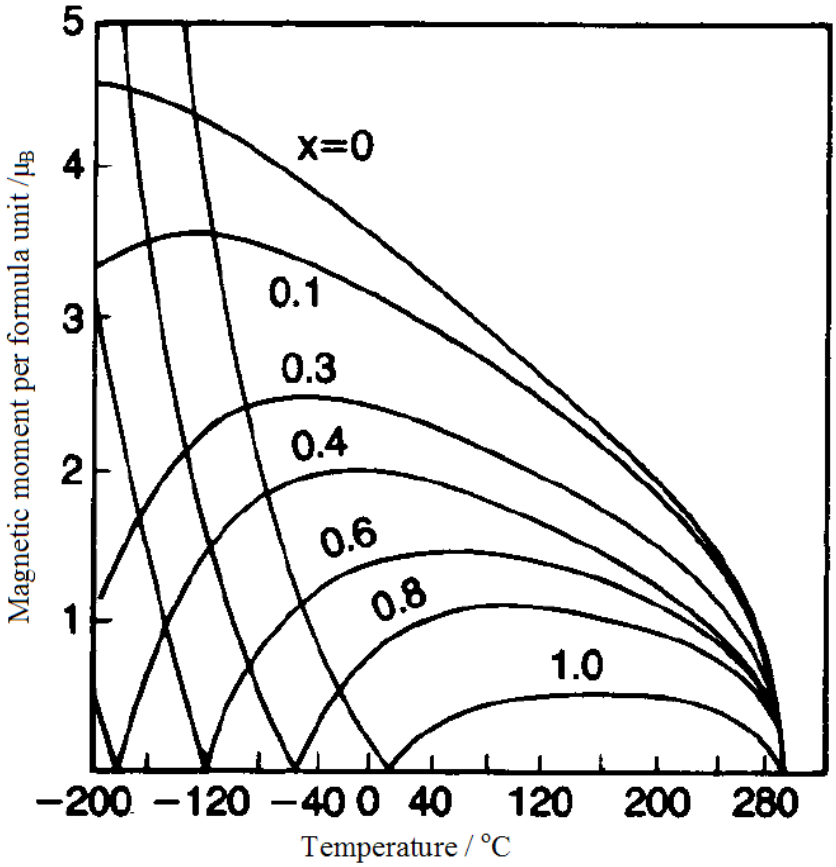

Figure 2.16 Saturation magnetization for different stoichiometry conditions of $Y_{3(1-x)}Gd_{3x}Fe_5O_{12}$ (Moulson, 2003)

2.6.3.2 Applications of garnet based materials

There are number of applications YIG and YIG based materials used widely. As mentioned above;

- *Faraday rotator* is an optical device that rotates the polarization of light due to the Faraday Effect, which in turn is based on a magneto-optic effect. The Faraday rotator works because one polarization of the input light is in ferromagnetic resonance with the material which causes its phase velocity to be higher than the other. The application is illustrated at Figure 2.17 (Popescu et al. 2005).
- *Magneto-optical imaging (MOI);* is a contact-free method of evaluating the local critical current densities in coated conductors. It does so by visualizing the pattern of trapped (or excluded) magnetic flux which gives information on any non-uniform current density associated with local defects. Thus bad spots can be readily identified and this information is particularly vital to improving the performance since it is the weakest sections along the length of a coated conductor that dictates its ultimate performance as shown in Figure 2.18 (Argonne National Laboratory, 2002).

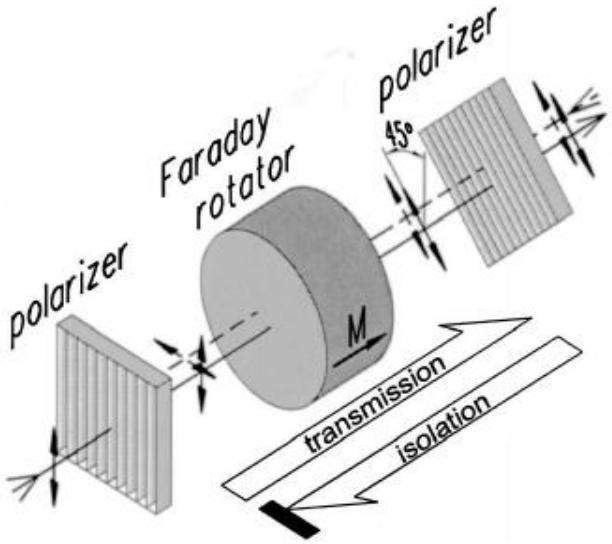

Figure 2.17 Faraday rotator (Popescu et al. 2005).

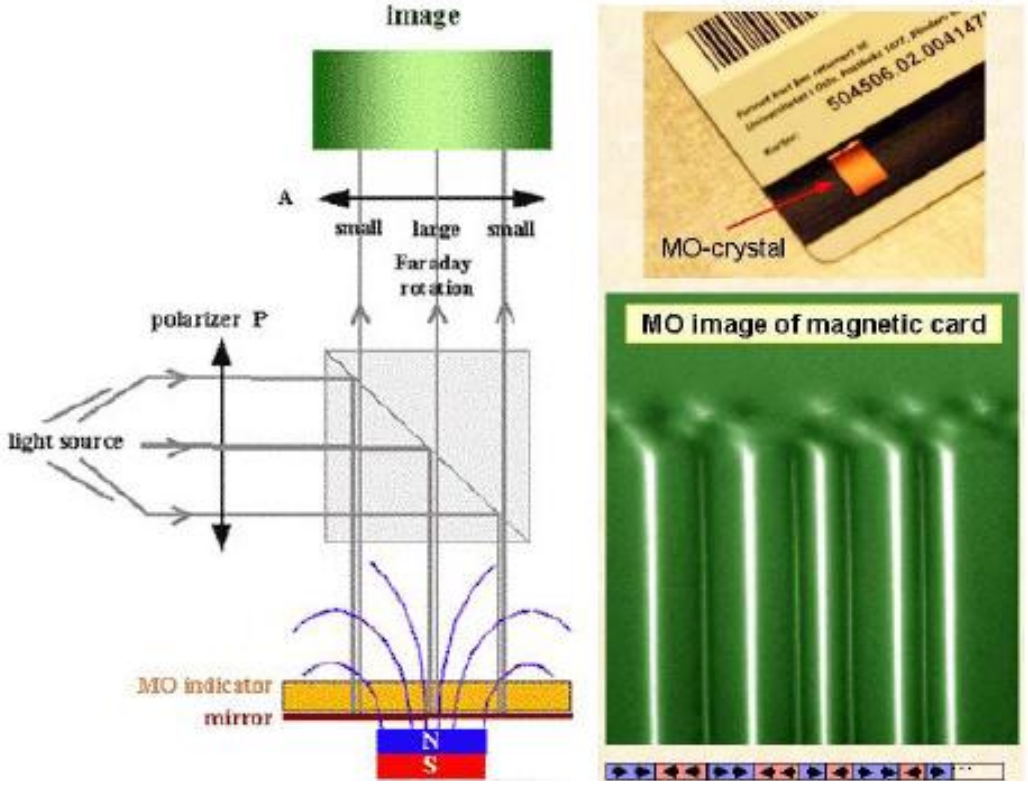

Figure 2.18 Illustration of MOI, an example of MO crystal and a MOI of a magnetic card (Argonne National Laboratory, 2002).

Researches about magneto optical materials keep going on the institutes by the scientist. According to some abstracts of researches which have not become a report, YIG based materials are started to be used as gas sensors. This is a very promising study since the signal is processed by light by the way time for gas sensing is hoped to be shorter than traditional gas sensors. In addition, in biochemistry and medical science YIG based nanopowders are employed to increase the sensitivity of MR devices at hospitals.

2.7 Magneto-optical Recording

Magneto-optic (MO) recording is the most highly develop erasable optical data storage technology. The advantages of MO recording are (a) remove-ability; (b) reliability, in terms of information preservation; and (c) high recording density. Nevertheless, drawbacks are (a) higher access time (about twice that of the magnetic

recording) (b) commercial products are not able to be direct overwriting and (c) relatively high cost of optical drives and optical media. In order to compete with the fast developing magnetic recording technology and other recording technology, such as semiconductor memory, MO recording not only need to keep its main advantages of high recording density and removeable from the drive, but also have to satisfy requirements of super-fast access time, high data transfer rates and low cost for the entire subsystem.

Further high density recording will be accomplished by using short wavelength lasers, mark edge recording methods, double track density recording, magnetically induced superresolution, zone constant angular velocity (in order to make the bit length equal) etc. techniques.

Though the complexity of applications of information technology in various fields has grown, the consumer is demanding to process ever larger volumes of data. Magneto Optic Disk (MOD) technology is found to be the strongest candidate for supplementing if not replacing magnetic media for secondary removable storage in view of its low/cost and large storage density as shown in Figure 2.19 and Table 2.7**.**

The technologies and applications of optical memories were studied in details. The present study addresses the advances which have taken place in the last two years specifically in magneto-optic disks (Das et al., 1994).

Since the magneto-optic (MO) media is erasable and has high recording density, it is a very serious candidate for use as a secondary removable storage device. It has additional advantages of reasonably high data transfer rate; high tolerance to fluctuating ambient temperature, stray magnetic field and dusty environment. Among the various optical recording technologies, it is most advanced and has large scale usage possibilities. Several US and Japanese companies are now making MO drives and disks and some of the standard products marketed by them are given in Table 2. As can be seen, the cost of the MO disk storage varies between US$ *0.27* to 0.50 per MB of storage compared to the cost of floppy disk storage which is US$ 1 to 2 per

MB. Storage costs of other competing media like Bernoulli magnetic cartridge (US$ 1 O/MB) are also higher than that of MO media. Therefore, MO disk storage at present offers the lowest cost of storage amongst all removable storage production, the cost is bound to come down. Fujitsu plans to see MO recorders at an affordable US$ 400 per piece within a few years (Das et al., 1994).

Due to its high access time and low data transfer rate, MO recording system cannot replace the magnetic hard disks for online direct-access-storage devices. However, where a large volume of data is to be handled and stored through removable medium or where data security is important, the MO media is the most appropriate medium today. With increasing use of faster computers having large semiconductor RAM size in industry offices and homes, stand-alone small computer systems have to handle large volumes of data and multimedia systems will be used for this purpose. Once that happens, floppy disks (as used presently) will not suffice to store this volume of data and transfer it to other computers. The MO recording system appears to be the obvious replacement for floppies in PCs and work stations. Potential application areas include strategic and military applications. It is interesting to correlate the development of the MO recording technology with development of PCs. By 2000 AD, a PC is expected to have 1 GB of semiconductor RAM memory with a processing speed of 100 MIPS. However, this will not make secondary memories obsolete. It is well known that for efficient operation of a PC, a secondary storage ten times the size of the RAM memory is required. A window of opportunity exists for the MO technology to offer an appropriate secondary memory of the size of 10 GB in a PC (Das et al., 1994).

The main competitor to the MO technology is still the magnetic recording technology specially for the erasable and removable high density recording system. The magnetic recording seems to be a cat with nine lives. Since 1970s its demise has been predicted again and again by the 'experts'-first due to the advent of magnetic bubbles and now due to the optical recording. But each time the technology has fought back with improvements and cost reductions which the new challengers could not match. Today, it rules supreme for the direct-access-storage device applications,

but is being challenged by optical disk technology in the removable media market. It is fighting .back through attempts like floptical disks and newer developments can be expected in future (Das et al., 1994). Application of MO technology listed in Table 2.8.

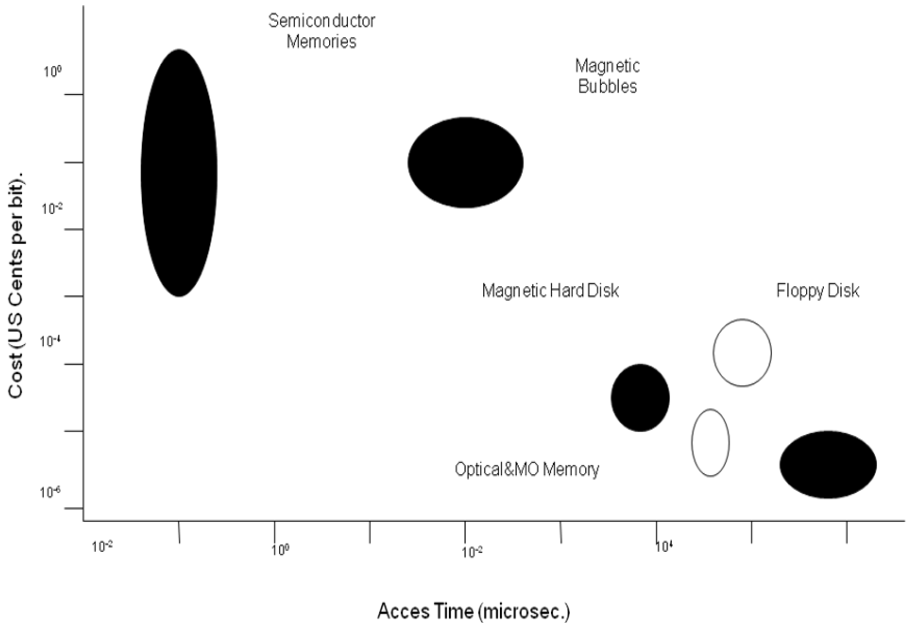

Figure 2.19 Chart showlng usage of different memories (Das et al., 1994).

Table 2.7 Comparison of various commercial recording technologies, (Das et al., 1994).

Technology	Areal Density MB/cm^2	Bits per cm	Tracks per cm	Data Transfer Rate KB/s	Access Time
Dijital Tape (1/2*)	0,02	2500	7	550	Minutes
Hard Drive (5 ½*)	8	12000	667	1373	20 ms
Floppy Disk (3 ½*)	0,32	6900	54	92	1 s
Video Tape (½*)	1,8	6900	260	120	Minutes
DAT-4mm	18	24000	748	183	20 s
CD-ROM (3 ½*)	70	11000	6000	1830	40 s
MO Disk (3 ½*)	40	10000	6000	4000	40 ms

Table 2.8 Applications of MO technology at different areas (Das et al., 1994).

Education	• Course Material for Distance • Learning Archival Storage • Paperless Library • Audio-visual Programmes
Health	• Hospital Record • Medical lmage Storage
Engineering	• CAD/CAM Stations • lmage Processing in Remote • Sensing
Service	• Bank Record Storage
Industry	• Railways Reservation Data Storage • **Airline** Reservation **Data** Storage • Office Data Record

CHAPTER THREE
SOL-GEL PROCESS THIN FILM DEPOSITION

3.1 The Chemistry of Precursors Solution

If inorganic sols and gels can be obtained by various methods, they are often directly synthesized from chemical reactants dissolved in a liquid medium. The chemical reactants which contain the cation M (metal) present in the final inorganic sol or gel is called the chemical precursor. Its chemical transformations are complex and involve a competition at the molecular level between the reaction responsible for the formation of open structures and the one leading to dense solid. Those same reactions are responsible for the controlled dispersion of dense colloidal particles in a sol or their agglomeration into a gel (Pierre, 1998).

All types of precursors can be used, provided they are miscible. For thin film production metal alkoxides are better than its salts as a precursor to achieve crack-free, pinhole-free, homogeneous and textured films.

Solvents which dissolve precursor have a molecular structure chracterized both by a permanent dipole moment μ and by a relative dielectric constant ε_r. A high relative dielectric constant (ε_r>40) is often due to the existance of a permanent dipole moment. Such molecules have good ionizing properties and can therefore dissolve other polar solute. On the other hand when the solvent's relative constant is low (ε_r <20), it has a weak ionizing property and can only dissolve less polar solute.

Sol-gel precursors undergo chemical reaction with solvents and the other species present in the solution. One of the most efficient models used to predict those reactions is the Partial Charge Model. Various atomic or molecular groups called ligands can bind to a complex C or cation M either directly or by substituting another ligand. The mechanism of the transformation depends on the partial charge of the different atoms in the species. Those with a negative partial charge are nucleophilic,

and those with a positive charge are electrophilic. Similarly, in a substitution reaction, the new ligands with the highest partial charge are the nucleophile while the group in the metal complex with the highest positive charge is the leaving group.

We can easily prepare solutions by addition of specific precursor, solvent and other chemicals for YIG, Ce-YIG and Bi-YIG thin film productions according to Table 3.1 in appropriate stoichiometries.

Table 3.1 Precursors, solvents and chelating agents for YIG based thin film production

Solutions	Precursor	Solvent	Chleating agent
1	Yttrium (III) 2,4 Pentanedionate	Methanol, 99% and Pentanedionate	Acetic acid, glacial 99,9% (Metal basis) and Propionic acid 99,9% (Metal basis)
2	Iron(III) 2,4 Pentanedionate		
3	Bi (III) Acetate		
4	Cerium (III) Pentanedionate		

3.2. Hydrolysis and Condensation Reaction

Hydrolysis can be expressed by deprotonation of a solvated M cation and it consists in the loss of a proton by one or more of the water molecules that surrounds the M in the first solvatation shell during hydrolysis process. As a consequence, the aquo ligand molecule, H_2O that is bonded to the metal is either transformed into an hydroxo ligand, OH^-, if only one proton leaves, or into an oxo ligand O^{-2}, if two protons detaches.

The behavior of the cations in aqueous solutions can yet be summarized according to their nature and with respect of their final type of ligands as shown in Figure 3.1. Figure 3.1 shows that Y, Ce and Bi has cations with valance III and Fe has cation with valance II and III. By the way these will have a slightly higher charge and electronegativity than those with valance I which does not hydrolyze in solution but remain as solvated cations of the form $[M(H_2O)_N]^{+Z}$. Therefore, Y, Ce, Bi and Fe extensively undergo condensation and precipitate in the form of hydroxides.

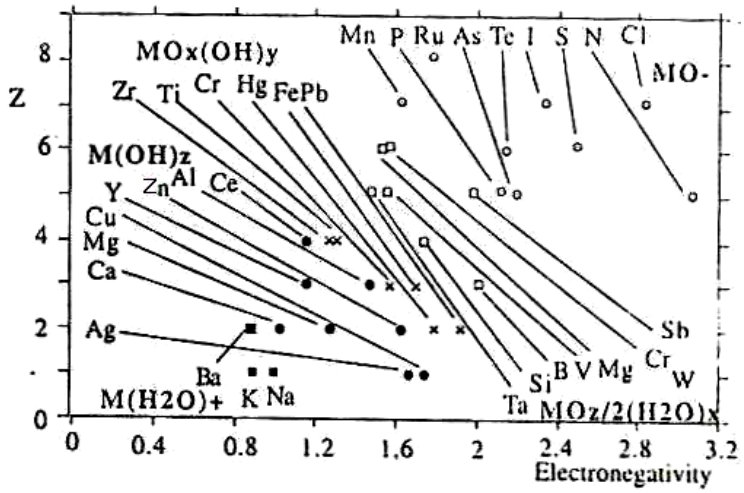

Figure 3.1 Charge versus electronegativity. This relation shows the species formed by cations in aqueous solutions (Pierre, 1998).

After hydrolysis, condensation reaction occurs to form a polynuclear complex consisting of two metal atoms. Condensation, in aqueous solutions, is the result of either an olation or an oxolation reaction. In either case, one must be quite careful as the oxygen present sometimes speeds the reaction to apoint where it becomes necessary to work in the the neutral atmosphere of argon in order to control it. In the first case, transfer of the H to an OR ligand according to the reaction below (olation process);

$$\text{-Y-OH- + -Y-OR- => Y-O-Y +ROH} \qquad (3.1)$$

In the second case, transfer of the H to an OH group according to reaction (3.1), condensation is called oxolation.

$$\text{-Y-OH + -Y-OH => Y-O-Y + ROR} \qquad (3.2)$$

As mentioned above in the Reactions of 3.1 and 3.2, the same reactions can be written for Bi, Ce, and Fe based precursors. Hydrolysis and condensation both keep on going thus gradually building up a tridimentional network that, at the end, often forms a solid phase which was constructed with electrostatic forces. This process is accelerated by heat as the rate of the both reactions increases together with the temperature. Since the kinetics of hydrolysis and condensation, and hence the overall

reaction and the type of polymers formed, depends on the pH, a great variety of materials with different structures can be obtained. These include linear polymers as well as dense colloidal particles and smaller ones with more or less weakly bonded cross-linked clusters of polymers.

3.3 Thermodynamics of Nucleation and Crystal Growth

The chemical reactions which transform a precursor solution, produce a large variety of complexes. The formation of solid particles can be described as a process of nucleation and growth, according to the sequence (3.3);

$$\text{hydrolysis} \rightarrow \text{condensation} \rightarrow \text{nucleation} \rightarrow \text{growth} \qquad (3.3)$$

Solid particles can form as the results of heterogenoues on foreign inclusions, such as dusts, or the products from uncontrolled hydrolysis (Pierre, 1998).

The transformation from the amorphous to the crystalline state can be considered with phenomenological thermodynamics. The most favorable site for the nucleation can be derived by classical nucleation theory. It should be noted that much of the volume is not far from the surface and the interface with the substrate and heterogeneous nucleation is more likely to occur in the thin films. Assuming for simplicity that regions of crystalline YIG is spherical with a radius r, a free energy change ΔG, due to homogeneous nucleation is given by

$$\Delta G = 4\pi r^2 \gamma + \frac{4}{3}\pi r^3 \Delta G_v \qquad (3.4)$$

where γ is the interfacial energy between the amorphous and the crystalline YIG and ΔG_v the free energy change per unit volume. In case of solid-solid transformation, a nucleus usually undergoes distortion in atomic arrangement as a result of contact with surrounding matrix and/or the substrates. Consequently, a distortion energy term must be added in a right-hand side of Equation 3.4. In the present case,

however, both the matrix and the substrate are amorphous giving incoherent interfaces, and the nucleus is not affected by them in terms of the atomic arrangement. Therefore, the distortion energy can be regarded as zero (Fujihara et al., 2001).

From the nucleation $\partial(\Delta G)/\partial_r=0$, a free energy barrier, ΔG_c, which subcritical embryos must overcome to become supercritical nuclei, is derived as follows:

$$\Delta G_c = \frac{16\pi\gamma}{3(\Delta G_v)^2} \tag{3.5}$$

At the substrate surface, "amorphous YIG" has a higher interfacial energy than crystalline YIG. When the nucleus forms on substrate, some high-energy substrate/amorphous, YIG surfaces are replaced by lower-energy substrate/nucleus surface. This contributes to a smaller overall interfacial energy in Equation 3.5, resulting in reduction of the free energy barrier. Thus, the heterogeneous nucleation at the substrate surface is more likely to occur. Consideration of a polyhedron nucleus leads to a similar tendency.

When the nucleus is formed on a flat substrate characterized by contact angle, θ, the reduced barrier, ΔG^*_c, can be expressed by:

$$\Delta G_c^* = f(\theta)\Delta G_c \tag{3.6}$$

where

$$f(\theta)=¼(2+\cos\theta)(1-\cos\theta)^2 \tag{3.7}$$

The θ value is determined by the surface energy of the substrate (γ_s) and the nucleus (γ_n) and the interfacial energy between them (γ_{sn}) :

$$\cos\theta = \frac{\gamma_s - \gamma_{sn}}{\gamma_{sn}} \tag{3.8}$$

Figure 3.2 shows a relationship between f(θ) and θ. The f(θ) value increasing the contact angle θ. Therefore ΔG_c^* in Equation 3.6 is lower with smaller contact angle of the nucleus. $\gamma_{s=}\gamma_n$ and $\gamma_s=0$ in homoepitaxial systems give cosθ=1, f(θ)=0, and accordingly $\Delta G_c^*=0$. On the other extreme, $\gamma_{sn}=\gamma_s+\gamma_n$ gives $\Delta G_c^*=\Delta G_c$, where the homogeneous nucleation occurs without the effect of the substrate.

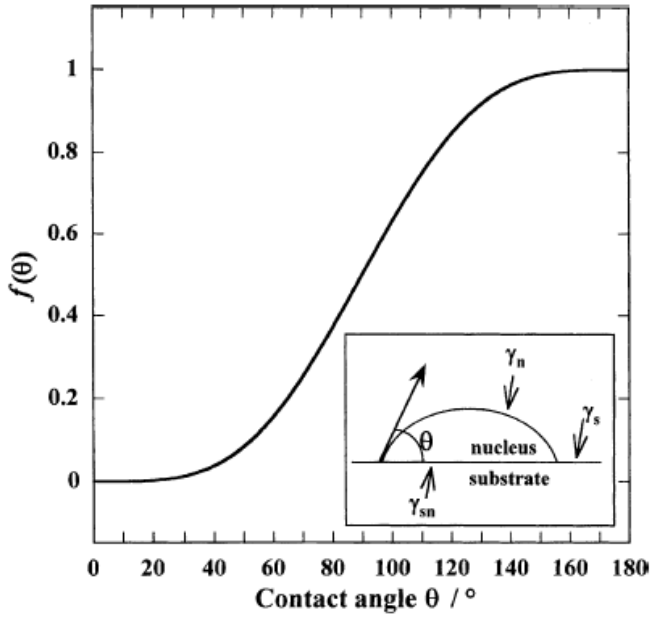

Figure 3.2 A relationship between f(θ) and contact angle, θ (Fujihara et al., 2001)

γ_{sn} is generally less than the sum of γ_s and γ_n. When γ_s is constant as for the glass substrates, γ_n is determined by γ_n as follows:

$$\gamma_{sn} = \alpha\gamma_n \quad (0 < \alpha < 1) \tag{3.9}$$

From Equations 3.9 and 3.10,

$$\cos\theta = \left(\frac{\gamma_s}{\gamma_n}\right) - \alpha \qquad (3.10)$$

Assuming that α is constant, the lowest γ_n gives the largest cosθ and hence, the smallest ΔG_c^*.

A typical value of γ_s is 0.26 J/m^2 for the surface of the silica glass composed of silicon and oxygen atoms without any dangling bonds. The surface energy of Pyrex borosilicate glass might be slightly higher depending on the distribution of Si-O-Si, Si-OH, B-O-B,, etc., and surface domains due to phase seperation.

Finally, we can presume reason for the random orientation often observed in the sol-gel-derived YIG thin films. The rate of the heterogeneous nucleation typically reaches a maximum at a lower temperature. At higher temperatures, the homogeneous nucleation competes with the heterogeneous one. This limits the annealing of the films to lower temperatures. On the other hand, the driving force for the crystalization is higher at lower temperatures because of a larger difference between the melting point and the nucleation temperature. For example, YIG crystallizes from a sollution of yttrium (III) 2,4 pentanedonate, iron (III) pentanedionate and methanol around 65^{o}C in the presence of OH^-. Unless the Y^{+3} , Fe^{+3} ions are coordinated by the thermally stable organic molecules according to the stoichiometric rates calculated before preparing solutions, the nucleation of YIG cannot be controlled by temperature. Even at optimal temperatures, the heterogeneous nucleation can take place in the bulk of the film as well as the film/substrate interface because of defects such as pores, decomposed organic residues or precipitates (Choi et al., 2000). Also one can consider that if the more substrate crystal structures same to the goal crystal structure the lower crystallization temperature obtained. For example if GGG substrates were used instead of Si(100) or glass slides the temperatures can be decreased.

3.4 Gelation

Gelation is a process according to which a sol or solution, transforms to a gel. It consists of establishing links between the sol particles or the solution molecules so as to form 3-dimensional solid network. Gelation occurs when the extent of polymerization reactions ξ reaches a critical value ξ_c. This precise critical stage, when for the first time a polymer of infinite size is formed by comparison with the molecular scale, defines the gel point. In a practical manner, at this point the product resulting from polymeric condensations transforms suddenly from a viscous liquid to a material with elastic properties.

Gelation can be described in a more abstract fashion within the frame work of critical phenomena in thermodynamics in particular by the percolation theories. The most simple of the percolation models is isotropic such as the bond percolation and the site percolation (Figure 3.3). In these models, either a bond is established or a site is occupied with probability p, in a completely random fashion througout a geometrical network.

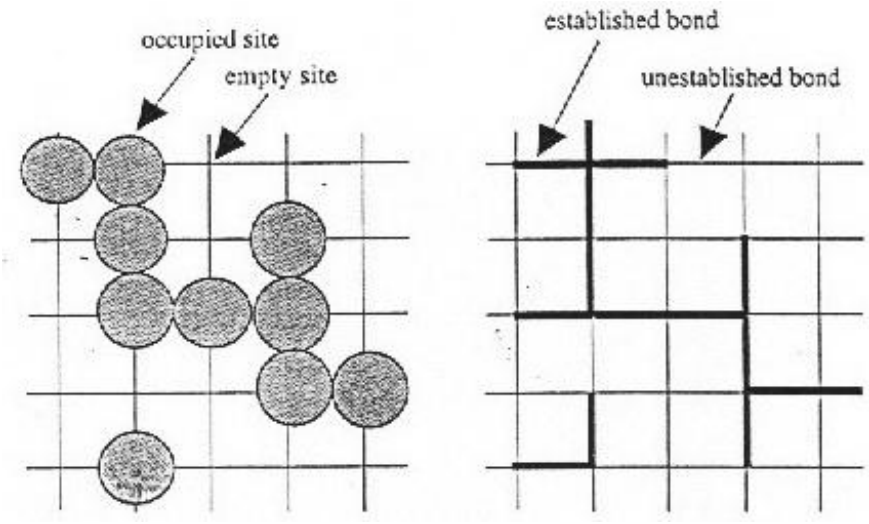

Figure 3.3. (a) Site percolation and (b) bond percolation on a square bi-dimensional network (Pierre, 1998).

Another critical parameter is the percolation treshold probability p_c as shown in Figure 3.4. However, its value depends on the coordination number Z in the case of a regular site network or on the volume fraction ϕ occupied by the sites if they are replaced by hard spheres packed in a random fashion. Critical probability p_c .is related to the coordination number Z by

$$P_c = \xi_c = \frac{1}{Z-1} \qquad (3.11)$$

Its main default is to neglect the formation of closed loops contrary to what occurs in real gelation.

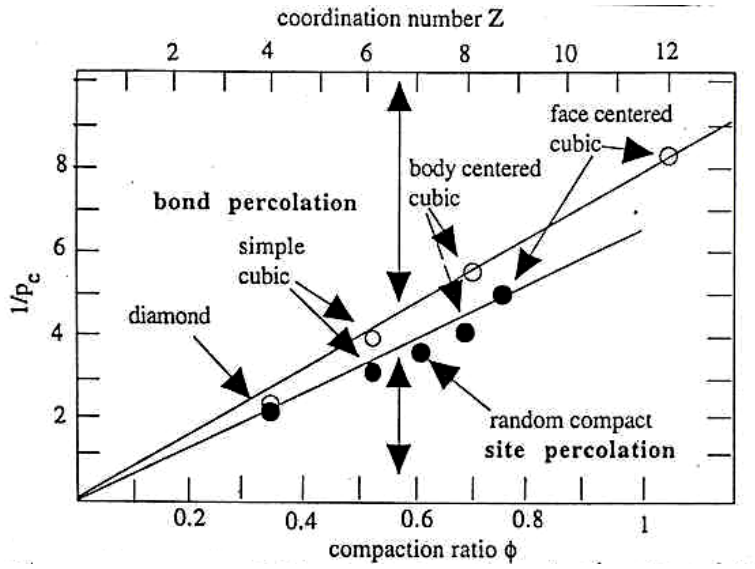

Figure 3.4 Empritical correlation between the percolation treshold and the lattice (Pierre, 1998).

Diffusion limited aggregation models (DLA model) can be also described the happening. The sites at a given distance from the original nucleus are allowed to walk randomly. They may therefore either avoid meeting a nucleus or reach one of them and participate to its growth. As soon as some branches of the aggregate statistically start to grow around this nucleus, the posibility for sites to diffuse up the corridors without hitting a tendency to keep growing so that the aggregates becomes even more ranified than in the percolation models (Figure 3.5).

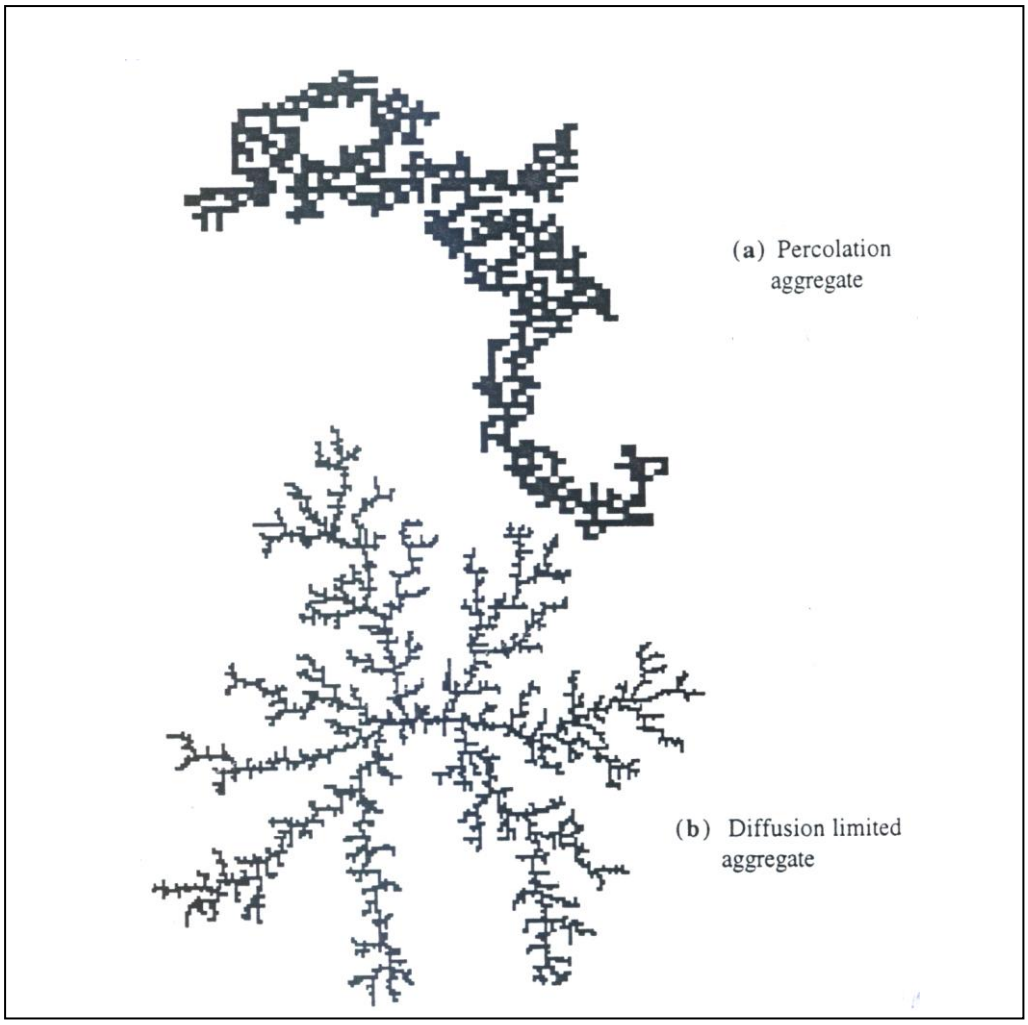

Figure 3.5 Bi-dimensional aggregates on a square lattice with different fractal dimensions: (a) aggregate near the percolation tresholds in site percolation and (b) diffusion-limited appregation cluster comprising 3600 particles (Pierre, 1998) .

Ramified structures can be observed when a large number of primary particles have aggregated. Nevertheless, a linear bonding between colloidal particles is possible in some conditions as soon as the first contacts occur and this phenomenon can be described within the DLVO theory. Figure 3.6 demonstrates condition for the formation of a stable sol, gelation and coagulation as a function of the non-potential determining electrolyte C. If the concentration C of non-potential determining electrolyte is smaller than the existance of a critical concentration for gelation C_g a sol is stable. If $C_c > C > C_g$ where C_c is the existance of a critical electrolyte concentration the sol slowly gels (Pierre, 1998).

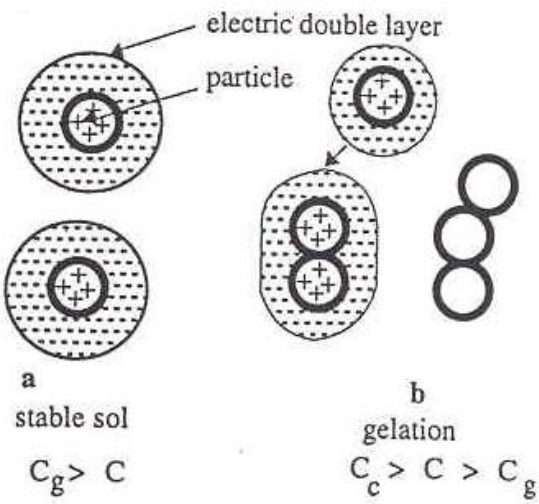

Figure 3.6 Conditions for the formation of: (a) stable sol; (b) gelation as a function of the non-potential determining electrolyte (Pierre, 1998).

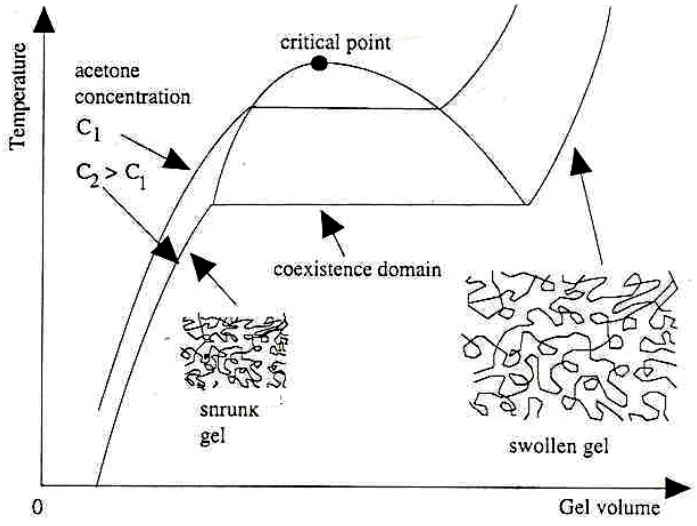

Figure 3.7 State diagram of an organic polymer gel (Pierre, 1998).

The molecular groups which constitute the solid network of a gel can present a more or less strong affinity for molecules in the liquid which impregnates them. This affinity can be strong enough, in some cases, to overcome the mechanical strength of the network without destroying it. That is to say, the gel swells or shrinks and in some gels such as organic polymeric gels, this change in gel volume is reversible. A polymeric gel can practically adapt one of two possible states: a shrunken state and a

swollen state. These two states can coexist, exactly as a liquid and a gas state can coexist in a classical liquid-gas phase transformation. Moreover, a critical point exists above which the gel passes gradually from one state to the other. Below the critical point is possible to obtain either one of these two states; or the coexistence of both, as in classical liquid-gas state transition. The critical point corresponds to critical conditions where the compressibility of the gel network becomes infinite; this is a true critical point in a thermodynamic sense. Overall, the state transition of a covalent polymeric gel network can be described within the theory of critical phenomena, and a state diagram can be drawn as shown in Figure 3.7.

3.5 Drying

Drying rate per unit area of gels follows two succesive regimes: a "constant-rate" period, followed by a "falling-rate" period (Figure 3.8, curves a and b). The transition between these two regimes occurs at a very sharp point named the "critical-point".

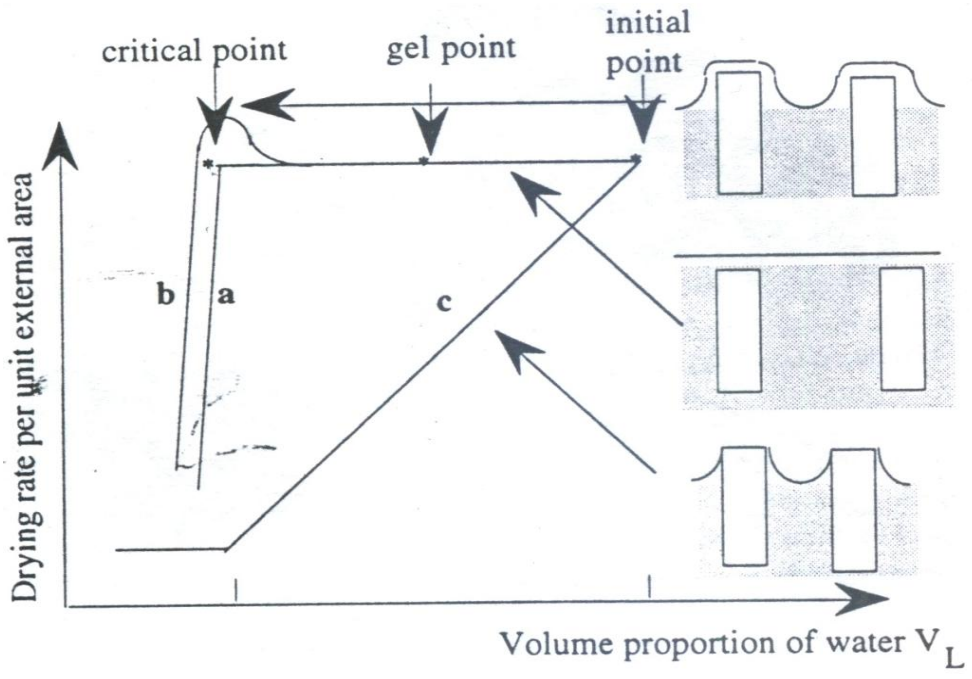

Figure 3.8 Evolution of the drying-rate per external unit area of wet gel as a function of the liquid volume proportion V_L: (a) and (b) experimental graphs; (c) graph if the drying rate was proportional to the relative surface of menisci (Pierre, 1998).

Drying is irreversible transformation of the gel which is composed of a solid network and liquid matrix. The capillary mechasim explain well the reproducible adsorption hysteresis curves of water in silica gels. This mechanism can be summarized as follows:

1) Evaporation creates a liquid vapor meniscus at the exit of pores in the gel.
2) This induces a hydrostatic tension in the liquid, which is balanced by an axial compression on the solid.
3) The latter compression makes the gel shrink.
4) As a result of shrinkage, more liquid is fed to the menisci at the exit of the gel pores, where it is evaporated and so on (Pierre, 1998).

Branch IC in Figure 3.9.a corresponds to the initial drying of the gel. At point C, the meniscus is as in Figure 3.9.b. Further on, it penetrates inside the gel pores which stop shrinking. Along CD, the meniscus is deeper inside the pores (Figure 3.9.c), but this is a spherical meniscus with two radii of curvature equal to the radius of the pore r_{por}. Its curvature is therefore $2/r_{por}$. From D to S, only a thin layer of water remains on the cylindrical walls of the pores. The cylindrical configuration of point S maintains if water is reabsorbed in the gel and curve SDF is followed during re-adsorption. At point F, the gel pores again full of water. Along FC, during the second desorption cycle, a spherical meniscus is formed again.

The equilibrium meniscus radius r_m at any instant, is given by the compressive stress that the solid network of the gel can support. The contact wetting angle at the liquid–solid-vapor interface is undetermined along a sharp solid edge. Higher stresses are required for higher compression states of the solid, which requires higher hydrostatic tension in the liquid. It follows therefore that the menisci are sharpar and sharper (smaller radius r_m) when contraction increases. This keeps a gel shrinking until the meniscus radius r_m reaches the pores radius r_{por}. The latter event defines the drying critical-point. Beyond this critical-point, capillarity cannot increase the

compresive stresses anymore on the solid network. For instance, for a cylindrical pore of radius r_{por} and cross section:

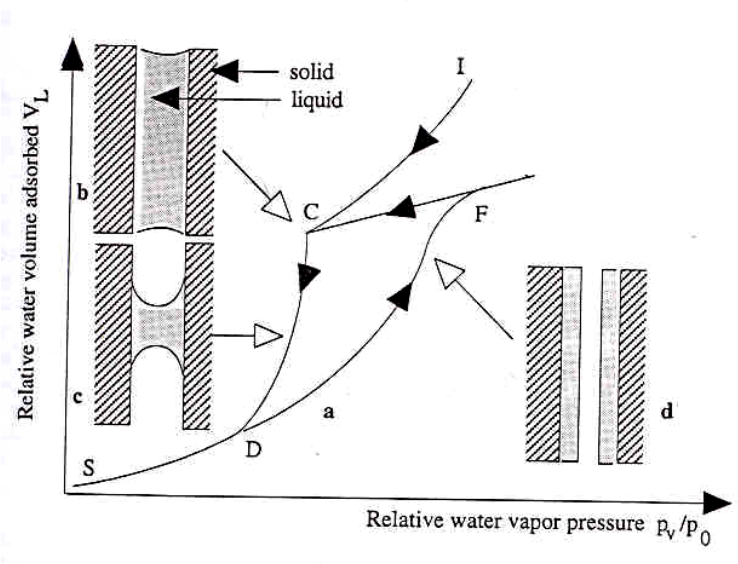

Figure 3.9 Adsorption-desorption isotherms of water vapor in a silica gel (Pierre, 1998).

Hence the drying rate per unit area should decrease linearly with the liquid content c. The experimantal existence of a "constant-rate" period before the critical-point is therefore generally interpreted as being due to evaporation of a continous liquid film, which covers the entire surface of the gel. Obviously, the existence of such a film can be related to the affinity of oxides for water, which depends largely on the nature of the oxide.

3.6 Sintering

The specific surface area of the porosity is an evolution named sintering. In terms of termodynamics, sintering orginates from the specific surface area S_a a porous material, which introduce a positive contribution G_s due to the surface of pores, to the Gibbs free energy of a material:

$$G_s = \gamma S_a \tag{3.12}$$

Since states with a lower Gibbs free energy are more stable at a given temperature and pressure, the specific surface area should tend to decrease, an evoluation which can proceed according to two types of pore evaluation:

1) by changing the shape of pores but not their volume.
2) by eliminating the pores.

The first type of evoluation does not produce any material densification, contrary to the second one which makes a material shrink without losing any mass. Moreover, sintering is not the only transformation which involves Gibbs free energy of surface origin. Grain boundaries constitute another type of surfaces which contribute another Gibbs free energy term G_{gb}. In order to reduce this free energy contribution, the specific grain boundary area S_{gb} must decrease. Hence another evolution named grain growth, enters in competition with sintering.

Sol-gel ceramics just after drying and even after heat treatments at intermediate tempratures often have a very high specific surface area and an extremly small grain size. Hence, both sintering and grain growth tend to be vigorous.

In so far as densification can be considered to occur in sol-gel ceramics by global atomic diffusion, the corresponding diffusing species are also likely to enhance the cyristallization by nucleation and growth of the most thermodynamically stable crystalline phase. Densification on sol gel ceramics often occurs concurrently with their crystallization. Even in compounds where sintering occur at a relatively low temperature, the crystallization of a stable phase usually occurs at a slightly lower but very close temperature (Liu et al., 2002).

3.6.1 Possible Texture Evolution

If the external pressure in the pores outside the solid is p_o and the two principal curvature radii of the surface are r_1 and r_2, the local pressure inside the solid, just under the surface is

$$p = p_o + \gamma\left(\frac{1}{r_1} + \frac{1}{r_2}\right) \tag{3.13}$$

When the local surface is convex, that is to say when the solid is on the same side as the center of curvature, a radius r must be taken with a positive value. On the other hand, when the local surface is concave, that is to say when the solid is on the opposite side to the center of curvature, the radius r must be taken with a negative sign. For sake of simplicity, it is possible to consider the case where p_o=0 (treatment under vacuum). In such conditions, when two spherical particles of radius r are linked by a neck with principal radii x (convex radius) and p (concave radius) at the neck tip and such that in absolute value p<<x, (Figure 3.10), the mechanical stresses states inside the solid near the external surface are:

- a compression far from the neck, at point A where:

$$p_A = \sigma_c = \frac{2\gamma}{r} > 0 \tag{3.14}$$

- a tension near the neck at point N where:

$$p_N = \sigma_t = \gamma\left(\frac{1}{x} - \frac{1}{\rho}\right) \approx \gamma\frac{1}{\rho} < 0 \tag{3.15}$$

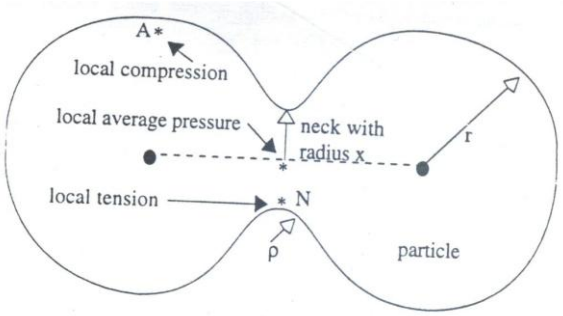

Figure 3.10 Initial sintering stage of two spherical particles (Pierre, 1998).

The mechanical stress difference between points A and N is equivalent to a difference in the local Gibbs free energy of mechanical nature and it tends to attenuate by transfer of matter. Finally, the surface energy happens to be at the origin of atomic transport.

The transport of atoms to sinter a material can proceed along several different types of paths. Some of these paths actually result in densification, in particular when the atoms originate from sources, that is to say local parts of the material located along dislocations and grain boundaries, or when atoms are transported by a cooperative phenomenon known as viscous flow. Other transport paths only change the pore shape, in particular when the matter comes from the pore surface.

3.6.2 Atomic Transport Mechanisms Operating During Sintering

When sintering proceeds by atomic diffusion in the case of a ceramic which comprises several types of ions, each ion has to diffuse in proportion to its stoichiometry in the ceramic. Consequently, sintering is controlled by the slowest ion transported along its fastest path. If one species, for instance the anions, has the smallest diffusion coefficient, it is possible to accelerate its diffusion with the help of cations additives which have a lower valence and a size close to that of the host cation. To balance the electric charges in the compound, anion vacancies are then often created, which accelerates anions diffusion. In oxide, this concerns the oxygen

anions which diffuse significantly at high temperature only. The formation of oxygen vacancies increases their mobility and can help sintering. The proportion of additives must remain below but can be close to the solid solution limit.

3.6.2.1 Atomic Diffusion in Sol-Gel Materials

It is possible to question whether transport mechanisms such as atomic diffusion can be extrapolated from the conventional ceramics, to the collodial sizes. Atomic transport by diffusion in the vapor phase rests on an evaporation-condensation process due to differences in the equilibrium vapor pressure near a solid surface, depending on the local surface curvature. The equilibrium vapor pressure is lower near a neck between two particles where the solid surface is essentially concave, than far from a neck, at atomic scales. The resulting vapor pressure gradient induces a vapor phase diffusion which keeps feeding the neck. It modifies the pore shape but does not induce densification which in a gel often occurs between 900 and 1200 ^{o}C. At these temperatures, the equilibrium vapor pressure of oxygen is very low for an oxide. On the other hand, the residual hydration water usually absent in conventional ceramics is much more volatile relatively low temperatures. Hence, this mechanism cannot be completely rejected for the sol-gel processes, as water is known to be a general sintering aid. Surface atomic diffusion does not induce densification neither. However, it is like to operate at a lower temperature than usual, because of the extremely high special area of sol-gel and also because of the special nature of the gel surface which easily adsorbs water molecules or OH groups.

Overall, the atomic transport mechanisms which make the pore shape become spherical without producing any densification are likely to be common in sol-gel materials. If this is the case, these mechanisms can be strongly modified by tailoring the nature of a sol-gel solid surface, for instance by adsorbing hydrophobic molecules. Hence the liquid sol-gel chemistry can have a marked influence on the sintering behavior.

As seen previously, lattice atomic diffusion can actually densify a material, depending on the source from where the atoms originate. In a crystalline material such as an oxide, this mechanism begins to significantly operate when the atomic mobility of oxygen atoms is high enough that is to say at high temperatures. It requires the presence of atomic point defects such as vacancies, interstitialcies, or dislocations. However gels are far from being very well crystallized; they have at best very small grains whit a high defects density. Consequently, depending on the compound, lattice diffusion can often operate at a much lower temperature than conventional ceramics. Actually, a distinction between the different atomic diffusion paths, such as on a surface, inside a lattice, along dislocations or along grain boundaries may be dificult in sol-gel materials, in so far as it becomes difficult distinguish between dislocations, grain boundaries and surfaces. It would seem appropriate to consider a global diffusion process through a very disordered gel or transition phase structure.

3.6.2.2 Sintering and Crystallization in Sol-Gel Ceramics

In so far as densification can be considered to occur in sol-gel ceramics by global atomic diffusion, the corresponding diffusing species are also likely to enhance the crystallization by nucleation and growth of the most thermodynamically stable crystalline phase. Densification of sol-gel ceramics often occur concurrently with their crystallization. Even in compounds where sintering occurs at a relatively low temperature, the crystallization of a stable phase usually occurs at a slightly lower but very close temperature.

Production of garnet powders and thin films via sol-gel method provides easy densification. While several techniques were used in literature keeps densification or sintering temperatures as high as 1050 ^{o}C. (Tas et al., 1996). The same phase structures were obtained at temperatures like 700-900 ^{o}C when sol-gel or wet chemical routes were used (Rehspringer et al., 2000). Since sol-gel is an atomic scale production method the temperatures and time for transformations become easy to operate.

CHAPTER FOUR
EXPERIMENTAL STUDIES

4.1 Purpose

The objective of this study was to fabricate pure YIG and substituted YIG structures such as Ce-YIG and Bi-YIG using sol-gel technique for different wavelength magneto-optical applications. With this aim, solutions to produce YIG, Ce-YIG and Bi-YIG thin films including Y, Fe, Ce and Bi based precursors, solvent and chelating agent were prepared. In order to determine solution characteristics which affect thin film structure; turbidity, pH values and rheological properties of the prepared solutions were measured by turbidimeter, pH meter and rheometer machines before coating process. Prior to coating process, substrates which were used such as silica glass, Si(100) were cleaned in 1:1 methanol-water medium with ultrasonic cleaner. In order to use suitable process regime and to define chemical structure and reaction type of intermediate temperature products, DTA-TG and FTIR analyses were performed in the film production using xerogels produced at different temperatures. Structural analysis of the films was performed using multipurpose XRD and surface morphology was investigated using SEM/EDS. Thickness measurements of the films were investigated using refractometer and spectrophotometer. In addition, the magnetic properties and magneto-optical properties of the films were characterized through VSM and self designed MO-equipment respectively.

4.2 Materials

In order to prepare magneto-optical thin films Si(100), glass and GGG substrates were used as substrates. Chemicals which were used for production of solutions, gels and thin films were listed in Table 4.1. The chemical which were used as precursor materials are all alkoxide materials. By this way appropriate solvents and chealating

agent were used to dissolve precursors easily. Generally speaking there were no wetting problems, thus any wetting agent was not used.

Table 4.1 All chemicals used for production of magneto-optical YIG films.

Chemical Type	**Chemical**	**Formula**	**Purity**
Precursor	Yttrium(III) 2,4-pentanedionate hydrate,	$C_{15}H_{21}O_6Y•xH_2O$	99.9 % (REO)
	Iron(III) 2,4 Pentanedionate	$C_{15}H_{21}FeO_6$	99.9 % (REO)
	Cerium(III) 2,4-pentanedionate hydrate	$C_{15}H_{21}CeO_6•xH_2O$	99.9 % (REO)
	Bismuth(III) acetate, (metals basis)	$Bi(OOCCH_3)_3$	99.999 %
	Ytterbium (III) 2,4 Pentanedionate Reaction,	$C_{15}H_{21}O_6Y_b$	99,9 %(REO)
	Silicon (IV)Acetate	$Si(OOCCH_3)_4$	99.999 %
Solvent	Methyl alcohol	CH_3OH	99.90 %
	Pentadionate	$C_5H_7O_2$-	99.90 %
Chelating Agent	Acetic acid, glacial 99,9% (Metal basis)	$C_2H_4O_2$	99.90 %
	Propionic Acid	CH_3CH_2COOH	99.90

4.3 Preprocessing

4.3.1 Substrate Preparation

In the current research, Si(100), fused silica, glass and gadolinium gallium garnet (GGG) were used as substrate materials. All the substrates used were in high purity. The properties of the substrates were illustrated in Table 4.2.

Table 4.2 Properties of substrates

Substrate	**Surface**	**Crystal structure**	**Preperation for coating process**
Si	Polished	Cubic –Textured	Cutting with diamond pen
Fused Silica	Polished	Amorph	Cutting with diamond pen
Glass	Polished	Amorph	Ready for coating process
GGG	Polished	Distorted perovskite	Ready for coating process

4.3.2 Solution Preparation

In order to obtain crack, pinhole free and continues thin films in the exact stoichiometries, homogenous solutions must be prepared. In this research there are three main solutions, these are YIG, Ce-YIG and Bi-YIG based solutions. According to the differences on the solutions, different solution stoichiometries were prepared. Solution preparation steps for each solution was summarized and generalized in Figure 4.1.

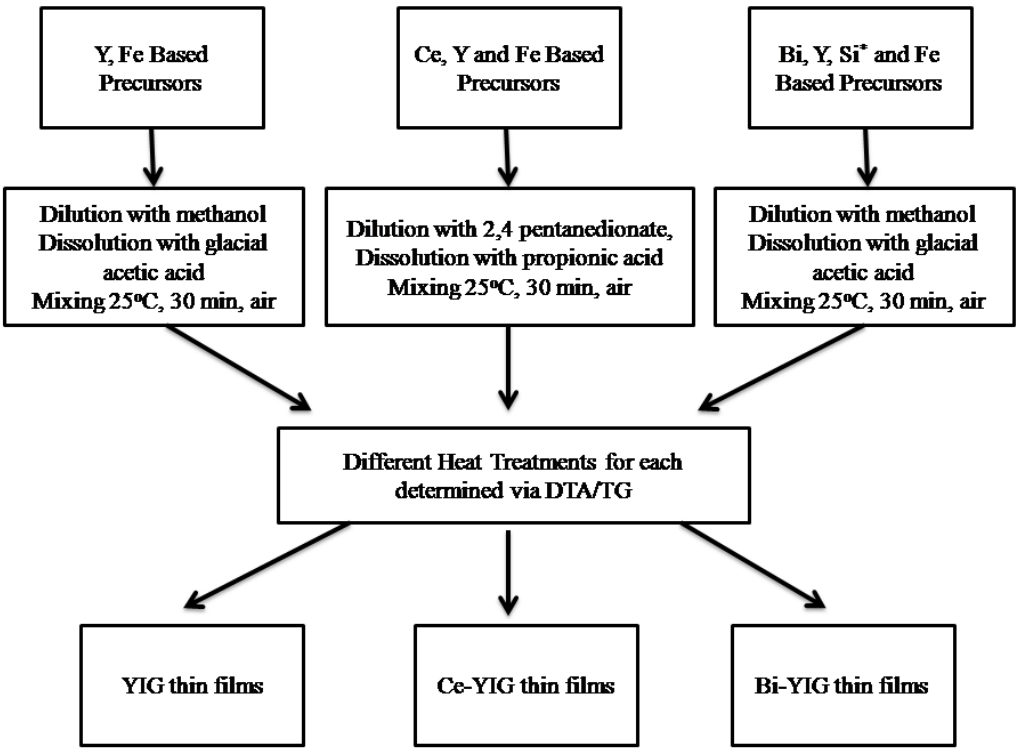

Figure 4.1 The diagram of flow chart for sol-gel process

4.4 Preparation of Thin Films

There are several methods for sol-gel based coating of materials. Most used ones are spin coating, dip coating and solution dropping. Spin coating and solution dropping methods were used in this study.

Spin coating is a procedure used to apply uniform thin films to flat substrates. In short, an excess amount of a solution is placed on the substrate, which is then rotated at high speed in order to spread the fluid by centrifugal force. A machine used for spin coating is called a spin coater, or simply spinner. Rotation is continued while the fluid spins off the edges of the substrate, until the desired thickness of the film is achieved. The applied solvent is usually volatile, and simultaneously evaporates. Therefore, the higher the angular speed of spinning, the thinner the film. The thickness of the film also depends on the concentration of the solution and the solvent.

Solution dropping method is simpler and hand operated if compared with spin coating. This procedure has several steps, these are; taking solution in to an injector, dropping solution drops at equal numbers on substrates, giving a tilt of approximately 20° to the substrates with the help of a clean pincer to help whole wetting on substrate surface.

The films of YIG based solutions were deposited on substrates with Cookson Electronics Equipment SCS G3P-8 model spin coater. The coating spinning regime which were used is presented in Figure 4.2. As shown in figure spin coating process which is executed at air atmosphere has three steps. At first 20 seconds the spinner accelerates up to 3600 rpm to spread the solution and remove the excess of solution. Between 20^{th} sec. to 50^{th} sec., spinner turns in a constant speed at 3600 rpm. At this step of operation the deposited solution spreads related to the parameters of wettability, viscosity, pressure etc... Third step is the deceleration step here vaporizing of the volatiles and residual solutions were removed in 25 seconds.

Ce-YIG and Bi-YIG based solutions were coated using solution dropping procedure. The smoothness of the films was determined by eye in this method. By this way the quality of the surfaces are not as good as spin coated ones.

After coating process several heat treatment procedures must be applied to the films in order to obtain thin ceramic films. The films were annealed at different

temperatures and different regimes according to the data obtained from DTA/TG results. The DTA/TG data and heat treatment regimes will be presented at next section in experimental results.

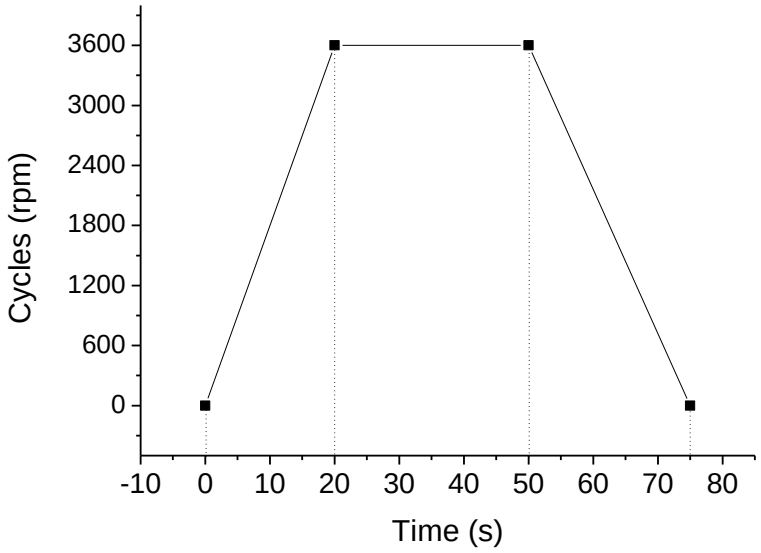

Figure 4.2 Spin coating regime for YIG based solutions.

4.5 Characterization

4.5.1 Solution Characterization

In order to determine solution characteristics which affect thin film structure, turbidity, pH values and rheological properties of the prepared solutions were respectively measured by turbidimeter, pH meter, and rheometer machines before coating process.

4.5.1.1 Turbidity Measurement

Turbidity which means the relative cloudiness of a liquid, gives the optical characteristics of suspended particles in a liquid. Light is passed through the sample and is scattered in all directions. The light that is scattered at 90^{o} angle to the incident light is then detected by a photo diode and is converted into a signal linearized by analyzer and displayed as ntu. The more suspended particles there are in a liquid, the

more light will be scattered, resulting in a higher ntu value (Wilde & Gibs, n.d.). Turbidity properties of YIG, Ce-YIG and Bi-YIG based solutions were measured to use standard solutions for coating process by VELP TB1 Model turbidimeter. The sample was placed in a vessel with a dimension of Ø25 mm and height of 50 mm. Formazin is recognized throughout the world as a primary standard. Formazine solution was used to calibrate the turbidity. Measurement range was taken in the range of 0 and 1000 ntu (nephelometric turbidity unit).

4.5.1.2 pH Measurement

After preparation of transparent solutions, pH values of the solutions were measured to determine their acidic and basis characteristics using a standard pH meter with Mettler Tolede electrode.

4.5.1.3 Rheological Measurement

The rheological measurements were conducted using a Bohlin Instruments CVO 100 Rheometer with 2^o conic plate geometry 60 mm in diameter and 0.7 μm gap sizes between plates. The viscosity values of YIG, Ce-YIG and Bi-YIG based solutions were performed at constant 300 Hertz frequency and 25^{o}C at single shear mode. The viscosity characteristics were compared for each solution.

4.5.2 Material Characterization

4.5.2.1 Differantial Thermal Analysis-Thermogravimetry (*DTA-TG)*

In order to use suitable process regime and to define reaction type of intermediate temperature products, DTA/TG analyses were performed under O_2 flowing for the YIG, Ce-YIG and Bi-YIG based xerogels by using Shimadzu DTG-60H Model DTA-TGA. In addition, a detailed information regarding as decomposition, weight loss and phase formation was obtained by means of the same machine. Prior to the measurements, buffer solutions were firstly dried at room temperature and

subsequently fired to in the gel structure at 200^{o}C for 30 minutes in air. Measurements were carried out from room temperature to 900 °C at heating rate of 10^{o}C/min for buffer samples and to 750^{o}C at a heating rate of 10^{o}C/min for YIG, Ce-YIG and Bi-YIG based samples. Measurements were performed in a cylindrical Al_2O_3 crucible diameter of 4 mm and depth of 2 mm.

4.5.2.2 Fourier Transform Infrared Spectroscopy (FTIR)

FTIR spectrum of YIG, Ce-YIG and Bi-YIG based samples were recorded by using Perkin Elmer Spectrum BX model FTIR to determine the organic components in the samples. FTIR absorption spectra were measured over the range of 4000 to 400 cm^{-1} at room temperature after the reactions in the temperature range of 300 ^{o}C and 800 ^{o}C for 30 minutes in air. After preparing coatings on Si(100) substrates reflectance - wavelength and % absorbance-wavelength curves can be obtained. According to the results, depending on temperature, variation of organic components concentration can be determined by Fluka library supplied by Perkin-Elmer.

4.5.2.3 X-Ray Diffractions (XRD)

X-ray diffraction (XRD) patterns of thin films were determined by means of multipurpose Rigaku D/Max-2200/PC Model difractometer with a Cu K_α radiation by using multipurpose thin film attachment. Measurements were performed by applying 40 kV voltages and 36 mA current.

4.5.2.4 Scanning Electron Microscopy (SEM)/Energy Dispersive Spectroscopy (EDS)

The surface morphologies of both buffer layers and YBCO layers were examined by a Scanning Electron Microscope (JEOL-JSM 6060 SEM) with an Energy Dispersive X-ray spectroscopy (IXRF System EDS) system attachment. Accelerating voltage of 20 kV was used for the SEM imaging and SEM/EDX analyses. Weight percentage distributions and X-ray mapping of elements were determined by EDS.

4.5.2.5 Thickness Measurement

Refractive indexes of thin films were measured at selected wavelenghts in the VIS region by a high-accuracy Abbe refractometer at room temperature. Refractive indexes were used to determine film thickness values of single layered buffers using V-530 JASCO UV/VIS Spectrophotometer.

4.5.2.6 Vibrating Sample Magnetometer (VSM)

Magnetic properties of the YIG, Ce-YIG and Bi-YIG thin films were determined by using VSM Lakeshore 736, 7400 Series at different magnetic fields. Saturation magnetization (M_s), remnant magnetization (M_r) and coercivity ($H_{c)}$ were determined.

4.5.2.7 Magnetooptic Measurements

Magneto-optical properties of doped YIG thin films could be described in detail by alteration of components of dielectric tensor with magnetic field. Produced thin films were saturated by effect of a external magnetic field. We have used a light source that has several wavelengths. Light is polarized by a polarizer. Polarized light is transmitted to surface of thin film perpendicularly. Polarization of light is changed by Faraday or Kerr effect. Magneto-optical measurement set up is showed in Figure 4.3. and 4.4 for Faraday and Kerr Effects respectively. Elements of designed setup were described below in details;

Light Source; He-Ne laser which are wavelength 632,8 nm and intensity 0,5 mW is used.

Polarizer; Brand of polarizer is Glan-Thompson. Polarizer has several advantages like, high extinction ratio ($1:10^5$), wide wavelength (350-2300 nm) and operation sustainability in the case of angular income of light.

Analyzer and Step Motor; Glen-Thompson polarizer is used for analyzing. Rotating platform that has $1^{o}/800$ rotation angle is used. Rotation platform is controlled by a step motor and computer.

Optical Cutter; In order to modulation of light optical cutter that has 1000 Hz rotation frequency is used.

Modulator and Compensator; Cylindrical glass that is produced from MR3-2 type MO material and coil that is wrapped around the cylinder are used as light modulator and compensator. MO glass rotate polarization of light in order to obtain linearity of light with magnetic field. Compensator is improved sensitivity of system.

Electromagnet and Power Supply; Voltage and current of electromagnet are 20V and 50A respectively. Power supply of electromagnet is computer controlled. However, in the case of measuring of Faraday rotation, intensity of light and external magnetic field must be in the same direction. Thus, cores that are in the polars of electromagnets was removed and coils were used only. By this means, magnetic field source which could change with current linearly and has a 800 Gauss magnetic field value was produced. This value is sufficient to saturate garnet type MO materials.

Detector; The Si photo-detector in the system has several technical properties such as; wavelength between 300-1070, light intensity between 1pW-10mW, maximum 90 dB efficiency, 10-MHz frequency.

Lock-In Amplifier (LIA); LIA is used for measurement of modulated light.

Computer Interface; **GPIB** (IEEE488) card is used for computer controlling of devices. MATLAB and Lab VIEW are computer programs which were employed while performing the measurements.

Polarized light source was used in set-up. Polarizer that is located in front of light source is used for adjusting of polarization of light relative to reflection plane. First modulator has a photodedector that is used for measuring to intensity of light. Polarized light which passes through modulator reflects from the sample. Thus, elliptically polarized light is obtained. Elliptically polarized light is turned into fluctuating signal by PEM. PEM is used to modulate of polarization of light. Frequency of sinusoidal wave is proportional to Kerr angle and ellipsoid. Kerr angle and ellipsoid is measured by processing of signal that is corrected by LIA.

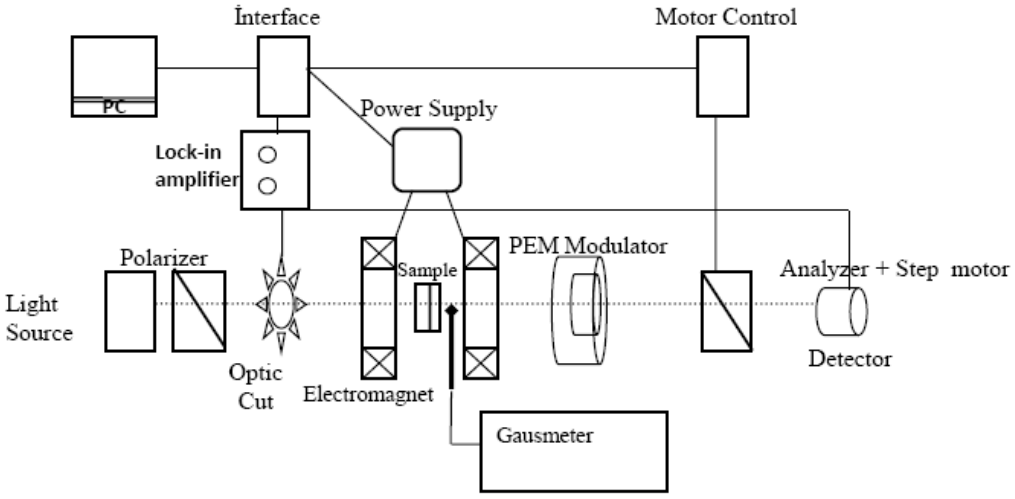

Figure 4.3 Magneto-optical Faraday Effect measurement experimental setup

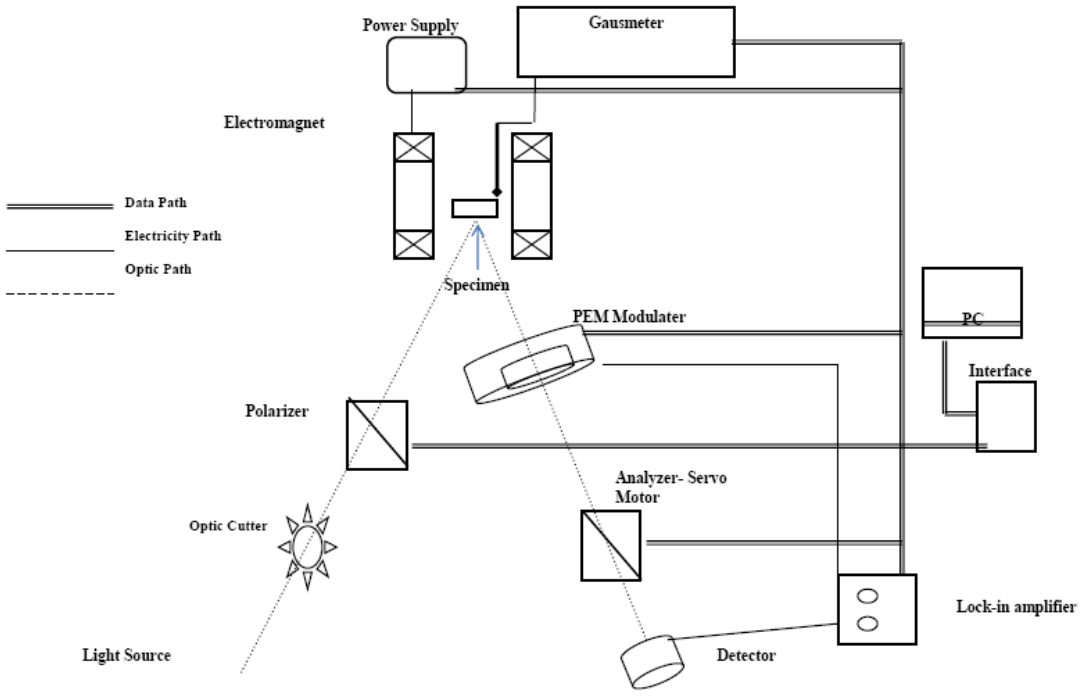

Figure 4.4 Magneto-optical Kerr Effect measurement experimental setup

CHAPTER FIVE
RESULTS AND DISCUSSION

Nanostructuring of materials through chemistry is an expanding area of research due to its scientific and technological potential in many fields where nanoscale control of structure is required to obtain either new functionalities or advanced physical properties while maintaining relatively low processing costs and large-scale processability (Obradors et al., 2006). The advances made during the past decade in the preparation and characterization of thin films and surfaces have brought an intriguing question within reach: is it possible to fabricate `designer solids' by controlling materials on the atomic scale, that is layer by layer, row by row, and ultimately atom by atom? Engineered molecules are common-place in electronic devices, and the same idea can be brought to bear on solids and electronic materials. Electronic properties of devices have been controlled by heterostructures, quantum wells and superlattices. Magnetism as a cooperative phenomenon lends itself to manipulation in small structures, where neighbor atoms can be replaced systematically by species with stronger or weaker magnetism. In fact, a class of magnetic/non-magnetic multilayers termed `spin valves' has been introduced into magnetic storage devices (Himpsel et al.1998).

By this way nano or micro structures which work for the same idea can be produced for electronic, magnetic and magnetooptical applications. According to the statements mentioned above magnetooptically active thin films were deposited on several substrates such as; Si(100), commercial Pyrex glass, fused silica and GGG via sol-gel method. The results of this research can be categorized into two parts; (a) solution properties such as turbidity, pH meter, and rheology, and (b) material and film characteristics including DTA-TG, FTIR, XRD, SEM-EDS, thickness measurement, VSM and magneto optical tester. YIG, Bi-YIG and Ce-YIG based solutions and films were compared and discussed a combination of characterizations in this chapter in details.

5.1 Solution Properties

In determination of solution characteristics; turbidity, pH values and rheological properties of the prepared solutions were measured by turbidimeter, pH meter and rheometer respectively prior to coating process. The solutions were prepared according to the stoichiometries mentioned in chapters beforehand.

5.1.1 Turbidity

As mentioned before, turbidity means the relative cloudiness of a liquid. It gives the optical characteristic of suspended particles in a liquid (Wilde & Gibs, n.d.). Whether solutions are dissolved very well is understood as ntu values with turbidity experiments before coating process. Measurement range is between 0 ntu and 1000 ntu. It is interpreted that powder based precursors are completely dissolved as turbidity value approaches to 0 ntu and they are not dissolved and some powder particles are suspended in a solution as it approaches to 1000 ntu. The fabrication of homogeneous, continuous and thin film is directly related to turbidity value which is 0 ntu.

Turbidity values of YIG, Bi-YIG and Ce-YIG based solutions were listed in Table 5.1. Studies performed in literature have similar results. Due to the fact that iron has red color, the turbidity values increase even if they are dissolved very well (Erol et al., 2009). Since YIG based solutions containing Fe ions possess with dark red color, the turbidity values of the solutions were obtained higher.

Tablo 5.1 Turbidity values of buffer and YIG based solutions.

Solution	**Turbidity (ntu)***
YIG	329
Ce:YIG	686
Bi:YIG	380

Depending on to the results listed in Table 5.1, YIG based solution has the smallest turbidity value. This means that the added substituent increase the turbidity

value in a logical way. Also Ce-YIG based solution has the highest value. Bismuth (III) acetate, (metals basis) Cerium (III) 2,4-pentanedionate hydrate increasing the number of external ions in the solution if compared with YIG based solution. The solubility of the Cerium (III) 2,4-pentanedionate hydrate component is low in pentadionate and propionic acid. By this way it can be pointed out that some of the Cerium (III) 2, 4-pentanedionate hydrate cannot be dissolved.

5.1.2 Acidic/basic characteristics

The pH value is a measure of the activity of hydrogen ions (H^+) in a solution therefore, its acidity. Solutions with pH values lower than 7 exhibit acidic properties, while pH values higher than 7 are considered as basic. A pH value is an important parameter in the solution deposition processes because it directly affects the hydrolyses, condensation and complexation reactions. Determination of solution characteristics is a key factor in sol-gel processing or solution based deposition. Inasmuch as pH value of the solution is an important factor influencing the formation of the polymeric three-dimensional structure of the gel during the gelation process, it should be taken into consideration while preparing solutions. While ramified structure is randomly formed in acidic conditions, separated clusters are formed from the solutions showing basic characters (Pierre, 1998). In addition the final film structure is directly related to the gelation processes. By this way pH value is an important parameter to be determined.

Tablo 5.2 The pH values of the prepared YIG based solutions.

Solution	**pH**
YIG	3,7
Ce:YIG	3,24
Bi:YIG	3,31

The pH values of YIG, Bi-YIG and Ce-YIG based solutions are illustrated in Table 5.2. As seen on this table; it can be understood that all three solutions are acidic. Ce and Bi substituted solutions are more acidic than the un-substitued one. Based on this; the addition of Ce and Bi decrease the pH value since the H^+ content

of these precursors are high. The pH values of the solutions have little differences. By this way it can be thought that mechanisms related to reactions of hydrolysis and condensation will be similar. Thus film growths of the films were found to be in the same characteristics.

5.1.3 Rheological Properties

Gelation occurs when aggregation of particles or molecules takes place in a liquid, under the action of Van der Waals forces or via the formation of covalent or noncovalent bonds. The process can be investigated using rheological measurement techniques (Phonthammachai et al., 2004). Times versus viscosity values of the solutions were determined as seen in Figure 5.1.

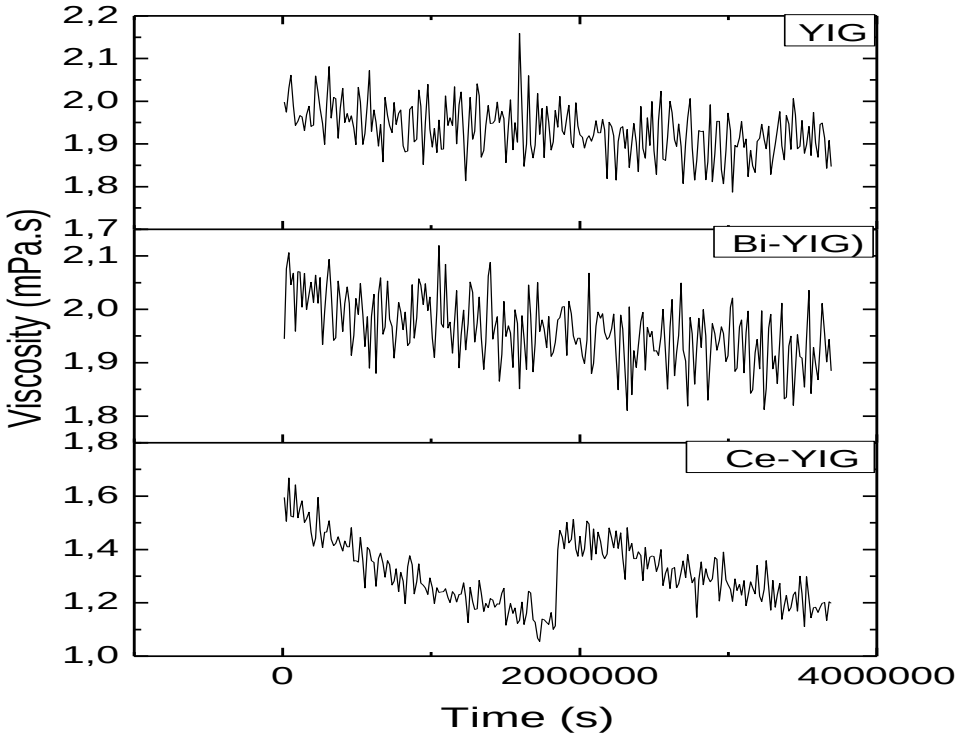

Figure 5.1 Time versus viscosity curves of the solutions (a) YIG based, (b) Bi-YIG and (c) Ce-YIG

As mentioned in our previous study (Öztürk et al, 2008), the decrease in the viscosity value with time can be explained by several reasons. With the excess of shear forces of the parallel plates on viscosity device the 3-D polymeric bonds are

broken and new complex structures are formed. Depending on Figure 5.1, it can be understood that, substitution of Ce and Bi into YIG decreases the formation of polymeric bonds. The viscosity value of the YIG based solution is more stable than that of the substituted ones. The average viscosity values of YIG, Bi-YIG and Ce-YIG solutions were found to be 1,93 mPa.s, 1,99 mPa.s, and 1,32 mPa.s respectively. Since the stoichiometric rate of the Bi precursor is more than that of the Ce precursor, the viscosity value is determined to be higher.

5.2 Material Characterization

5.2.1 DTA/TG Analyses

Differential thermal analysis was conducted to understand thermal decomposition of YIG, Bi-YIG and Ce-YIG solutions and xerogels during heat treatment process. Figures 5.2, 5.3 and 5.4 show the DTA-TG curves of YIG, Bi-YIG and Ce-YIG based xerogels which were dried at 300^{o}C for 30 minutes in air, respectively. According to the graphs, there are three main reactions occurred from room temperature to the oxide ceramic formation as reported elsewhere (Öztürk et al., 2008).

According to the DTA/TG curves exothermic and endothermic reactions occur in a temperature range between 30 ^{o}C and 1000 ^{o}C. It was determined that there are four different phenomena including removal of solvent-based materials, combustion of carbon-based content, formation of oxides and garnet phase formation (Erol et al., 2009). Temperatures where mentioned phenomena occur were determined and listed in Table 5.3. The DTA/TG curves were depicted in Figures 5.2, 5.3 and 5.4 for YIG, Bi-YIG and Ce-YIG based xerogels respectively.

Table 5.3 Reaction temperatures determined from DTA/TG

Rection → **Xerogel ↓**	**Solvent Removal**	**Combustion of Organics**	**Formation of Oxides**	**Phase Transformation and Topotectic Reactions**
YIG	~ 110^{o}C	~ 250 ^{o}C	~ 410 ^{o}C	~ 800 ^{o}C, ~1100 ^{o}C
Bi-YIG	~ 120 ^{o}C	~ 280 ^{o}C	~ 400 ^{o}C	~ 800 ^{o}C
Ce-YIG	~ 180 ^{o}C	~ 300 ^{o}C	~ 435 ^{o}C	~ 850 ^{o}C, ~850 ^{o}C

Table 5.3 shows thermal properties of YIG- based xerogel. In this table some critical temperatures such as, solvent removal, combustion of organics, oxidation and phase transformations are significant issues for determination of heat treatment regimes.

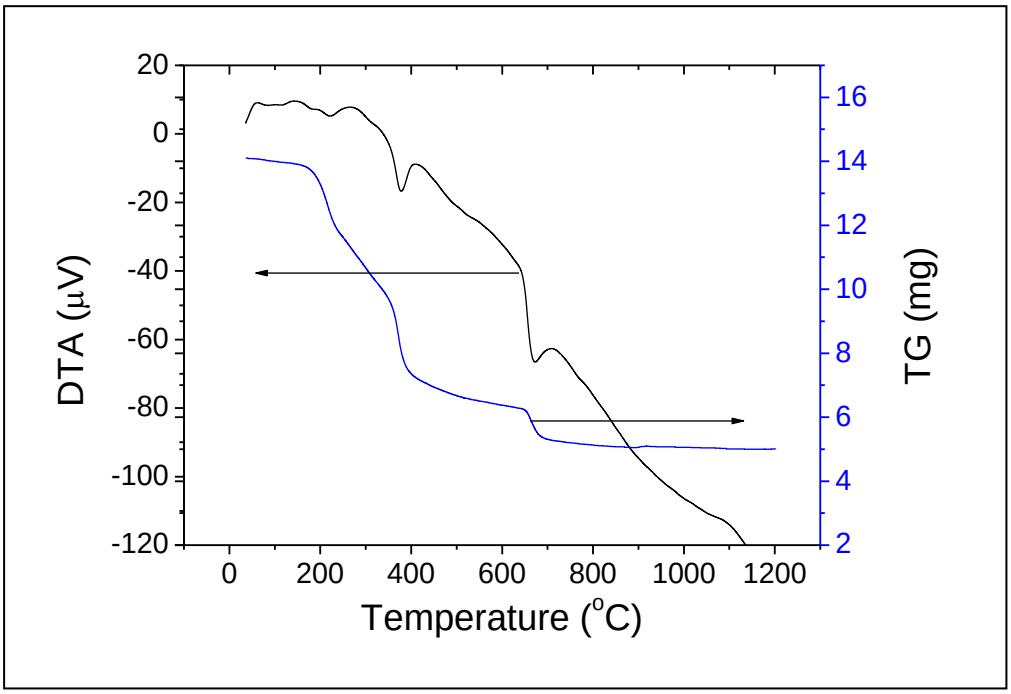

Figure 5.2 DTA/TG curve of YIG xerogel

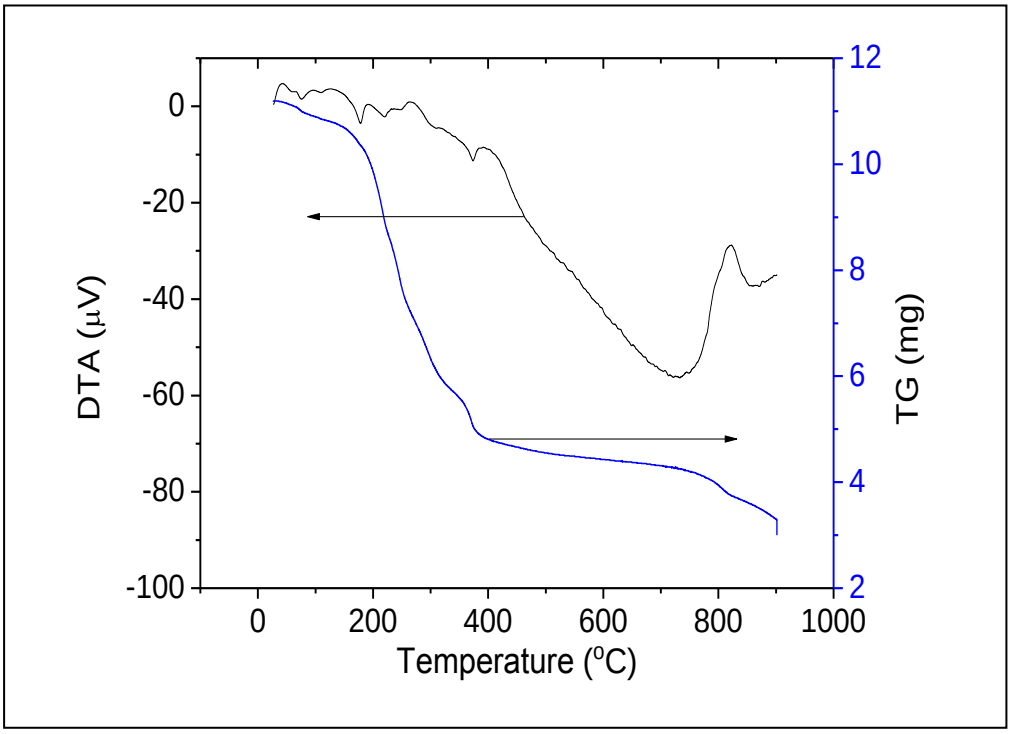

Figure 5.3 DTA/TG curve for Bi-YIG xerogel

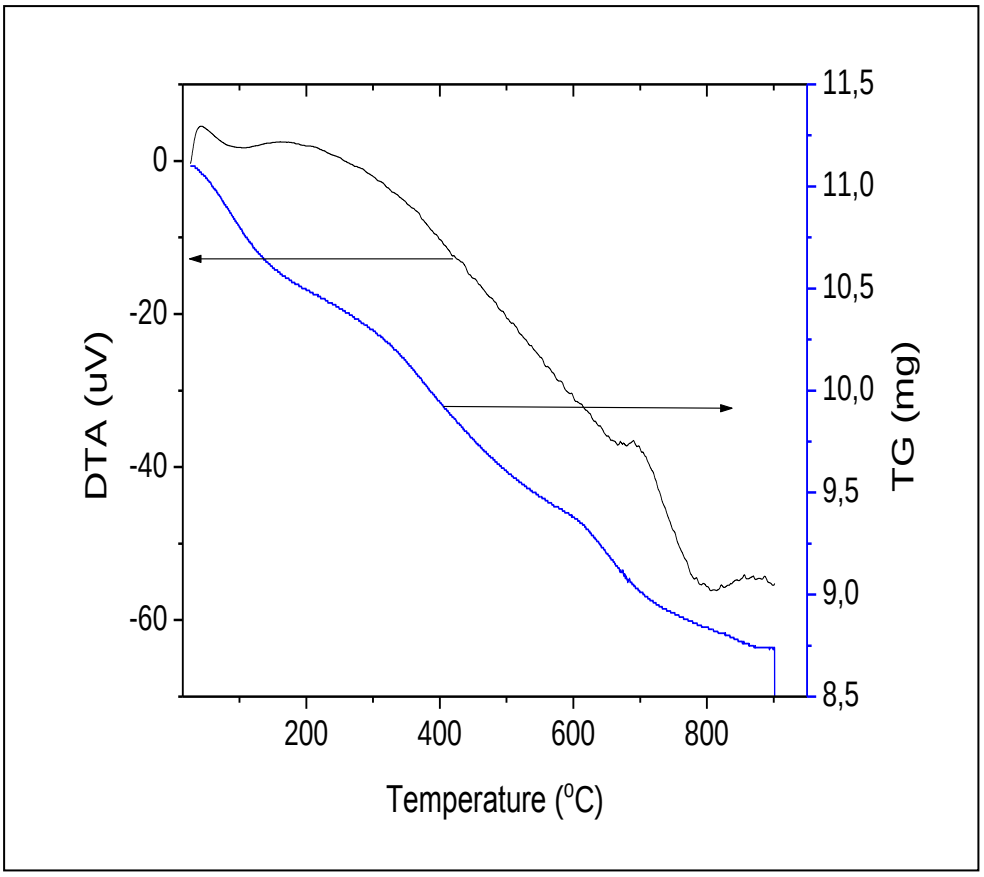

Figure 5.4 DTA/TG curve for Ce-YIG xerogel

As explained above, there are several temperatures which are critical for formation of garnet phase and heat treatment regime. Thus these critical temperatures were determined from the curves for each xerogel and illustrated in Table 5.4.

Table 5.4 Regimes determined via DTA/TG curves.

Critical Temperature → Xerogel ↓	**Drying**	**Combustion of Organics**	**Formation of Oxides**	**Phase Transformation**
YIG	100°C/10 min	350°C/15 min	450°C/30 min	1000°C/2 hr
Bi-YIG	100°C/10 min	350°C/15 min	450°C/30 min	750°C/2 hr 850°C/2 hr
Ce-YIG	100°C/10 min	350°C/15 min	500°C/30 min	850°C/2 hr 950°C/2 hr 1050°C/2hr 1150°C/2 hr

As seen from Table 5.3, the regime determined for Bi-YIG xerogel is not similar with the DTA/TG curve (Figure 5.3). The sublimation rate of Bi ions is very high,

thus the formation of the exact stoichiometry cannot be observed. Studies in literature show that annealing process of Bi-YIG films at 800 ^{o}C causes to obtain Fe_2O_3, $FeYO_3$ and Bi-YIG together. It was reported that they increased annealing temperature above 800 ^{o}C and also Bi-YIG fraction was increased in the specimen. Similar results can be seen in references of (Xu et al., 2008, Erol et al., 2009). Beside it is reported that YIG phase is not obtained at temperatures below 800 ^{o}C. Increasing temperature accelarates the reaction of Fe_2O_3 with $FeYO_3$ to form YIG as shown in Equation 5.1 (Zhang et al., 2008).

$$3FeYO_3 + Fe_2O_3 \rightarrow Y_3Fe_5O_{12} \ (T>800\ ^{o}C) \qquad (5.1)$$

By using DTA/TG weigh loss versus time with increasing temperature is determined too. TG analysis of the xerogels are important since this experiment gives information about the final film weight. With this information one can decide or get opinion about the film density, morphology. By using DTA/TG weigh loss versus time with increasing temperature is determined too. The change in weights for YIG, Bi-YIG and Ce-YIG based xerogels were listed in Table 5.5.

Table 5.5 Weight losses of the xerogels determined via DTA/TG curves.

Xerogel	**Weight Loss (%)**
YIG	64
Bi-YIG	73
Ce-YIG	32

Acoording to Table 5.4, weight loss of the Ce-YIG xerogel is denser than that of the others. Thus it has the minimum weight loss. With this respect weight losses of Bi-YIG and YIG xerogels are higher than that of Ce-YIG xerogel. It can be thought that the nature of Ce-YIG xerogel caused this low weight loss.

5.2.2 FTIR Analyses

FTIR spectra are commonly used to identify specific substances like organic groups. The spectrum reflects the characteristic vibrations of certain bonds between

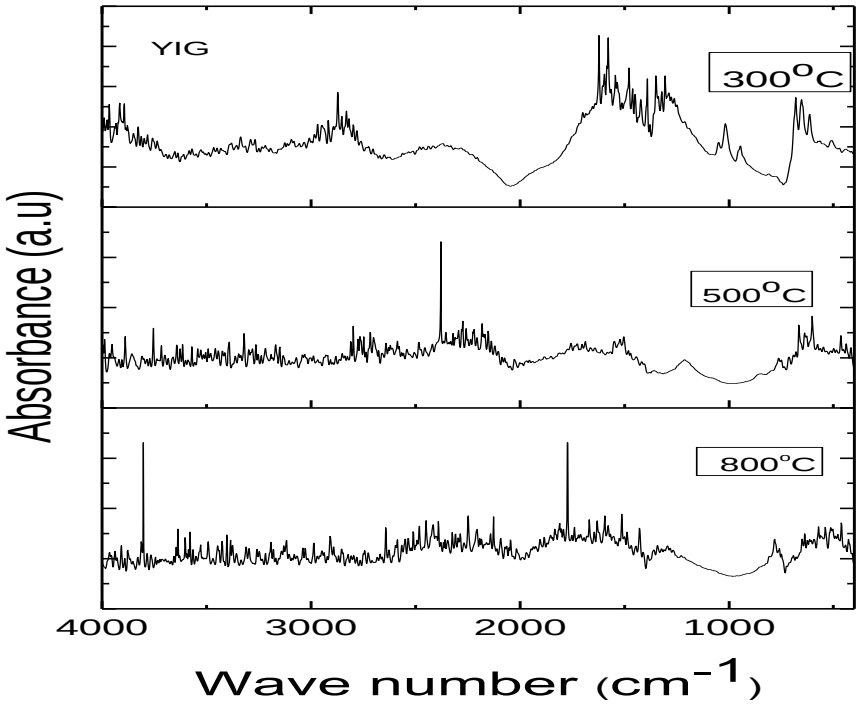

Figure 5.5 FTIR spectra of YIG based films at different temperatures

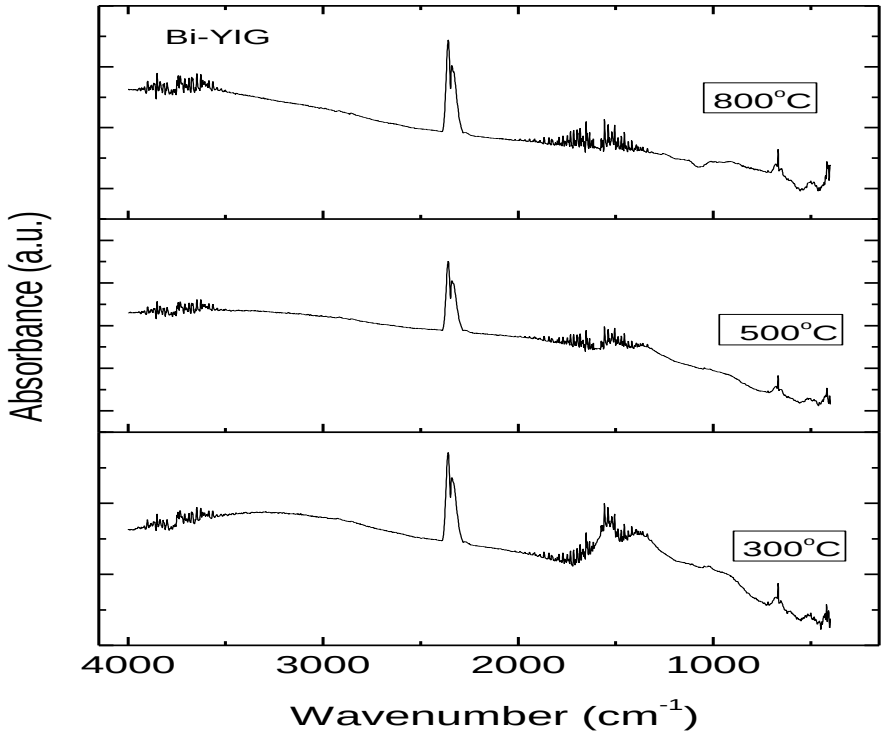

Figure 5.6 FTIR spectra of Bi-YIG based films at different temperatures

particular groups of atoms. The FTIR spectra may also be employed to analyse the decomposition process of the organic gels if we collect the spectra at different stages of the process (Zhao, Cai, Luo & He, 2004). The resulting spectra produce a profile of the sample, a distinctive molecular fingerprint that can be used to easily screen and scan samples from many different components. It is an effective analytical instrument for detecting functional groups and characterizing covalent bonding information (Kayatekin, 2006).

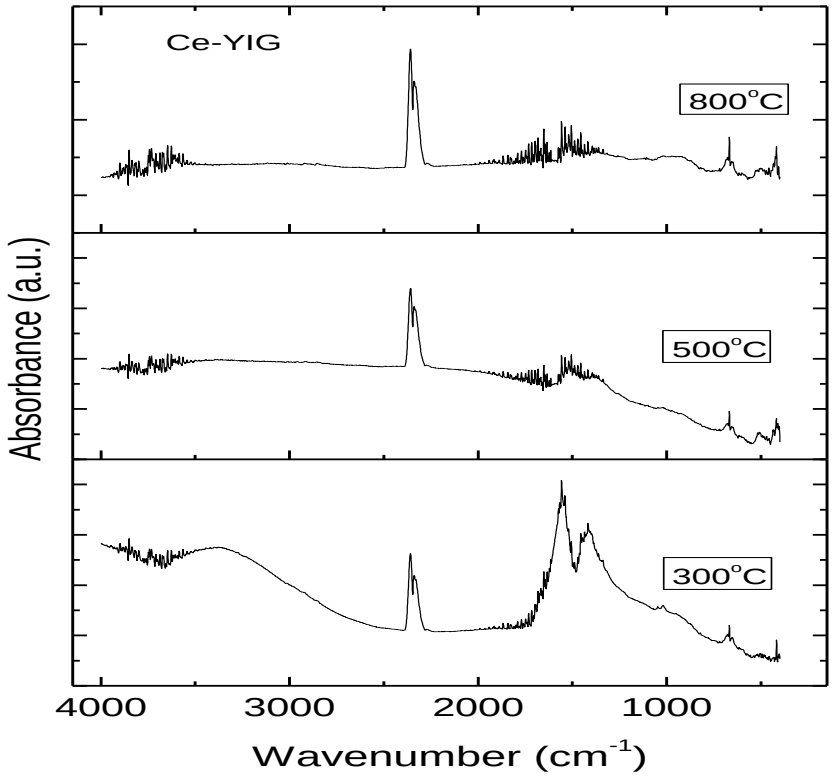

Figure 5.7 FTIR Spectra of Ce - YIG based films at different temperatures

In order to obtain FTIR spectra of YIG, Bi-YIG and Ce-YIG based thin films, solutions were coated on substrates with spin coater and heat treated at specific temperatures determined via DTA/TG. The determined specific temperatures are 300°C, 500°C and 800°C. These temperatures are the peaks in the DTA results, where reactions occur. Thus FTIR is employed to determine the nature of these reactions. Several FTIR spectra of the sol-gel thin films were carried out in the range

of 4000-400 cm^{-1} and were represented for YIG, Bi-YIG and Ce-YIG based films in Figures 5.5, 5.6 and 5.7 respectively. As can be seen on the frequency O-H, C=O and M-OCOO-M bond decreased at 300˚C and finished 500˚C. This means that the organic content and hydroxyl were removed. The relative result of the spectra are Y=O and Fe=O bonds under 600 cm^{-1}. The density of the bands increased with increasing temperature. Thus it can be expressed that different oxide formations were occured. Figures 5.6 and 5.7 are different from Figure 5.5 because there are minor amounts of Bi and Ce in the structure. By this way Bi-O and Ce-O bands can be seen in the spectra as a result of this addition.

5.2.3 Phase Analyses

XRD patterns of YIG, Bi-YIG and Ce-YIG based thin films were represented in Figures 5.8, 5.9 and 5.10 respectively. The obtained patterns were compared device library with search match operation. After deposition of the YIG based solution to the Si(100) substrate and several heat treatments, the pattern illustrated in Figure 5.8 was obtained. As shown in that pattern pure YIG phase was obtained in this films with low intensities because of very thin film thickness. Small amount of Fe_2O_3 was observed in the pattern. This must be resulted from heat treatment time or temperature. Since there is not enough time for diffusion ions could not take their place in the structure. Another alternative reason might be that; while weighting precursors some mistakes may be done and these make stoichimetry to be broken.

XRD pattern of Bi-YIG was represented in Figure 5.9. As seen in pattern YIG phase with low amounts of Fe_2O_3. Here Y^{3+} ions fully diffused in to the strucutre but Fe^{3+} could not be diffused. Time or temperature for heat treatment must be increased to obtain full diffusion of all ions. Since Bi^{3+} ions sublimates at low temperature with a fast sublimation rate. In order to keep this ions in the structure $M^{(IV)}$ contented precursor were added to solutions as reported in literature. Researchers added specific amounts Ge as a $M^{(IV)}$ element. By this way two magneto-optic phases occur in the structure one of them Bi-YIG and $Bi[M^{(IV)}]_{12}O_{20}$ (Bismuth Silicate) as mentioned elsewhere (Rehspringer et al., 2000).

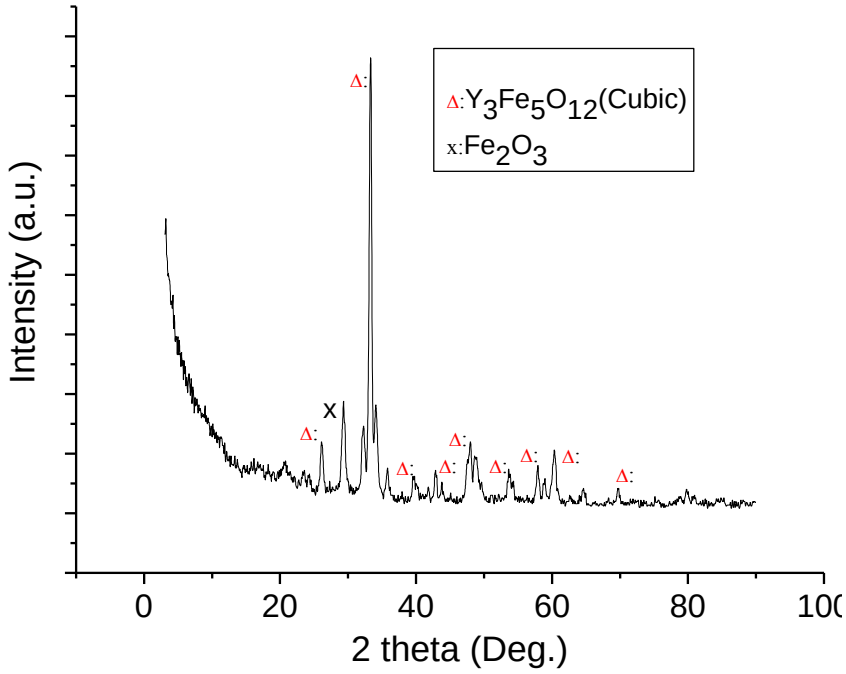

Figure 5.8 XRD pattern of YIG thin film on Si substrate

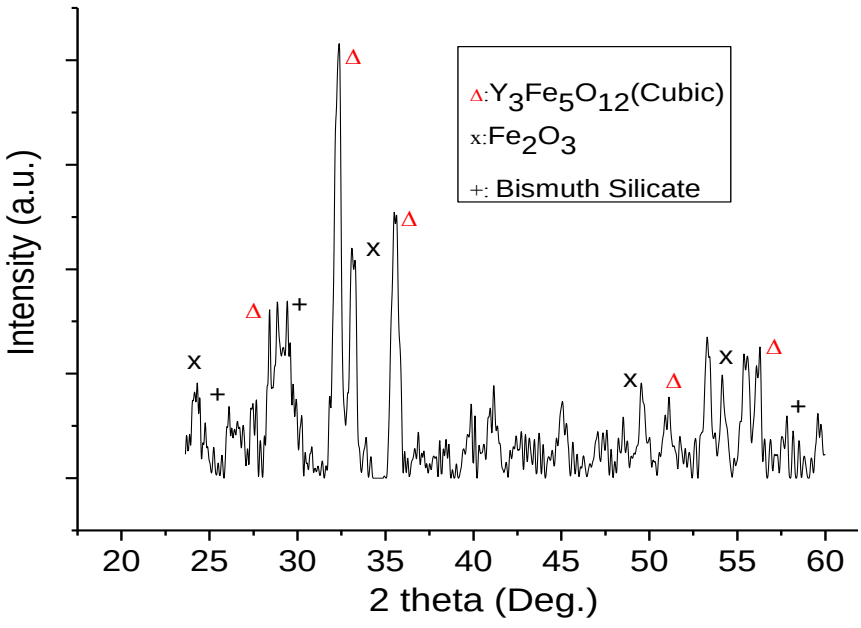

Figure 5.9 XRD pattern of Bi-YIG thin film on Si substrate

In this thesis study Si based precursor (Si (IV) acetate) was added in to the solution with a rate $Bi/M^{(IV)}=12$. If the pattern in Figure 5.9 was considered it can be

seen that Bismuth silicate and YIG phases were obtained together succesfully. Since the product and byproduct of this reaction are magneto-optical materials there is no negative effects Bismuth silicate to be in the structure. Also there are small amounts of undefined peaks in the pattern which were not recognized by XRD device guide. These peaks may be resulted of some impurities of noises of the device.

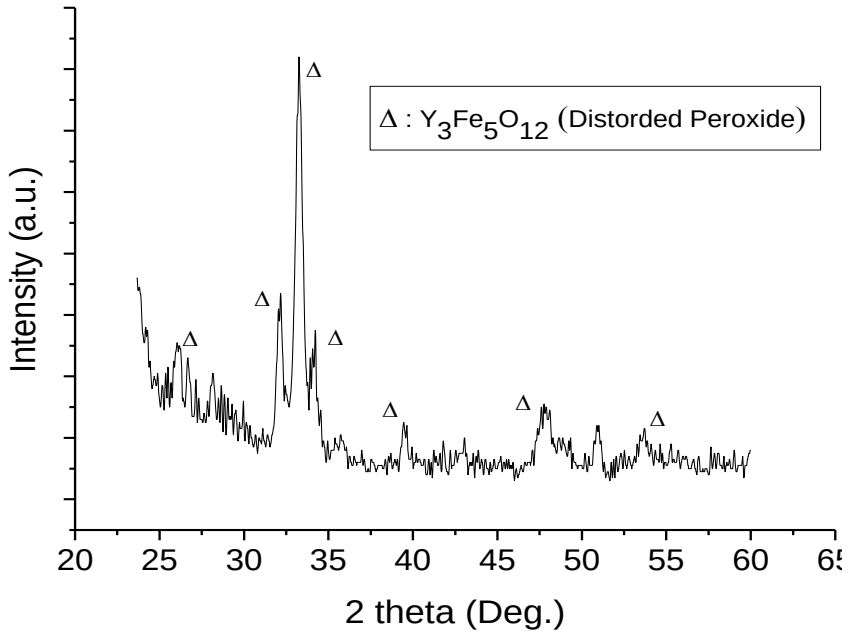

Figure 5.10 XRD pattern of Ce-YIG thin film on Si substrate

5.2.4 Microstructure

SEM images of YIG, Bi-YIG and Ce-YIG films on Si substrates were represented in Figure 5.11. The morphology of the films is an important parameter that affects electronic, magnetic and magneto-optical properties as mentioned before. The more smooth film surface the better properties obtained. Morphology of the films are directly affected from the processing parameters such as; solution concentration, pH, viscosity, film thickness, coating technique, and heat treatment regime.

The SEM micrographs of YIG thin film includes cracks, pinholes, channels and coating islands as seen in Figure 5.11.a. The coating technique which was employed

for this specimen is spin coating. Although spin coating is a technique which provides smooth surfaces heat treatment regime resulted this structure. While this film was prepared to have three layered coating heat treatment regime was including thermal shocks. These thermal shocks caused micro structure to have cracks and pinholes etc.

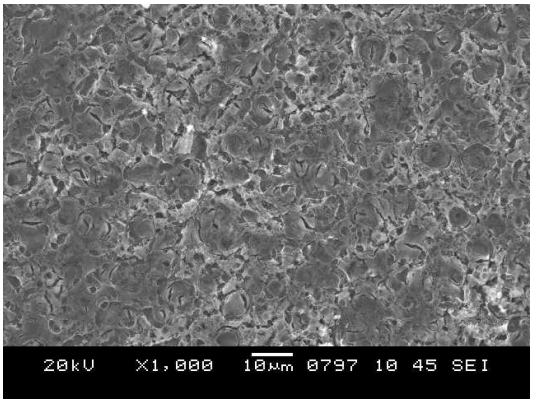

(a)

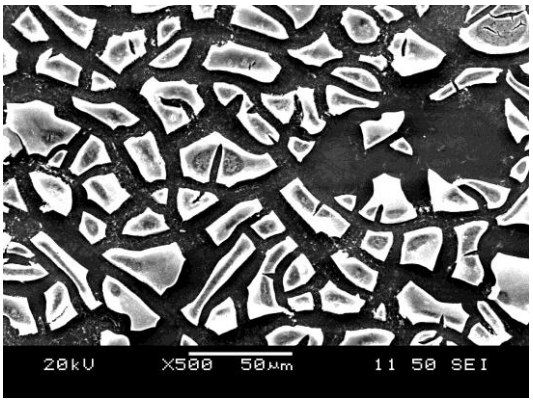

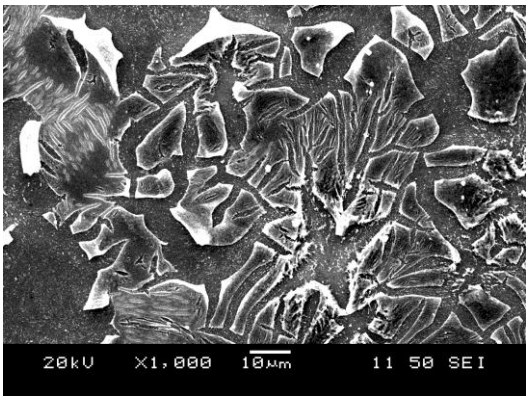

(b) **(c)**

Figure 5.11 SEM images of (a) YIG, (b) Bi-YIG, (c) Ce-YIG films on Si substrates

SEM image of Bi-YIG sample was illustrated in Figure 5.10.b. Since this sample was produced via solution dropping technique the structure have many coating islands. Also the channels in this structure are wider and morphology is worse than YIG structure. Different from YIG sample the structure obtained in this sample is directly related to coating technique.

The SEM micrograph Ce-YIG films in Figure 5.10.c shows that there are cracks on the surface. This surface morphology occurred because of thermal treatment effects of our production steps. The surface of this specimen has Ce domains (small

white points). Sizes of regions containing CeO_2 vary from 100 nm (or less) to 1000 nm. EDS counts of white areas shows that these regions contain mainly Ce and O and some faction of Y and Fe. Gray areas have very small fraction of Ce. In addition, some Ce ions tend to exist in a diamagnetic tetravalent state Ce^{4+} without free electrons while some precipitates as a CeO_2. The non-magnetic CeO_2 particles in the Ce-YIG or YIG will affect the intended magnetic characteristics [Öztürk et al. 2008]. As a result, there were nano and micro size CeO_2 weighted regions on the Ce-YIG surface.

In addition in order to present spin coated samples, partially YIG phase including Ce-YIG and Bi-YIG microstructures are depicted in Figure 5.12. The morphology of these films found to be better than the solution dropped ones but % 100 YIG could not be observed.

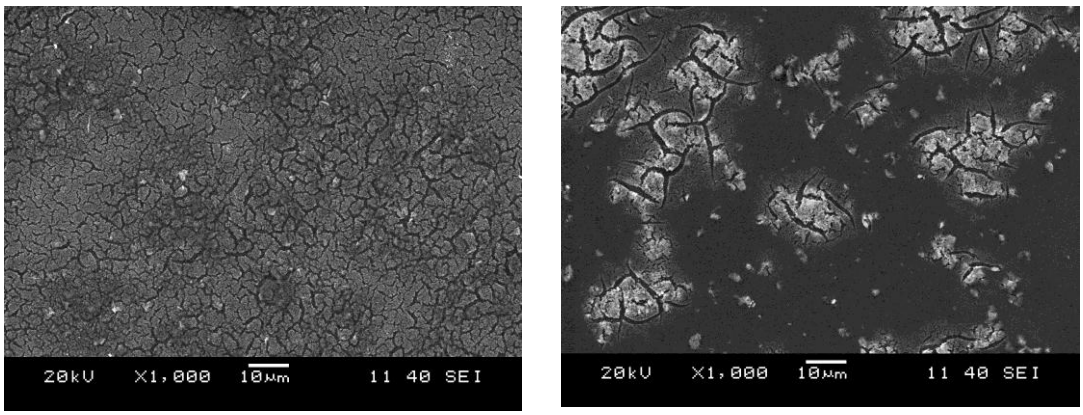

(a) (b)

Figure 5.12 SEM images of partially YIG phase containing (a) Ce-YIG and (b) Bi-YIG films on Si(100) substrates.

5.2.5 Refractive index, Film Thickness and Band Gap

The determination of film thickness using white light interference is a well known and established principle. Such optical techniques for the determination of thin film characteristics rely upon the interaction of the film with light, and can be used to determine not only thickness but also optical constants. They are dependent upon the interference pattern resulting from partial reflection/transmission through two

partially reflecting surfaces. This method of thickness measurement provides an investigative tool that is accurate, nondestructive and requires no sample preparation (Hind & Chomette, n.d.).

In the case of a thin film on the surface of a glass, both the top and bottom surfaces of the film reflect light, with the total amount reflected being dependent upon the sum of these two reflections. Furthermore, these two reflections may add together constructively or destructively depending upon their phase relationship. This phenomenon is due to the wavelike nature of light, with the phase relationship determined by the difference in optical path lengths of the two reflections. The resulting interference pattern can be used to determine the thickness of the film according to the formula

$$d = \frac{m}{2D\sqrt{(n^2 - \sin^2\theta)}} \qquad (5.2)$$

where; d=film thickness, m=number of patterns in wavenumber region used, n=refractive index, θ=angle of incident (measured by spectrophotometer during measurement), D_n= wave number region used (Hind & Chomette, n.d.,).

Table 5.6 Refractive index, film thickness and band gap of the films

Sample	**Refractive Index (nD)**	**Thickness (µm)**	**Band Gap (eV)**
YIG	1,57	0,914	4,74
Ce-YIG	1,47	0,206	3,6
Bi-YIG	1,48	0,194	3,72

Refractive index, film thickness and band gap values of YIG, Bi-YIG and Ce-YIG films which were deposited on glass substrates were listed in Table 5.6. In a logical view the refractive indexes and band gap of the YIG film is higher than the substituted films. Substitution of metallic conductive ions in to the structure decreased band gap. Due to the fact that YIG sample is deposited with a different technique, the thickness value of this film is higher than the others as mentioned before.

5.2.6 Magnetic Properties

Magnetization (M) versus magnetic field curves were obtained using VSM device with the effect of diamagnetic substrate. The measurements were applied to the thin film surfaces both paralel and perpendicularly. The data obtained from these measurements were illustrated in Figures 5.13, 5.14 and 5.15 for YIG, Bi-YIG and Ce-YIG respectively.

As seen from Figure 5.13, YIG based specimen was found to be both parallel and perpendicularly magnetized. Saturation magnetization (M_s) and remanent magnetization were measured for parallel magnetization 7,4 emu/cc and 1,8 emu/cc, for perpendicular magnetization 11,4 emu/cc and 5,4 emu/cc respectively. The coercivity (H_c) value of YIG based specimen was found to be as 60 Oe. If this value compared to literature, it is lower than Bulk YIG (Öztürk et al., 2008).

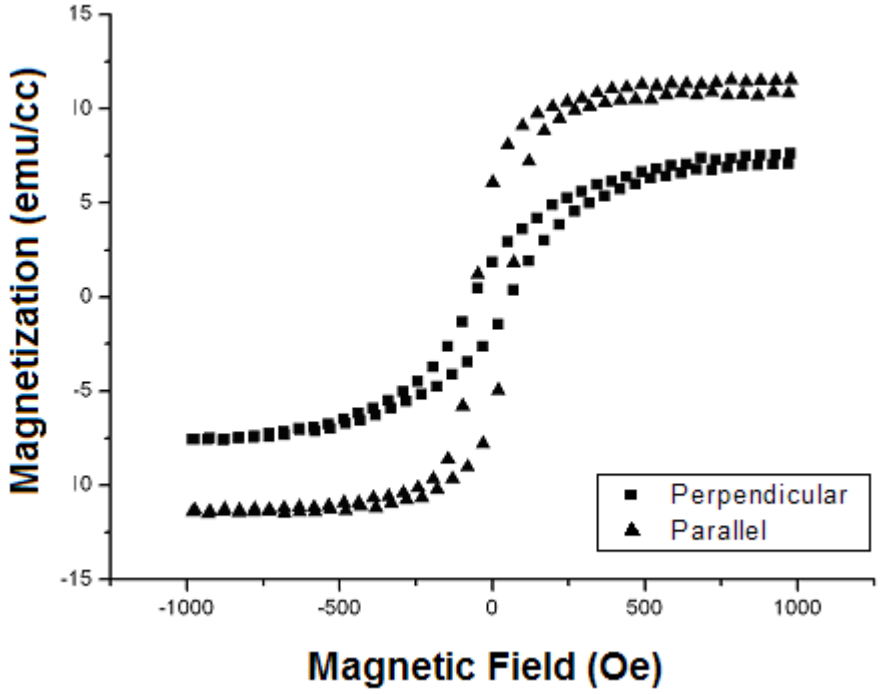

Figure 5.13 Magnetization versus magnetic field curve of YIG sample.

Prepared Bi-YIG specimens show magnetic properties in-plane and perpendicular configurations as seen in Figure 5.14. Along with VSM results we should also regard XRD results: the XRD results indicate Bi-YIG is in comparison to other phases

present (Figure 5.9). According to XRD result the existing phases are Fe_2O_3, $Y_3Fe_5O_{12}$ and $Bi(Si)_{12}O_{20}$. Fe_2O_3 has paramagnetic behavior and also $Y_3Fe_5O_{12}$ is ferrimagnetic material but there is evidently a diamagnetic effect in our measurements dominating other phases. Si (100) was used as a substrate. Due to the fact that bulk Si is a diamagnetic material, the curve probably is affected from this condition as explained in literature (Erol et al., 2009). However for perpendicular configurations diamagnetic effect is suppressed. This can be attributed to film perpendicular case has nonzero de-magnetization coefficient whereas for in plane case demagnetization coefficient is almost zero. As a result of mentioned reasons above no saturation was obtained.

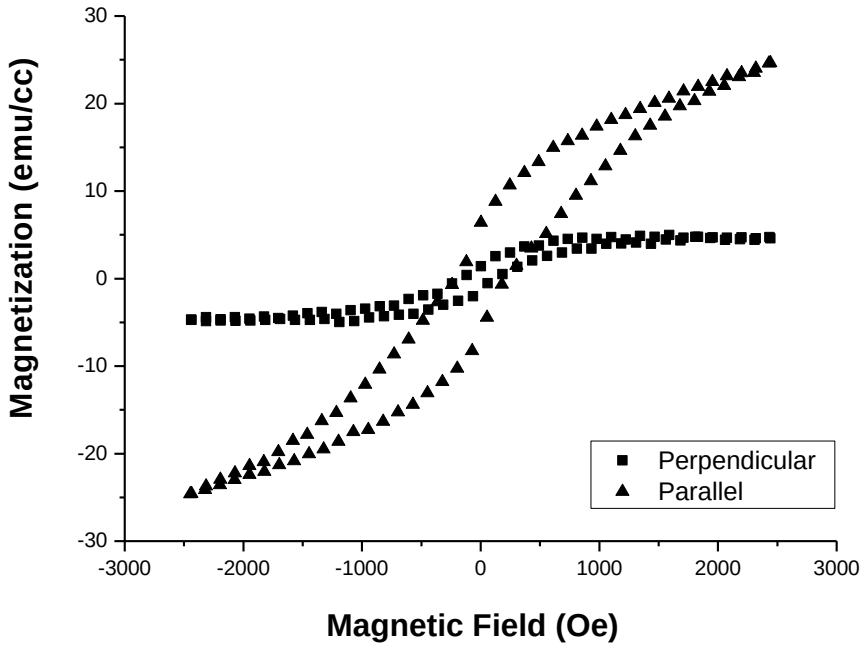

Figure 5.14 Magnetization versus magnetic field curve of Bi- YIG sample.

Similar curves were obtained for Ce-YIG specimen with Bi-YIG specimen represented in Figure 5.15. Although these thin films have YIG phase with high concentrations, the thicknesses of the films were around 200 nm. Since the thicknesses are low the affect of the substrates found to be very affective in VSM results.

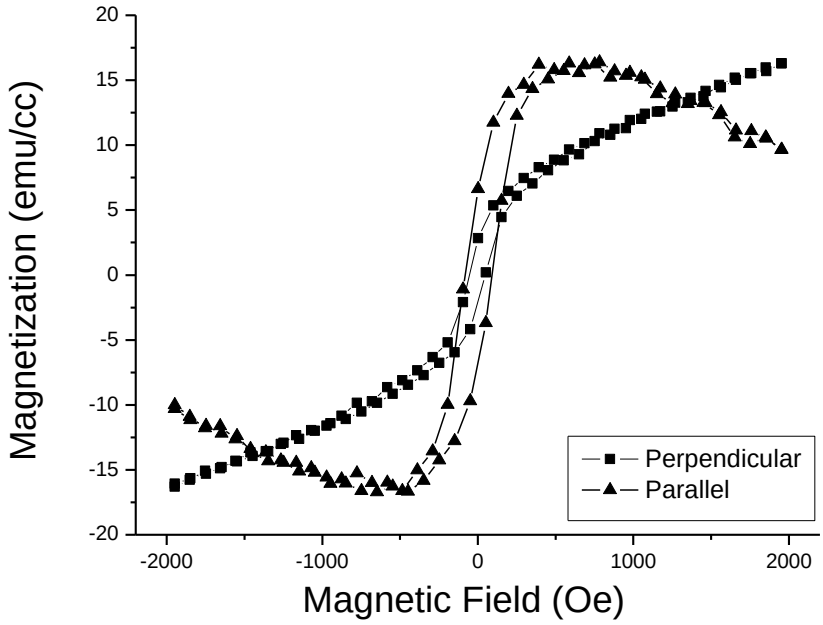

Figure 5.15 Magnetization versus magnetic field curve of Ce- YIG sample.

As a summary of magnetic properties of YIG based thin films condensed on this thesis, since the used technique is sol-gel there are too many factor affecting the obtaining the exact phases as mentioned elsewhere. At the same time magnetic properties of the films were found to be affected from these parameters.

5.2.7 Magneto-optical properties

An important point of this thesis is the design and optimization of magneto-optical measurement system setup. System equipments and their functions were summarized in previous chapter (Chapter 4).

In order to apply magneto-optical measurements with the designed system, firstly reference specimens were employed. Production history, magnetic and magneto-optical properties of these specimens were known and summarized below. After the optimization was performed, magnetooptic measurements for YIG based specimens were employed in this setup.

As a further information; reference specimen used was Co thin film which have thickness of 84 nm, magnetization 2,3 emu/cc, surface roughness in nanometer scale and produced with magnetron sputtering (a homogenous, pure and low roughness thin film production technique). In order to represent that the designed setup, works at different wavelengths and frequencies, studies at different conditions were applied to the Co specimens. These detailed experimental results were represented in Figure 5.16.

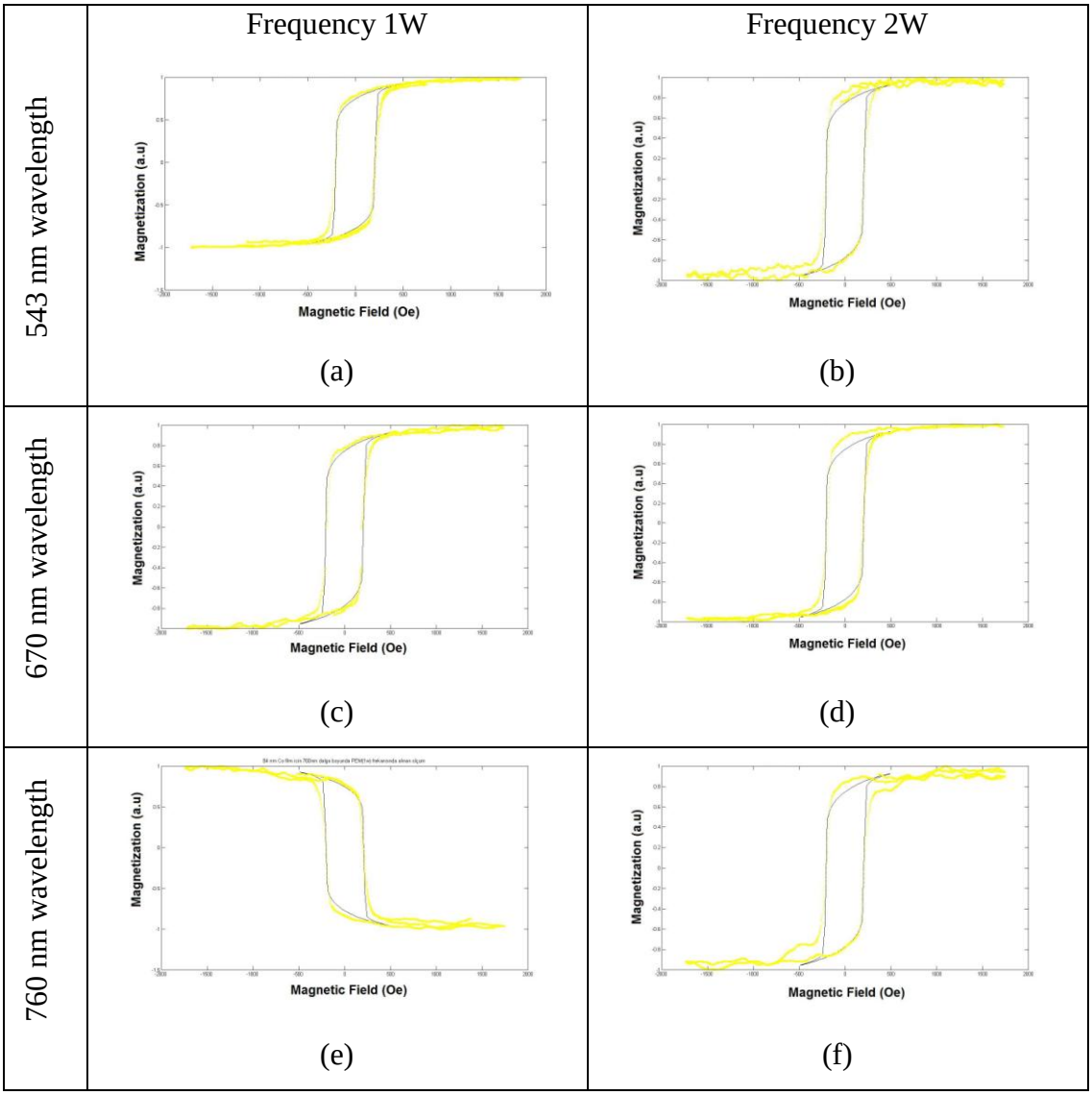

Figure 5.16 Magneto-optical properties of Co films at different wavelength and frequency conditions.

As seen in Figure 5.16 different wavelengths and frequencies were employed to optimize the system. All hysteresis loops obtained via experiments and reference hystresis loop represented at figure keep coherency to each other. By this way one can say that the system is optimized and can do measurements of magneto-optical materials.

In order to obtain Kerr rotation of the films, theoretical measurement must be employed. As seen experimental setup (Figure 4.4) by using the polarizer one directional polarized light was obtained. Then to obtain square wave laser is passed throught the chopper (optic-cut). Next the light reaches to the specimen which is in the magnetic field. The polarization of the laser is changed by the specimen. This polarization change is modulated by PEM and reached to the photo-diot. By using LIA the voltage (V_{DC}) obtained on the photo-diot is measured. As mentioned above by using sequences 5.3 and 5.4 first harmonic (V_{1f}) and second harmonic (V_{2f}) were measured in order to determine polarization rotation and elipticity of the signal respectively.,

$$\theta_K = \frac{\sqrt{2}V_{2f}}{4J_2V_{DC}} \tag{5.3}$$

$$\psi_K = \frac{\sqrt{2}V_{1f}}{4J_1V_{DC}} \tag{5.4}$$

The Kerr elipticity and the Kerr Rotation were calculated by the sequences above and depicted in Figure 5.17. Similar studies were performed by several researchers. The results we ontained for Co thin films were supported by literature (Rellinghaus et al., 1997).

After optimization of the system, in order to apply magneto-optical measurements of YIG based samples, the same procedure was employed. The YIG specimen was firstly fixed between electromagnets and then the experiment started as mentioned elsewhere.

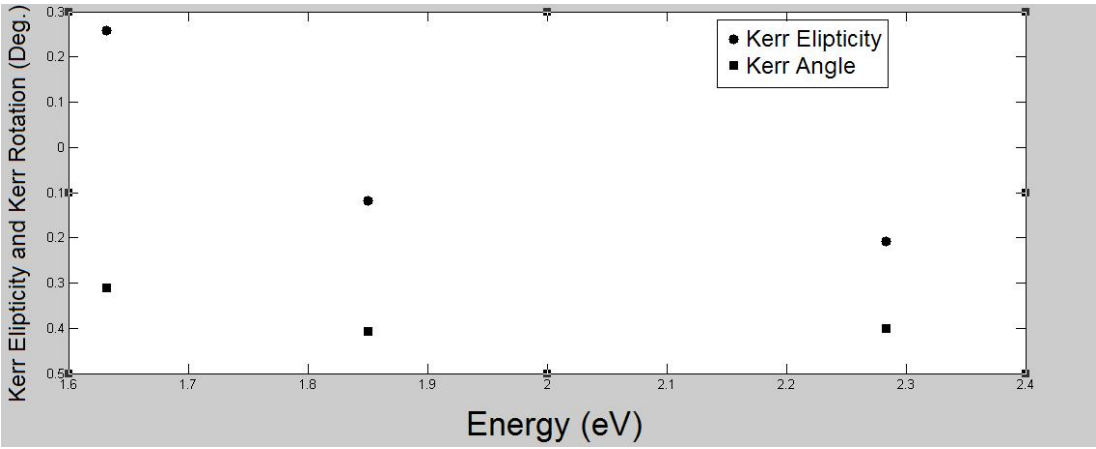

Figure 5.17. Calculated kerr elipticity and kerr rotation of Co thin films at different wavelengths.

Many experiments were repeated to obtain similar results with Co samples. Only one significant hysteresis loop was obtained for Ce-YIG specimen which was depicted in Figure 5.18. Any expressive results were obtained for YIG and Bi-YIG specimens.

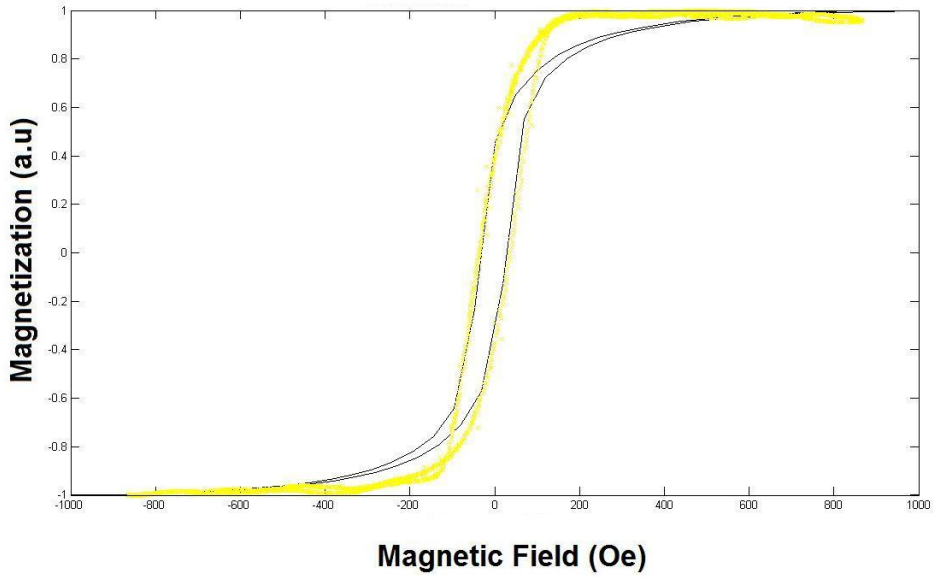

Figure 5.18 Magneto-optical properties of CeYIG samples at 543 nm wavelength

In order to compare the results of Co specimen and our samples, these can be considered such as; there are many parameters affecting the measurements on system (fixage of the system components and specimens, applied field and system efficiency etc…), film surface must be homogenous and have low roughness, the reflection of

the thin films must be good at in many wave lengths. And also the production technique of the YIG samples (sol-gel) and Co specimen (magnetron sputtering) are different.

As a result since the surface roughness and homogeneity of both YIG and Bi-YIG samples are not appropriate for measurement; any significant results were obtained to be reported in this thesis.

CHAPTER SIX
CONCLUSIONS

6.1 General Results

In this study, synthesis of garnet based films by sol-gel technique and their magneto-optical properties were investigated for coated specimens. The following conclusions are obtained from the experimental works:

1- Turbidity values of the YIG, Ce-YIG and Bi-YIG based solutions were measured as 329, 686 and 380 respectively. These values pointed that powder based precursors are not almost completely dissolved in all solutions and the red color of the iron based precursor increased the turbidity.

2- The pH values of the solutions were found to be for YIG, Ce-YIG and Bi-YIG based solutions 3,7, 3,24 and 3,31 respectively. This pH measurement results pointed that all solutions are acidic. Also, addition of Ce and Bi based precursors increase the acidic characteristic since they include H^+ ions at significant amounts.

3- The average viscosity values of YIG, Ce-YIG and Bi-YIG solutions were found to be 1,93 mPa.s, 1,32 mPa.s., and 1,99 mPa.s respectively. Since the stoichiometric rate of the Bi precursor is more than that of the Ce precursor, the viscosity value is determined to be higher.

4- Generally, three thermal phenomena in the xerogel were determined for the all YIG based xerogels. The first endothermic peaks represent this solvent removal. The combustion process of organic groups occurred at ~350^{o}C as a second thermal phenomenon. The last phenomenon was the formation of ceramic oxides at temperatures between 450 and 500 ^{o}C. The significant amount of these weight losses was observed during the combustion and oxidation reactions. Weigh losses of the xerogels were found to be for YIG, Ce-YIG and Bi-YIG as 64%, 32% and 73%

respectively. Thus by using these results heat treatment regimes were determined for sol-gel coated thin films.

5- FTIR analyses were performed to determine the removal of organic components in the structure. The intensities and noise of the vibrations decreased with increasing temperature and the spectrum becomes smoother for all spectrums while the oxide content increasing.

6- Almost pure YIG and substituted YIG thin films were produced according to XRD results. YIG has several crystal structures that have different magnetic and magnetooptical properties. Some of these crystal structures were obtained in this study.

7- The SEM micrographs of the films were represented in previous chapter (Chapter 5). Depending on obtained results one can express coating process and heat treatment regime are directly in a relation with microstructure. Spin coated samples have more smooth surfaces than the samples which were coated by solution dropping technique.

8- The refractive index, band gap and thickness measurements are important electronic characterization steps. The obtained results were employed in magnetic and magneto-optical characterization. The obtained results for YIG, Ce-YIG and Bi-YIG thin films are given in previous chapter. The band gap value was found to be decreasing by addition of metallic Ce and Bi. According to these results one can say that results changing logically since the conductivity increasing.

9- The hysteresis loops of the films were determined via VSM. Except YIG based solution no saturation was obtained. There are many factors affecting the properties of the thin films such as morphology, phase structure and, homogeneity. Although there are almost pure XRD patterns obtained expected hysteresis loops cannot be observed.

10- Magneto-optical measurement system setup and magneto-optical measurements are the significant issues of this thesis. The system setup was installed successfully. By using Co samples, calibration of the system was carried and Kerr elipticity and Kerr rotation of the samples were determined by using system and theoretical calculations. Similar studies were repeated for YIG based samples and any significant results were obtained according to the reasons mentioned on VSM results.

6.2 Future Plans

It is recommended that a further study should be carried out to obtain more homogeneous, crack-free, pinhole-free, and textured YIG films. With this aim, new coating solutions can be prepared with different pH, viscosity and contact angle values. Except solutions, coating procedure parameters should be changed. Also, heat treatment regime should be optimized to decrease thermal shock risks. If the mentioned problems were handled, magnetic and magnetooptical measurements could be performed successfully.

REFERENCES

Akdoğan N., (2004), *Magnetooptical measurements on thin films*., Technical University of Yıldız, Master of Sciences Thesis, İstanbul.

Argonne National Laboratory, (2002), *Magneto-optical imaging*, 17 March 2009 from; http://superconductivity.et.anl.gov/Facilities/MOI.html.

Buschow K.H.J., (1995). *Handbook of Magnetic Materials*- North-holland Press.

Callister W.D. Jr, (2008) *Materials Science and Engineering An Introduction (7th ed.)*, New York: John Wiley & Sons, Inc.

Cardarelli F. (2000) *Materials Handbook: A Concise Desktop Reference* (2th ed.), Tuscon, Arizona: Springer.

Case Western University, (2009), *Light and Polarization*, 23 April 2009 from; http://plc.cwru.edu/tutorial/enhanced/files/lc/light/light.htm.

Choi J. D., Choi G. M., (2000), "Electrical and CO gas sensing of layered ZnO-CuO sensor", *Sensor and Actuators B69* 120-126.

Das B.K., Rastogi A.C. and Kotnala R.K., (1994), *DESlDOC Bulletin of Inf Technol, 14(1)*

DiBiccari A., (2002), *Sol-gel processing of $R_xY_{3-x}Al_yFe_{5-y}O_{12}$ magneto-optical films*, Virginia Polytechnic Institute and State University Material Science and En gineering Departmant, Master of Science Thesis, Blacksburg, Virginia

Erol M., Öztürk Y., Avgın I. and Çelik E., (2009), Production, characterization and magnetic properties of Bismuth-substituted Yttrium Iron Garnet layers prepared by sol-gel process, *Journal Of Physics, Conference Series 153*

Fujihara S., Sasaki C. and Kimura T., (2001), "Crystallization behavior and origine of c-axis orientation in sol-gel derived ZnO:Li thin films on glass substrates", *Applied Surface Science* 180 341-350.

Gomi, M., Satoh, K., Abe, M. (1988), Giant Faraday rotation of Ce-substituted YIG films epitaxially grown by RF sputtering. *Jpn. J. Appl. Phys.* **27**, 1536.

Haitao Xu, Hua Yang, Wei Xu, Feng S, (2008), Magnetic Properties of Ce,Gd-Substituted Yttrium Iron Garnet Ferrite Powders Fabricated Using a Sol–Gel Method, *Journal of Materials Processing Technology* 197 296–300

Henderson, T. (1997), Tom Henderson, Tom Henderson's Web Site, http://www.glenbrook.k12.il.us/GBSSCI/PHYS/CLASS/light/u12l1e.html

Higuchi, S., Ueda, K., Yahiro, F., Nakata, Y., Uetsuhara, H., Okada, T., Maeda, M.: (2001), Fabrications of Cerium-Substituted YIG Thin Films for Magnetic Field Sensor by Pulsed-Laser Deposition. *IEEE Trans. On Magn*. **37**, 2451-2453

Kayatekin I. 2006, *Synthesis and Characterization of buffer layers and* $YBA_2CU_3O_x$ *Superconducting coatings by chemical solution deposition*, University of Dokuz Eylül, Master of Science Thesis, İzmir, Tukiye.

Kurkjian, Charles R. and Prindle, William R. (1998). Perspectives on the History of Glass Composition, *Journal of the American Ceramic Society*, 81 (4), 795-813.

Moulson, A. J., Herbert, J. M.: (2003) *Electroceramics*- John Wiley & Sons Ltd., West Sussex.

Obradors, X., Puig, T., Pomar, A., Sandiumenge, F., Pinol, S., Mestres, N., et al. (2004). Chemical solution deposition: a path towards low cost coated conductors. *Superconducting Science Technology*, 17, 1055-1064.

Öztürk, Y., Avgın, I., Erol, M., Çelik, E., (2007), Cerium—doped Yttrium Iron Garnet Thin Films Prepared by Sol-Gel Process: Synthesis, Characterization and Magneto-optic Properties, *Advances in Nanoscale Magnetism Proceedings of the International Conference on Nanoscale Magnetism ICNM-2007 June 25–29, Istanbul, Turkey.*

Phonthammachai, N., Rumruangwong, M., Gulari, E., Jamieson, A.M., Jitkarnka, S., Wongkasemjit, S. (2004). Synthesis and rheological properties of mesoporous nanocrystalline CeO2 via sol–gel process. *Colloids and Surfaces A: Physicochem. Eng. Aspects*, 247, 61-68.

Pierre, A. C. (1998). *Introduction to sol-gel processing*. USA: Kluwer Academic Publishers.

Popescu, A.; W., Thomas (2005). On the potential of Faraday anomalous dispersion optical filter as high-resolution edge filters". *Laser physics* 15 (1): 55–60.

Rastogi, A.C., Moothy, V.N. (2002). Magnetic properties of multilayers of nano thin Co,Ce-doped and undoped yttrium iron garnet films for magneto-optic applications. *Materials Science and Engineering* **B95**, 131-136.

Rehspringer J.L., Bursik J., Niznansky D., Klarikova A., (2000) Characterisation of bismuth-doped yttrium iron garnet layers prepared by sol}gel process, *Journal of Magnetism and Magnetic Materials,* pp. 291-295.

Sekijima, T., Kishimoto, H., Fujii, T., Wakino, K., Okada, M.: (1999). Growth of terbium aluminum garnet ($Tb_3Al_5O_{12}$; TAG) single crystals by the hybrid laser floating zone machine, *Jpn. J. Appl. Phys*. **38**, 5874.

Shinagawa, K., (1999): *Magneto-optics*- Springer, Berlin.

Tas A.C., E. Akin, and, Der H. (1996), "Chemical Preparation of YIG and YAG Powders by Self-Propagating Combustion Synthesis," *III. Ceramics Congress, October 22-25, , Istanbul, Turkey, Proceedings Book*, Vol. 2, pp. 440-450.

Uno T., Noge, S. (2001), Growth of magneto-optic Ce:YIG thin films on amorphous silica substrates. *Journal of the European Ceramic Society* **21**, 1957–1960 .

Wickersheim, K.A., Buchanan, R.A.: (1967). Optical Studies of Exchange in Substituted Garnets. *J. Appl. Phys*. **38** 1048 .

Wikipedia Foundation (2008), *Electromagnetic radiation*, 25 April 2009 from; http://en.wikipedia.org/wiki/Electromagnetic_wave_theory.

Wikipedia Foundation (2008), *Polarization,* 23 April 2009 from; http://en.wikipedia.org/wiki/Polarization.

Wikipedia Foundation, (2009), *Faraday effect*, 7 January 2009 from; http://en.wikipedia.org/wiki/Faraday_effect.

Wikipedia Foundation, (2009), *Magneto-optic Kerr effect*, 7 January 2009 from; http://en.wikipedia.org/wiki/Magneto-optic_Kerr_effect.

Wilde, F. D. & Gibs, J. (n.d.). Turbidity. *Geological Survey TWRI* Book 9, 1-30.

Xu H., Yang H., Xu W., Feng S. (2008). Magnetic properties of Ce, Gd-substituted yttrium iron garnet ferrite powders fabricated using a sol–gel method, *Journal of Materials Processing Technology* 197; 296.

Y. L. Liu, Y. C. Liu, Y. X. Liu, D. Z. Shen, Y. M. Lu, J. Y. Zhang and X. W. Fan, (2002), “Structural and optical properties of nanocrystalline ZnO films grown by cathodic electrodeposition on Si substrates”, *Physica B: Condensed Matter* 322 31-36.

Zhang X.-W., (2008), Faraday rotation spectra of bismuth-substituted rare-earth iron garnet crystals in optical communication band *Journal of Crystal Growth* 310; 3235.

Zhao, Y. E., Cai, C. Y., Luo, Y. Y., & He, Z. H. (2004). FTIR spectra of the M(EDTA)n- complexes in the process of sol-gel technique. *Journal of Superconductivity: Incorporating Novel Magnetism*, 17 (3), 383-387.